DISSERTATION

Three-Dimensional Simulations of Split-Drain MAGFETs

ausgeführt zum Zwecke der Erlangung des akademischen Grades
eines Doktors der technischen Wissenschaften

eingereicht an der Technischen Universität Wien
Fakultät für Elektrotechnik und Informationstechnik

von

Rodrigo RODRÍGUEZ TORRES

[redacted]

[redacted]

Wien, im März 2003

Kurzfassung

Mit Halbleitertechnologie gefertigte magnetische Sensoren zeigen eine elektrische Antwort, wenn sie einem magnetischen Feld ausgesetzt werden. Dieses elektrische Signal resultiert aus einer Reihe von physikalischen, als galvanomagnetisch bekannten, Effekten, nämlich die Auswirkung der Lorentz-Kraft auf in Bewegung befindenden Ladungen im Inneren des Sensors. Magnetische Sensoren werden dahingehend optimiert, dass, falls ein magnetisches Feld eingeprägt wird, die beweglichen Ladungen im Inneren des Sensors die größtmögliche Ablenkung erfahren. Die physikalischen Eigenschaften des Halbleiters spielen bei der Herstellung magnetischer Sensoren eine überaus wichtige Rolle.

Die Beweglichkeit der Ladungen ist einer der wichtigsten Parameter in magnetischen Halbleitersensoren. Da die Ablenkung der Ladungen ein direkt proportionales Verhältnis mit der Beweglichkeit aufweist, können auch schwächere magnetische Felder erkannt werden. Nichtsdestoweniger ist die Herstellung magnetischer Halbleitersensoren, deren Ladungen hohe Beweglichkeit aufweisen, sehr teuer und ist nur bei Fehlen anderer Alternativen sinnvoll. Darüberhinaus scheint eine Integration der Verarbeitungselektronik des Sensors auf demselben Chip empfehlenswert.

Die CMOS-Technologie ist die verbreiteteste und billigste Halbleitertechnologie. Die Verwendung von Silizium als Halbleiter ermöglicht die Produktion von Millionen identischer elektronischer Bausteine zu relativ niedrigen Preisen. Die Herstellung eines magnetischen Siliziumsensors mit CMOS-Technologie ist billig, da die Elektronik des Sensors einfach in einer integrierten Schaltung hergestellt werden kann. Dies ist jedoch nur möglich, wenn die Herstellung der Struktur des magnetischen Sensors ohne jegliche Änderung der Herstellungsschritte der CMOS-Technologie durchgeführt wird. Das Hinzufügen von Prozessschritten ohne eine Erhöhung des Endpreises des integrierten Sensors ist nicht möglich.

Der Split-Drain Magnetic Metal-Oxide-Semiconductor Field Effect Transistor, MAGFET, ist die beste Alternative zur Herstellung von magnetischen integrierten Sensoren mit CMOS-Technologie. Ihre Herstellung bedarf keines zusätzlichen Prozessschrittes, sie ist zu 100% mit dem CMOS-Prozesses kompatibel. Die Verarbeitungselektronik des elektrischen Signals kann auf demselben Substrat wie der Sensors integriert werden. Die CMOS-Technologie wurde für die Herstellung von Hochleistungs-MOSFETs entwickelt, der MAGFETs nutzt den Inversionskanal eines typischen MOSFETs. Nichtsdestoweniger ist die Beweglichkeit der Ladungen im Inversionskanal nicht so hoch wie in reinem Siliziumsubstrat oder in einigen anderen Halbleitern.

Beim Split-Drain MAGFET ist der Drainkontakt in mehrere Teile geteilt. In Abwesenheit eines magnetischen Feldes verteilt sich der gesamte Strom gleichmäßig auf die Drains. Wenn ein magnetisches Feld senkrecht auf den Inversionskanal eingeprägt wird, sind die Drainströme nicht mehr gleich. Eine Stromdifferenz kann gemessen werden, die proportional zur Beweglichkeit der Ladungträger ist. Bei Raumtemperatur können nur große magnetische Felder gemessen werden, bei Kühlung mit flüssigem Stickstoff funktioniert dies auch für schwache magnetische Felder. Darüberhinaus bietet die Tieftemperaturoperation weitere Vorteile, wie zum Beispiel ein besseres Signal-Rausch-Verhältnis.

Um die Beziehungen zwischen den elektrischen und den magnetischen Kräften innerhalb des Halbleiters besser verstehen zu können, sind dreidimensionale Simulationen notwendig, die Vektornatur der Lorentz-Kraft zwingt zu einer solchen Analyse. Im Gegensatz zu analytischen Modellen, die an konkrete Geometrien gebunden sind, kann der Einfluss geometrischer Faktoren genau untersucht werden. Die Potential- und Konzentrationsabweichungen der Ladunsträger, unter dem Einfluss eines magnetischen Feldes können besser analysiert werden, wenn Simulationsergebnisse sowohl bei Raumtemperatur als auch bei Temperatur von flüssigem Stickstoff (Nitrogen) vorliegen.

In dieser Dissertation werden Simulationergebnisse von Split-Drain MAGFETs präsentiert. Die experimentellen Ergebnisse aus Zwei-Drain MAGFETs lassen sich mit Simulationen bei Raumtemperatur und bei Temperatur von flüssigem Stickstoffe (Nitrogen) nachvollziehen. Eine Analyse der relativen Empfindlichkeit, die der hauptsächliche Gütefaktor von magnetischen Sensoren ist, wird für unterschiedliche Vorspannungen und Geometrien von Zwei- und Drei-Drain MAGFETs durchgeführt. Bei der Verwendung einer Diskretisierung, die ein willkürliches magnetisches Feld beachtet, werden die dreidimensionale Simulationen mit MINIMOS-NT durchgeführt.

Abstract

A solid-state magnetic sensor made with semiconductor materials generates an electric signal under the presence of a magnetic induction. This electric signal is the result of the Lorentz force on the mobile carriers and of a series of physical phenomena known as galvanomagnetic effects in semiconductors. A solid-state magnetic sensor is designed in such a way that the interaction between the magnetic induction and the mobile carriers inside the semiconductor material gives a maximum response. The physical properties of the semiconductor material used to build up the sensor play an important role.

The carrier mobility is the most important parameter for building magnetic sensors with semiconductor materials. Because the carrier deflection is proportional to the mobility of the carriers, the higher the mobility, the higher the deflection, and smaller magnetic inductions can be detected. However, building a magnetic sensor with semiconductor materials that offers higher carrier mobilities is expensive and it is only worthwhile if there is no other given choice. Besides, integrating the electronics for the processing of the electric signal in the same chip of the magnetic sensor can be desirable.

Among the various well established semiconductor processes, the complementary metal-oxide-semiconductor (CMOS) technology is the most popular. Mainly based on silicon, one can produce millions of identical devices at very low cost. Building a magnetic sensor with silicon and taking advantage of the CMOS process steps results in low-cost integrated sensors, because the sensor electronics can be easily integrated. But this goal can be only reached if building the sensor structure does not modify the standard steps of the CMOS process. Post-processing steps cannot be made if the building cost of the integrated sensor has to be kept low.

The split-drain magnetic metal-oxide-semiconductor field-effect transistor, MAGFET for short, is the ideal choice for integrated magnetic sensors in CMOS technology. Its fabrication does not need any post-processing step and actually it is full compatible with the CMOS process. The electronics for the processing of the electric signal can be built in the same substrate as for the sensor. Actually, the CMOS technology is optimized for building MOSFETs and the MAGFET functionality is based on the inversion layer of a common MOSFET. However, the carrier mobility in the inversion layer of a MOSFET is not as high as in the bulk of silicon or even, of many other semiconductor materials.

The split-drain MAGFET has its drain split into two or more drains. Under zero magnetic induction operation, the drains equally share the total drain current. If a magnetic induction is applied perpendicular to the inversion layer of a MAGFET, the drain currents experience an imbalance. As a result, a differential current can be measured at the drains. This differential current is proportional to the mobility of the carriers. At room temperature, only large magnetic inductions can be detected. If the device is cooled to liquid Nitrogen temperature, the carrier mobility is increased and the differential current too. As a result, smaller magnetic inductions can be detected. Besides, cryogenic operation of silicon devices offers some advantages, as for example, better signal-to-noise ratios.

For a better understanding of the electro-magnetic interaction inside the semiconductor materials, three-dimensional simulations are required. The vectorial nature of the Lorentz force requires such analysis in the space that three-dimensional simulations can properly make. Also, variations on geometric parameters can be better analyzed, because analytical approximations does not take properly into account such variations. Details on the potential and carrier concentration under the presence of a magnetic induction can be better understood if simulations are carried out at both, room temperature and liquid Nitrogen temperature.

This thesis presents simulation results of split-drain MAGFETs. Measurements of two-drain MAGFETs are accurately reproduced by simulations at both, room temperature and liquid Nitrogen temperature. An analysis of the relative sensitivity, the main figure of merit of magnetic sensors, is made at various bias and geometric conditions for two-drain and three-drain MAGFET structures. By means of a discretization scheme that takes into account an arbitrary magnetic field, three-dimensional simulations have been performed with MINIMOS-NT.

Resumen

Los sensores magnéticos de estado sólido fabricados con materiales semiconductores generan una señal eléctrica cuando son sometidos bajo la influencia de un campo magnético. Esta señal eléctrica es el resultado de una serie de efectos físicos dentro del material semiconductor conocidos como efectos galvanomagnéticos, que son a su vez resultado de la fuerza de Lorentz sobre las cargas en movimiento dentro del cuerpo del sensor. Los sensores magnéticos de estado sólido se diseñan de tal forma que las cargas en movimiento dentro del semiconductor experimentan la mayor desviación posible cuando se aplica un campo magnético. Las propiedades físicas del material semiconductor son de suma importancia para construir sensores magnéticos.

La movilidad de los portadores es uno de los parámetros más importantes para fabricar sensores magnéticos con materiales semiconductores. Debido a que la desviación de los portadores es directamente proporcional a la movilidad, mientras más alto sea este valor, más fuerte será esta desviación, y por lo tanto se puede detectar campos magnéticos más débiles. Sin embargo, es muy caro fabricar sensores magnéticos con materiales semiconductores que tienen valores altos de movilidad de los portadores y solo se fabrican si no hay otra alternativa disponible. Además, es deseable integrar en la misma pastilla de material semiconductor la electrónica para el proceso de la señal eléctrica y el cuerpo del sensor.

La tecnología de metal-óxido-semiconductor complementaria (CMOS) es la tecnología de material semiconductor más popular y barata entre las diferentes tecnologías de materiales semiconductores. Usando principalmente silicio como material semiconductor, esta tecnología puede producir miles o millones de dispositivos electrónicos idénticos a precios relativamente bajos. Fabricar un sensor magnético de silicio con la tecnología CMOS es económico porque la electrónica del sensor se puede fabricar fácilmente en el mismo circuito integrado. Pero esto solo se puede lograr si la fabricación del cuerpo del sensor magnético se realiza sin modificar los pasos de fabricación de la tecnología CMOS. Cualquier modificación en el proceso de fabricación estándar no pueden realizarse sin encarecer el precio final del sensor integrado.

La estructura de drenaje dividido de un transistor de efecto de campo metal-óxido-semiconductor, MAGFET, es la alternativa ideal para fabricar sensores magnéticos integrados con la tecnología CMOS. Su fabricación no necesita ningún proceso extra de fabricación dentro del proceso CMOS ya que es 100 % compatible. Se puede fabricar la electrónica para procesar la señal eléctrica en el mismo substrato que el del sensor. De

hecho, la tecnología CMOS está diseñada para construir MOSFETs de alto rendimiento y el principio de funcionamiento de un MAGFET aprovecha la capa de inversión de un MOSFET común. Sin embargo, la movilidad de los portadores en esta capa de inversión no es tan alta como en el substrato del silicio o de otros materiales semiconductores.

La estructura MAGFET tiene su drenaje dividido en dos o más partes. En ausencia de un campo magnético, la corriente total se reparte equitativamente entre los diferentes drenajes. Si se aplica un campo magnético perpendicular respecto de la capa de inversión de un MAGFET, las corrientes de drenaje dejan de ser iguales. Entonces se puede medir un diferencial de corriente entre dos drenajes, que es directamente proporcional a la movilidad de los portadores. A temperatura ambiente solo pueden detectarse campos magnéticos fuertes, pero si se congela la estructura del MAGFET a temperatura del nitrónego líquido, la movilidad de los portadores se incrementa, así como el diferencial, por lo tanto, se pueden detectar campos magnéticos débiles. Además, la operación criogénica de dispositivos de silicio ofrece muchas otras ventajas, como por ejemplo una mejor razón de señal-ruido.

Para entender mejor la interrelación entre las fuerzas eléctricas y magnéticas dentro del material semiconductor se necesitan simulaciones en tres dimensiones. La naturaleza vectorial de la fuerza de Lorentz obliga a este tipo de análisis. Además, se pueden analizar mejor las variaciones en los parámetros geométricos ya que los modelos analíticos se han desarrollado para geometrías específicas. Se pueden analizar mejor las variaciones del potencial y de la concentración de los portadores bajo la presencia de un campo magnético si se dispone de resultados de simulación a temperatura ambiente y temperatura del nitrógeno líquido.

En esta tesis se presentan resultados de simulación de MAGFETs. Los datos experimentales de MAGFETs de dos drenajes han sido bien reproducidos con las simulaciones tanto a temperatura ambiente como a temperatura del Nitrógeno líquido. Se analiza la sensibilidad relativa bajo diferentes condiciones de polarización y parámetros geométricos ya que ésta es una de las principales figuras de mérito de los sensores magnéticos. Se ha programado un procedimiento de discretización que toma en cuenta un campo magnético arbitrario, y con ayuda de éste se han realizado simulaciones en tres dimensiones usando el simulador de dispositivos MINIMOS-NT.

Acknowledgment

First of all I would like to thank my adviser Prof. Dr. Siegfried Selberherr for accepting me at the Institute for Microelectronics and helping me to solve the paper work problems at the TU Vienna. His leadership skills have made possible to create an incredible working environment at the institute that every student can ever dream of for their dissertation. His worldwide contacts at both the semiconductor industry and the academy have given to me this incredible opportunity. Also, I want to thank Dr. Edmundo A. Gutiérrez-Domínguez, because actually he put me in contact with the people of the Institute.

I wish to thank all my colleagues at the institute for an excellent working atmosphere and innumerable discussions about microelectronics, computer technologies, and also for their assistance. First of all I want to thank Robert Klima who has spent a lot of time explaining me how the programming environment works at the Institute, setting up my computer machine, installing all the modules and compiling it before I had a slight idea of how to make all of this by myself. Besides, I am grateful to him because he spent a lot of time helping me to solve many bureaucratic paper work at various Austrian offices before I could say *Grüß Gott* in perfect Vienesse.

Thanks to Michael Stockinger who introduce me to the `makedevice` program and actually taught me how to use many features of the MINIMOS-NT simulator. Also, thanks to Christian Troger for helping me to install all the software in my computer, to Robert Mlekus for setting up the CVS environment in my home directory, and to Tom Binder for letting me to run some simulations on his computer although he was not willing to allow it. I wish to thank to Robert Kosik for answering my philosophical questions about Vienna and Austria.

I am grateful to Vassil Palankovski who made for me the first arrangements at the University. Also, his incredible knowledge about the MINIMOS-NT source code has helped me not to mess around with. Thanks to Prof. Tibor Grasser for his general introduction to the discretization scheme used in MINIMOS-NT and Prof. Hans Kosina for his German-English lectures in TCAD. Thanks to Jong-Mun Park for sharing with me his experience in the microelectronics industry. To my roommates, Clemens Heitzinger, Hajdin Ceric, and Stephan Wagner mainly for letting me practice my poor German.

I wish to thank Andreas Gehring for accurately and diligently proof reading my thesis. Thanks to Igor Sosa Mayor for the German translation of the abstract and the proof

reading of the Spanish translation. Thanks to Klaus Dragosits for his general comments on my thesis and the proof reading of the abstract in the German translation. Also, I want to thank him and his girlfriend Christiane for the most enjoyable evening at the Techniker Ball 2002. Thanks to Johann Cervenka, Christian Harlander, and Rainer Sabelka for fixing the network, installing software or just going for a beer. Thanks to Michail Nedjalkov for pointing out the difference between loser doctors and just doctors.

To all of my friends I have made in Vienna, I wish to thank you all of you. You have been like my family in Vienna all those years. Specially thanks to my parents and my sister in Mexico. They believe in me and their support, although they have not been here, is greatly appreciated.

Contents

List of Figures

Chapter 1

Introduction

1.1 Solid-State Sensors

A sensor is a device which detects or measures a physical property and records, indicates, or responds to it. Solid-state sensors have no mobile parts and they must not be confused with transducers or actuators which react depending on the sensor response. Between sensor and actuator, a signal processing unit controls the whole system (Figure 1.1). Because the signal processing unit can be built as a semiconductor device, it is desirable to have the sensor device and the signal processing unit on the same chip. Integrated sensors can be built by taking advantage of semiconductor technology [15].

Integrated sensors offer cheap solutions for controlling industrial processes and they are a good choice for medical applications. For any given application, the strength of a physical quantity should be measured. A solid-state sensor is designed in such a way that the measurand, the physical property to be sensed, exploits a physical phenomenon within the sensor structure. This physical phenomenon leads to an electrical response that can be detected and magnified with electronics. However, the design of such an integrated sensor must be accomplished under some restrictions.

From the process and cost viewpoint, the sensor structure must be manufactured without modifications to the process flow in a mass production batch. Device fabrication must be fully compatible with standard process conditions. Integrating the bias and control circuitry will be straightforward. Unless the packaging material properties affect

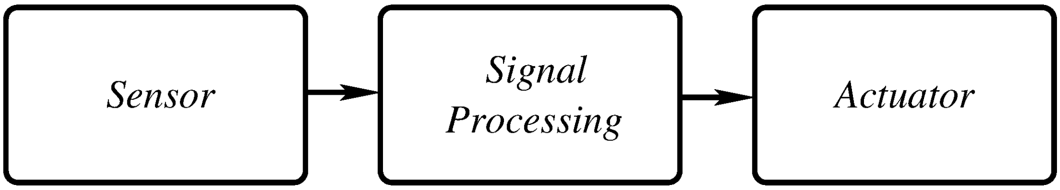

Figure 1.1: Block diagram of a sensor system.

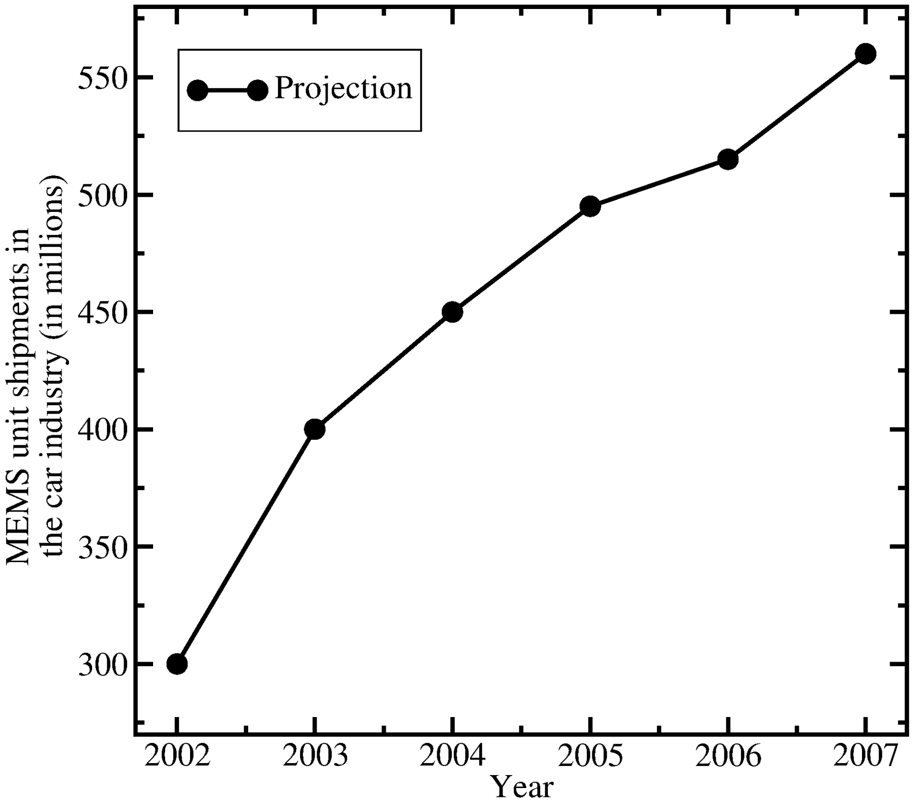

Figure 1.2: Projection of the micro electro-mechanical sensor (MEMS) unit shipments in the car industry versus year.

the sensor behavior, the standard packing process can be used. This allows to build low-cost sensors with standard semiconductor processes.

From the design viewpoint, the sensor structure should take advantage of the process steps and of the various electronic devices that can be built. Full numerical simulations must be carried out in order to better analyze and predict the behavior of a given sensor. Simplifications will not work, because they do not take properly into account effects like temperature or doping profile variations. Besides, the measurand is not implicitly present in the partial differential equations that must be solved, making the design process complex.

All of the above steps impact the design cycle of any integrated sensor. Monolithic integration of sensors is of great interest for the microelectronics industry, because it will provide cheap and reliable sensors [15]. According to In-Stat/SMR [1], despite the growing demand of the car industry (see Figure 1.2), to date, only a few sensor devices have been integrated into a high-volume production IC process.

There are several drawbacks that refrain the monolithic integration of sensor devices into IC chips. Packaging, thermal management, noise, cross-talk, are some of the drawbacks

---

[1] `http://www.instat.com`

that must be overcome before getting integrated sensor devices into mass production. However, more fundamental research must be first done before attempting to transfer a sensor device into mass production. This is the case of magnetic sensors that might also find a wider opportunity in the car industry. Thus, this thesis attempts to fulfill that lack of fundamental research by providing a full three-dimensional numerical simulation tool with magnetic effects.

1.2 Magnetic Sensors

Various classifications for sensors have been made [36, 40]. A magnetic sensor converts a magnetic field into an electrical signal. Two applications can be distinguished for the magnetic sensors. In direct applications the magnetic sensor is part of a magnetometer. Examples are the geomagnetic field measurements, the reading of magnetic data storage media, the identification of magnetic patterns in cards and banknotes, and the control of magnetic apparatus. In indirect applications the magnetic field is used as an intermediary carrier for detecting non-magnetic signals. Examples are potential-free current detection for overload protection, integrated watt-hour meters, and contactless linear or angular position, displacement, or velocity detection using a permanent magnet. These applications require the detection of magnetic fields in the micro- and millitesla range, which can be achieved by integrated semiconductor sensors.

In the case of solid-state magnetic sensors such as MAGFETs, the *measurand* is the magnetic induction **B**

$$\mathbf{B} = \mu\mu_0\mathbf{H}. \tag{1.1}$$

B is the magnetic induction in Tesla units (Vs/m^2), **H** is the magnetic field vector, μ_0 denotes the permeability of free space, and μ is the relative permeability. Silicon is a low-permeability material, that is, μ is approximately one.

1.3 Magnetic Effects in Semiconductors

Galvanomagnetic effects are exploited in solid-state magnetic sensors. They are the result of the magnetic induction on mobile carriers through the Lorentz force

$$\mathbf{F} = q \cdot (\mathbf{v} \times \mathbf{B}) \tag{1.2}$$

where q is the electronic charge and $\mathbf{v}$ denotes the velocity of the carriers.

Four different effects arise when a magnetic induction is applied to a semiconductor device carrying a current: a Hall voltage, a carrier deflection, a magnetoconcentration, and a magnetoresistance. The last one gives a quadratic response to the magnetic induction whereas the others result in a linear response. A solid-state magnetic sensor is designed in such a way that one or several of those effects are maximized within the device body.

Galvanomagnetic effects are used as a classification of solid-state magnetic sensors. Hall devices exploit the Hall effect. Magnetotransistors use the magnetoconcentration and carrier deflection. MAGFETs use carrier deflection as the physical effect to detect a magnetic field. This is not a fully appropriate classification of the solid-state magnetic sensors, because it is not clear that only one of such galvanomagnetic effects would prevail over the others. Besides, the solid-state magnetic sensors must fulfill some other specifications depending on their application.

1.4 Specifications of Magnetic Sensors

The selection of the appropriate sensor design and technology depends on a number of further specifications that may vary widely from one application to another. Solid-state magnetic sensors are characterized by using some figures of merit, such as

- availability and cost of technology
- application environment: temperature, humidity and chemical stress, vibrations and mechanical stress
- geometry: field parallel or perpendicular to chip surface
- sensitivity, signal level
- magnetic field resolution, signal-to-noise ratio: accuracy (absolute) and precision (relative)
- spatial resolution
- time resolution, frequency response
- linearity of magnetic response
- temperature coefficient of sensitivity
- offset and its temperature dependence
- power consumption, size, weight
- electrical input and output impedance
- stability, reliability, lifetime
- testability of above specifications

1.5 Magnetic MOS Field-Effect-Transistor

The inversion layer of a metal-oxide-semiconductor field-effect-transistor (MOSFET) can be used as the active region of a magnetic sensor [14]. This active region can exploit the Hall effect for Hall based sensors, or the carrier deflection, if the device has a split-drain (See Figure 1.3). A split-drain MOSFET structure is called MAGFET if it is used as a magnetic sensor.

One of the main advantages of a MAGFET is its compatibility with the CMOS process without the need for post-processing steps. Very low power consumption can be achieved with this technology. The ability of integrating the bias and control circuitry on the same chip makes this device structure particularly attractive. However, the most serious drawback of the MAGFET is its $1/f$ noise. Also, the electron mobility of the inversion layer is relatively low, which results in limited sensitivity of the whole structure, making it only useful for large magnetic induction in the 100 mT range.

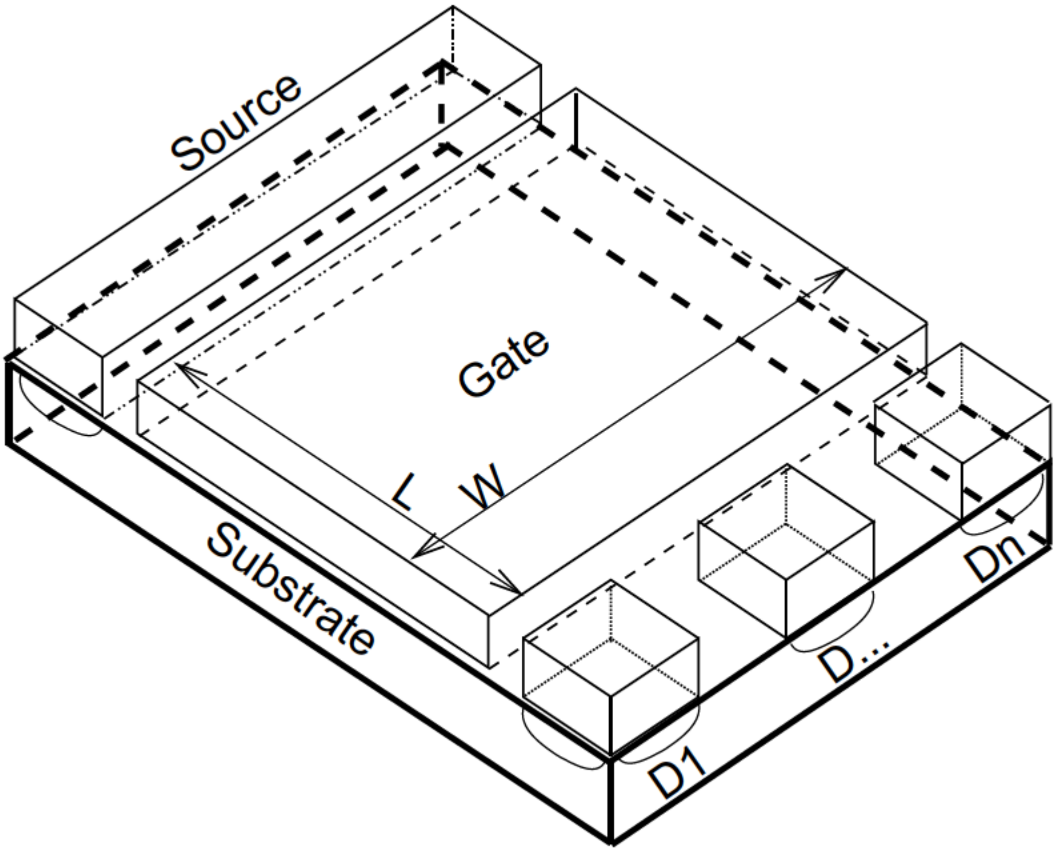

Figure 1.3: Split-drain MOSFET structure.

All these features point out that the MAGFET structure is not the proper sensor selection for a range of applications. However, if the solid-state magnetic sensor is cooled down to 77 K, many figures of merit are greatly improved [16]. The $1/f$ noise is lowered and the electron mobility of the inversion layer is increased, which results in increased sensitivity and allows detection in the sub-mT range. Cooling down the solid-state sensor will impact other figures, such as weight and cost. However, cooling down to 77 K (liquid Nitrogen temperature) is cheaper as compared to 4.2 K (liquid Helium temperature), the operating temperature used for most superconducting quantum interference devices (SQUID) which are capable of resolving the picotesla fields occurring in biomagnetometry [12].

Additionally, manufacturing the MAGFET in CMOS technology implies the use of silicon as the detector material. Although InSb or GaAs offer higher mobilities in n-type materials than Si, some other properties of InSb and GaAs make the choice of silicon straightforward [5, 24, 33].

1.6 Organization of the Thesis

The main goal of this thesis is to enhance MINIMOS-NT, a general purpose device simulator, to simulate the electro-magnetic performance of a split-drain MAGFET operated at 300 K and 77 K. For this purpose, full three-dimensional numerical simulations must be carried out. In Chapter 2 the magnetic effects in semiconductors are described, showing the equations that must be solved for the simulation of magnetic effects in semiconductors. Details of the implementation in MINIMOS-NT will be shown in Chapter 3, along with the discretization scheme for computing the vectorial product between current density and magnetic field. Chapter 4 presents results of a two-drain MAGFET at 300 K and 77 K. Chapter 5 gives results of a three-drain MAGFET at 300 K and 77 K, and finally some conclusions are drawn in Chapter 6.

Chapter 2

Galvanomagnetic Effects in Semiconductors

2.1 Introduction

Moving charges in a magnetic field experience the Lorentz force. In modeling this effect, a mathematical description is necessary. The following sections show the development of a general model that takes into account the thermoelectric, thermomagnetic, and galvanomagnetic effects in semiconductors.

2.2 Formal Transport Theory

The behavior of solid-state matter under the influence of external fields is one main subject of solid-state physics. The external field may be an electric field, a magnetic field, an optical signal, or a temperature gradient. Those external fields modify the distribution of the internal energy which in turn modifies or alters some electronic properties, such as the carrier concentration or the carrier mobility.

Besides the carrier mobility the electric current is also affected by the magnetic field by deflecting its direction. Modeling the electric current implies to determine the number of electrons with given momentum at a given location as a function of time. Those distribution functions are modeled by solving the Boltzmann equation and with them the electron and energy transport equations are derived. The transport equations can be obtained from the thermodynamics of irreversible processes. The advantage of this solution is a direct evaluation of the equation coefficients with respect to the driving forces, and a direct link to experiments [22].

2.3 The Thermodynamic Model

In [44] Wachutka regards the semiconductor material as a composite thermodynamic system which comprises the subsystems of electrons, holes, and host lattice. These three subsystems are affected by the action of external fields and interact with each other according to certain rules. For example, particle flow between holes and electrons is governed by recombination processes; or lattice scattering enables energy transfer between the carriers and the lattice.

The whole semiconductor can be uniquely characterized by a set of state variables which are position and time dependent. In semiconductor modeling these variables are the quasi Fermi levels, the carrier temperature, and the lattice temperature. The quasi Fermi level is the sum of a chemical potential and an electric potential where the former is a local function of the carrier density and temperature, while the latter is determined via the Poisson equation [43].

2.4 General Form of the Transport Equations

2.4.1 Fluxes and Forces

The external fields modify the internal energy of the semiconductor, which defines the variables representing the thermodynamic system. The fluxes are the response to the forces that interact with the thermodynamic model of the system. They are the hole current, the electron current, and the total energy. The forces, also called affinities, are the gradients of the quasi Fermi levels and the temperature [22, 34].

2.4.2 The Onsager Relations

The thermodynamics of irreversible processes postulates that, when local entropy production is represented as a sum of products of fluxes and forces, both must be linearly related to each other [22]. This can be expressed in the form

$$\frac{\delta\alpha_i}{\delta t} = \sum_j L_{i,j}\gamma_j \tag{2.1}$$

where the α_i are a set of measurable parameters of the system, the $L_{i,j}$, or ”kinetic coefficients”, are a function of the state of the system, depending from the external fields, and

$$\gamma_j \equiv \frac{\delta S}{\delta\alpha_j} \tag{2.2}$$

with S being the entropy of the system.

In equilibrium the entropy S is a maximum and the γ_j are therefore zero. Thus the γ_j are a measure of the deviation from the equilibrium state. If the $L_{i,j}$ were to be zero for all $i \neq j$, each flux $\delta\alpha_j/\delta t$ would depend only on its own driving force γ_j, and the various processes could be considered as independent. Thus the quantities $L_{i,j}$ are a measure of the interference of the jth process with the ith process [7].

Onsager's theorem states that

$$L_{i,j}(\mathbf{B}) = L^T_{j,i}(-\mathbf{B}) \tag{2.3}$$

where $\mathbf{B}$ is the applied magnetic field. Even if the magnetic field is reversed, the symmetry in the mutual interference of two or more irreversible processes will prevail [7, 28, 29].

The structure of the $L_{i,j}$ highly depends on the system. If the medium is anisotropic, the $L_{i,j}$ are tensors, and the $L_{i,j}$ become scalars if the medium is isotropic.

2.4.3 General Transport Equations

Following Onsager's general formalism, the electron and hole current densities, $\mathbf{J_n}$ and $\mathbf{J_p}$, and the heat fluxes of the individual subsystems, $\mathbf{Q_n}$, $\mathbf{Q_p}$, and $\mathbf{Q_L}$, are related to the gradients of the state variables by a 15 × 15 matrix:

$$\begin{pmatrix} \mathbf{J_n} \\ \mathbf{Q_n} \\ \mathbf{J_p} \\ \mathbf{Q_p} \\ \mathbf{Q_L} \end{pmatrix} = \begin{pmatrix} L_{1,1} & L_{1,2} & \dots & L_{1,5} \\ L_{2,1} & L_{2,2} & \dots & L_{2,5} \\ \vdots & \vdots & \ddots & \vdots \\ L_{5,1} & L_{5,2} & \dots & L_{5,5} \end{pmatrix} \begin{pmatrix} \nabla\phi_n \\ \frac{1}{T_n}\nabla T_n \\ \nabla\phi_p \\ \frac{1}{T_p}\nabla T_p \\ \frac{1}{T_L}\nabla T_L \end{pmatrix} \tag{2.4}$$

The 3 × 3 sub matrices $L_{\alpha,\beta}$ depend on the quasi-static magnetic field $\mathbf{B}$. Those kinetic coefficients, better known as transport matrices $L_{\alpha,\beta}$, are computed taking into account the reciprocity fact of Onsager's theorem and assuming cubic or higher spatial symmetry of the semiconductor medium. A general structure is as follows:

$$L_{\alpha,\beta}(\mathbf{B}) = a_{\alpha,\beta}(B^2)I + b_{\alpha,\beta}(B^2)(\mathbf{B}\times\cdot) + c_{\alpha,\beta}(B^2)(\mathbf{B}\times\cdot)^2 \tag{2.5}$$

where $a_{\alpha,\beta} = a_{\beta,\alpha}$, $b_{\alpha,\beta} = b_{\beta,\alpha}$, and $c_{\alpha,\beta} = c_{\beta,\alpha}$ are scalar functions of $|B^2|$, and the symbol $(\mathbf{B}\times\cdot)$ denotes the linear operation of taking the vector product of $\mathbf{B}$ and an arbitrary vector. In matrix representation it reads

$$(\mathbf{B}\times\mathbf{k}) = \begin{pmatrix} 0 & -B_z & B_y \\ B_z & 0 & -B_x \\ -B_y & B_x & 0 \end{pmatrix} \begin{pmatrix} k_x \\ k_y \\ k_z \end{pmatrix} \tag{2.6}$$

The coefficients $a_{\alpha,\beta}$, $b_{\alpha,\beta}$, and $c_{\alpha,\beta}$ can be given as a parametrization of physical quantities, accessible by measurement and commonly used for the characterization of material properties [7, 8]. These are the electric conductivities σ_n and σ_p, the thermal conductivities κ_n, κ_p, and κ_L, and the coefficients describing the thermoelectric, galvanomagnetic, and thermomagnetic effects, namely the thermopowers P_n and P_p, the Hall coefficients R_n and R_p, the Nernst coefficients η_n and η_p, and the Righi-Leduc coefficients $\mathcal{L}_n$ and $\mathcal{L}_p$ [22, 37, 44].

2.4.4 Transport Coefficients without a Magnetic Field

If the magnetic field is zero, the transport coefficients are multiples of basic driving forces. Equivalently, the transport coefficients are symmetric tensors. Three of them can be identified.

Heat Conductivity

The isothermal heat conductivity of electrons (holes) κ_n (κ_p) describes the electron (hole) heat current density $\mathbf{Q_n}$ ($\mathbf{Q_p}$) driven by a temperature gradient ∇T under zero current conditions:

$$\kappa_{n,p} = -\frac{\mathbf{Q_{n,p}} \cdot \nabla T}{|\nabla T|^2} \quad \text{with} \quad \mathbf{J_{n,p}} = 0 \tag{2.7}$$

Electric Conductivity

The isothermal electric conductivity of the electrons (holes) σ_n (σ_p) describes the electron (hole) current $\mathbf{J_n}$ ($\mathbf{J_p}$) driven by a gradient of the quasi Fermi level; the inverse of σ_n (σ_p) is defined as

$$\sigma_{n,p}^{-1} = -\frac{\mathbf{J_{n,p}} \cdot \nabla \phi_{n,p}}{|\mathbf{J_{n,p}}|^2} \quad \text{with} \quad \nabla T = 0 \tag{2.8}$$

Thermoelectric Power

The absolute thermoelectric power P_n (P_p) characterizes the gradient of the quasi Fermi potential $\nabla \phi_n$ ($\nabla \phi_p$) induced by a temperature gradient under zero current conditions:

$$P_{n,p} = -\frac{\nabla \phi_{n,p} \cdot \nabla T}{|\nabla T|^2} \quad \text{with} \quad \mathbf{J_{n,p}} = 0 \tag{2.9}$$

2.4.5 Transport Coefficients with a Magnetic Field

Even if the medium is isotropic, the transport coefficients in presence of a magnetic field show an asymmetry. The way in which driving force and magnetic field are oriented (perpendicular or parallel with respect to each other) implies a non-symmetric tensor representation of the transport coefficients that can be written as

$$L = L_{\perp}(1 - P_B) + L_{||}P_B \tag{2.10}$$

where P_B denotes the operation of projecting a vector along the direction of B.

The transport coefficients with magnetic field are the following:

Hall Coefficients

The isothermal Hall coefficients R_n (R_p) characterize the transverse quasi Fermi level gradient caused by the magnetic field acting on the electron (hole) current:

$$R_{n,p} = -\frac{\nabla\phi_{n,p} \cdot (\mathbf{B} \times \mathbf{J_{n,p}})}{(\mathbf{B} \times \mathbf{J_{n,p}})^2} \quad \text{with} \quad \nabla T = 0 \tag{2.11}$$

Nernst Coefficients

The isothermal Nernst coefficients η_n (η_p) characterize the transverse gradient of the quasi Fermi potential caused by the deflection of an electron (hole) heat current flowing 'down a temperature gradient':

$$\eta_{n,p} = -\frac{\nabla\phi_{n,p} \cdot (\mathbf{B} \times \nabla T_{n,p})}{(\mathbf{B} \times \nabla T_{n,p})^2} \quad \text{with} \quad \mathbf{J_{n,p}} = 0 \tag{2.12}$$

Righi-Leduc Coefficients

The Righi-Leduc coefficients $\pounds_n$ ($\pounds_p$) characterize the transverse temperature gradient caused by the deflection of an electron (hole) heat current flowing 'down a temperature gradient':

$$\pounds_{n,p} = \frac{\nabla T \cdot (\mathbf{B} \times \mathbf{Q_{n,p}})}{(\mathbf{B} \times \nabla T) \cdot (\mathbf{B} \times \mathbf{Q_{n,p}})} \quad \text{with} \quad \mathbf{J_{n,p}} = 0 \tag{2.13}$$

2.5 Compact Vector Formulation

The inversion of (2.4) will give us a better representation of the driving forces with respect to the fluxes. Making use of all the definitions given in the previous chapter, the current relations can be rewritten in a very compact formulation.

$$\nabla\phi_n = -\sigma_n^{-1}\mathbf{J_n} - P_n\nabla T_n - \mathbf{B} \times (R_n\mathbf{J_n} + \eta_n\nabla T_n) \tag{2.14}$$

$$\mathbf{Q_n} = P_nT_n\mathbf{J_n} - \kappa_n\nabla T_n + \mathbf{B} \times (\eta_nT_n\mathbf{J_n} + \kappa_n\pounds_n\nabla T_n) \tag{2.15}$$

An expansion of $\nabla\phi_n$ and $\nabla\phi_p$ in terms of electric potential ψ, carrier concentrations, and temperature reveals that actually drift, chemical diffusion, and thermal diffusion appear as driving forces. The deflection that the magnetic field causes on electric and thermal currents is reflected by vector products with **B**. Solving (2.14) for the current density $\mathbf{J_n}$ yields

$$\begin{aligned}\mathbf{J_n} = &-\sigma_n(\nabla\phi_n + P_n\nabla T) - \sigma_n\frac{1}{1+(\mu_n^*\mathbf{B})^2}\{\mu_n^*\mathbf{B}\times\nabla\phi_n + (\eta_n + \mu_n^* P_n)\mathbf{B}\times\nabla T\}\\ &-\sigma_n\frac{\mu_n^*}{1+(\mu_n^*\mathbf{B})^2}\{\mu_n^*\mathbf{B}\times(\mathbf{B}\times\nabla\phi_n) + (\eta_n + \mu_n^* P_n)\mathbf{B}\times(\mathbf{B}\times\nabla T)\}\end{aligned} \tag{2.16}$$

with $\mu_n^* = r_n \cdot \mu_n$ denoting the Hall mobility of electrons [37].

The current density $\mathbf{J_p}$ reads

$$\begin{aligned}\mathbf{J_p} = &-\sigma_p(\nabla\phi_p + P_p\nabla T) - \sigma_p\frac{1}{1+(\mu_p^*\mathbf{B})^2}\{\mu_p^*\mathbf{B}\times\nabla\phi_p + (\eta_p + \mu_p^* P_p)\mathbf{B}\times\nabla T\}\\ &-\sigma_p\frac{\mu_p^*}{1+(\mu_p^*\mathbf{B})^2}\{\mu_p^*\mathbf{B}\times(\mathbf{B}\times\nabla\phi_p) + (\eta_p + \mu_p^* P_p)\mathbf{B}\times(\mathbf{B}\times\nabla T)\}\end{aligned} \tag{2.17}$$

with $\mu_p^* = r_p \cdot \mu_p$ denoting the Hall mobility of holes [37].

2.6 The Isothermal Approximation

Although the present thesis deals with the full modeling of magnetic effects in semiconductor devices also at low temperatures, the available experimental data and simulation results show an excellent agreement when (2.16) is applied to the isothermal case. Literature shows that the thermomagnetic effects are orders of magnitude smaller than the Hall voltage [38].

The mathematical model that reproduces the Lorentz force on carriers in semiconductors for the electrons can therefore be simplified to

$$\begin{aligned}\mathbf{J_n} = &-\sigma_n(\nabla\phi_n) - \sigma_n\frac{1}{1+(\mu_n^*\mathbf{B})^2}\{\mu_n^*\mathbf{B}\times\nabla\phi_n\}\\ &-\sigma_n\frac{\mu_n^*}{1+(\mu_n^*\mathbf{B})^2}\{\mu_n^*\mathbf{B}\times(\mathbf{B}\times\nabla\phi_n)\}\end{aligned} \tag{2.18}$$

For holes, the mathematical model reads

$$\begin{aligned}\mathbf{J_p} = &-\sigma_p(\nabla\phi_p) - \sigma_p\frac{1}{1+(\mu_p^*\mathbf{B})^2}\{\mu_p^*\mathbf{B}\times\nabla\phi_p\}\\ &-\sigma_p\frac{\mu_p^*}{1+(\mu_p^*\mathbf{B})^2}\{\mu_p^*\mathbf{B}\times(\mathbf{B}\times\nabla\phi_p)\}\end{aligned} \tag{2.19}$$

Along with the Poisson and continuity equations, a device under the presence of a magnetic field can be properly simulated with the drift-diffusion approximation if the device is sufficiently large [19].

2.7 Boundary Conditions

The boundary conditions that are found in [11, 19] also apply for magnetic effects. However, for galvanomagnetic simulations, a particular problem arises. It is known that when a magnetic field perpendicular to a current distribution is applied, a Hall voltage appears across the device to compensate the deflection of the current. As a-priori rule it should be known where the discretization must be efficiently fine to resolve this Hall voltage. If this is not possible, dense grids must be used in large structures, which results in expensive simulations with a fairly large demand on computational resources.

The Hall field can be computed as

$$\mathbf{E_H} = \frac{\mathbf{J_n} \times \mathbf{B}}{qn} = -R_n(\mathbf{J_n} \times \mathbf{B}) \tag{2.20}$$

This voltage counteracts the Lorentz force and affects the electric potential and the boundary conditions for the Poisson equation.

For the electric potential the Gauß law states that the potential has to be a continuous function when crossing a surface

$$\epsilon_I \frac{\partial \psi}{\partial N}|_I = \epsilon_{II} \frac{\partial \psi}{\partial N}|_{II} + \rho_{\text{surf}} \tag{2.21}$$

where ϵ_I and ϵ_{II} are the respective permittivity constants of the materials adjacent to the interface, and ρ_{surf} is the surface charge density. The non-zero magnetic field differs in the following way.

Computing a fictitious induced surface charge from the Hall field, so that the boundary condition for the electric potential reads:

$$\mathbf{E} \cdot \mathbf{N} = \frac{\rho_{\text{surf}} + \rho_{\text{ind}}}{\epsilon} \tag{2.22}$$

with

$$\rho_{\text{ind}} = \epsilon \mathbf{E_H} \cdot \mathbf{N} \tag{2.23}$$

For general bipolar operating conditions, the isothermal case of the boundary condition for the electric potential is:

$$\begin{aligned}\frac{\partial \psi}{\partial N}|_{sc} = -\frac{\rho_{\text{surf}}}{\epsilon} + \sigma R_H(\mathbf{B} \times \nabla \psi) \cdot \mathbf{N} \\ - \frac{\sigma_n^2 R_n}{\sigma}(\mathbf{B} \times \nabla(\psi - \phi_n)) \cdot \mathbf{N} + \frac{\sigma_p^2 R_p}{\sigma}(\mathbf{B} \times \nabla(\phi_p - \psi)) \cdot \mathbf{N}\end{aligned} \tag{2.24}$$

where $\sigma = \sigma_n + \sigma_p$ is the transversal ambipolar electric conductivity, and

$$R_H = \frac{\sigma_n^2 R_n + \sigma_p^2 R_p}{\sigma^2} \tag{2.25}$$

is the ambipolar Hall coefficient.

The boundary conditions along internal interfaces or contacted outer surface portions are not affected by the magnetic field.

Chapter 3

Implementation

3.1 The Computation of the Vector Product

Proper simulation of semiconductor devices requires solving a set of coupled differential equations. Solving the Poisson and continuity equations implies partitioning the simulation domain into a finite number of subdomains where a solution can be approximated. The way in which a solution is approximated to a device geometry is called discretization. Any discretization needs a mesh, a group of points that defines lines, surfaces, and volumes which covers geometric information about the device geometry under consideration [11].

The discretization of the set of differential equations that describes the behavior of a semiconductor device without magnetic field can be found in several papers [11, 39]. Via the Gauß theorem the divergence of a gradient on volumes is expressed in terms of the fluxes through the surfaces of the volumes [13]. Those *fluxes* are basically current projections along the meshing lines which are computed using the local information found at the end points of a mesh line. Additionally, the points are ordered in such a way that the current projections are diagonal entries in the Jacobian matrix. This eases the solution of the equation system.

Discretization of (2.18,2.19), the equations comprising the magnetic field for the current densities, introduces a serious complication in the discretization procedure: namely the computation of a vector product. With any discretization procedure the only available information is the projection of quantities along the mesh lines. There is no information about either the vector components or the direction of the components. Even worse, if an approximation of such vector components exists, the computation of the vector product will introduce non-diagonal entries in the Jacobian matrix, compromising the existence of a solution [13].

From the programming point of view, the discretization of (2.18,2.19) must be performed without modifying the discretization procedure, that is, the way how the projections are computed along the mesh lines in order to avoid non-diagonal entries in the

Jacobian matrix. Any discretization procedure applied to (2.18,2.19) must prevail the details of the remaining code in any project, for example, the source code of MINIMOS-NT. It is obvious that the new discretization procedure must reduce to the original one when the magnetic field is zero. In the following section a discretization procedure taking into account the magnetic field will be developed based on the proposal of Gajewski and Gärtner [13]. The vectorial product is computed using only the information of the neighboring points, and actually it is not related to the discretization scheme used for computing the current projections along the mesh lines. That is, a drift-diffusion or a hydrodynamic approximation for computing the current projections along the mesh lines can be used together with the new discretization procedure to simulate magnetic effects in semiconductor devices.

The Hall mobilities are computed by means of the Hall scattering factors r_n and r_p. Their values are 1.15 for electrons and 0.8 for holes [4] for bulk silicon at room temperature. Jungemann *et. al* [18] give values for the Hall scattering factor for electrons in inversion layers at different temperatures and electric fields (see Figure 3.1).

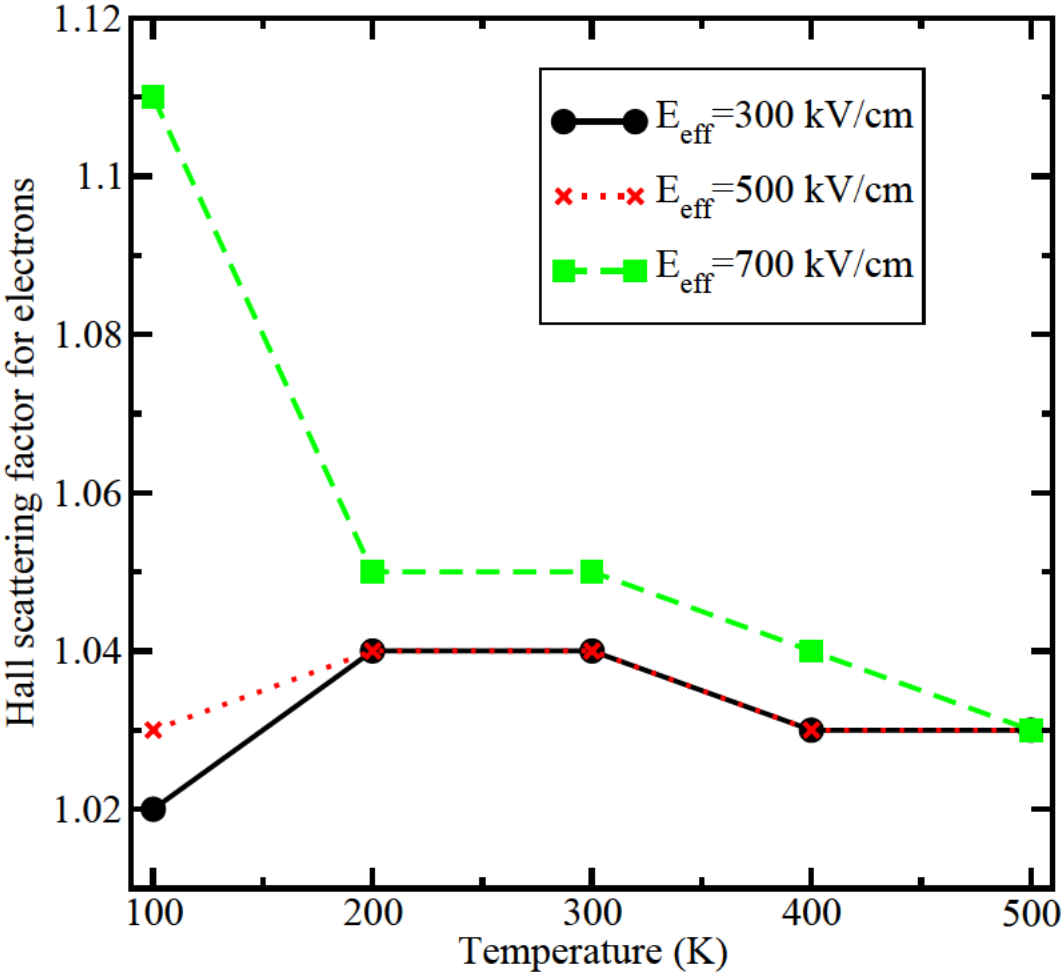

Figure 3.1: Hall scattering factor for electrons versus temperature (after [18]).

3.2 The New Discretization Procedure

The expression (2.18,2.19) result from solving the implicit expression

$$\mathbf{J}^0 = \mathbf{J} + \mu^* \mathbf{J} \times \mathbf{B} \tag{3.1}$$

where $\mathbf{J}$ is the current density including the galvanomagnetic effects, and $\mathbf{J}^0$ is the current density for zero magnetic field.

The previous equation can be written in matrix notation

$$\mathbf{J}^0 = \mathbf{A}\mathbf{J} \tag{3.2}$$

with $\mathbf{A}$ being an operator in the three-dimensional space. Inverting the previous expression one gets

$$\mathbf{J} = \mathbf{A}^{-1}\mathbf{J}^0 \tag{3.3}$$

thus $\mathbf{A}$ is an operator whose inverse applied to the zero magnetic field current $\mathbf{J}^0$ gives the deflected current $\mathbf{J}$. In spatial components, $\mathbf{A}$ is formed with the product between the magnetic vector and the Hall mobilities $\mu^*\mathbf{B}$. The symbol β will be used to represent this dimensionless product, so $\mathbf{A}$ reads

$$\mathbf{A} = \begin{pmatrix} 1 & \beta_z & -\beta_y \\ -\beta_z & 1 & \beta_x \\ \beta_y & -\beta_x & 1 \end{pmatrix} \tag{3.4}$$

$\mathbf{A}^{-1}$ can be expressed as

$$\mathbf{A}^{-1} = \frac{\mathbf{I} + \beta\beta^T + \beta\times}{1 + |\beta|^2} \tag{3.5}$$

where $\mathbf{I}$ is the identity matrix, $|\beta|^2 = \beta_x^2 + \beta_y^2 + \beta_z^2$, and $\beta\times$ as shown in (2.6).

The explicit components of each vector in (3.3) must be replaced by the current projections, because this is the only available information that any discretization procedure provides. So, $\mathbf{J}^0$ is transformed to $\mathbf{J}_k^0$ where the subindex k is the index of a *simplex,* a grid point which includes its neighboring points (See Figure 3.2). $\mathbf{J}_k^0$ has all the current projections from a k simplex, from the point i to the neighboring points j.

$$\mathbf{J}_k = \mathbf{A}^{-1}\mathbf{J}_k^0 \tag{3.6}$$

Because a k simplex could have any number of neighboring points, $\mathbf{J}_k^0$ must hold the same number of current projections too. So, (3.3) must be modified accordingly. Expression (3.5) gives a 3 × 3 matrix unless an operation is introduced in such a way that it gives a square matrix with the same number of current projections of a k simplex. This is done by introducing a transformation matrix $\mathbf{N}$ composed of the unitary vectors which are computed from the point i to every neighboring point j.

$$\mathbf{N} = \sum_j n_{i,j} \tag{3.7}$$

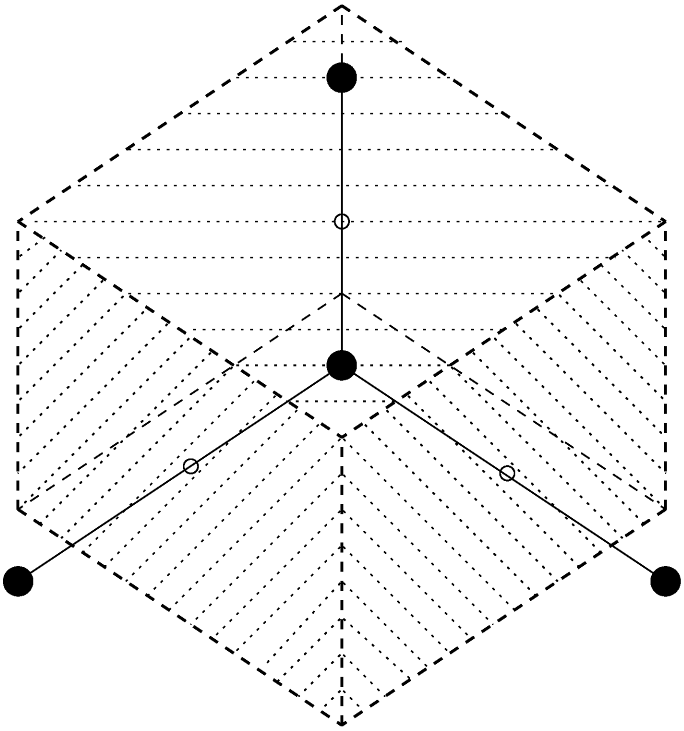

Figure 3.2: Cubic representation of a k-simplex with its Voronoi volume.

Introducing the transformation matrix $\mathbf{N}$ in (3.5), and replacing in (3.6) one gets

$$\mathbf{J}_k = \frac{(\mathbf{I} + \mathbf{N}^T(\beta\beta^T + \beta\times)\mathbf{N}^{-T})\mathbf{J}^0}{1 + |\beta|^2} \tag{3.8}$$

The above expression determines a matrix which combines n current projections with the components of a magnetic field. However, the neighboring points j of the point i for every simplex k can be arbitrarily placed in the simulation domain. Care must be taken in this step to obtain the proper weight of current projections with the magnetic field. This is done by means of a matrix multiplication with the $\mathbf{s}_k$ vector whose components are the inverse of the distances between the point i and the neighboring points j.

$$\mathbf{s}_k = \sum_j \frac{1}{d_{i,j}} \tag{3.9}$$

Finally, the discretization procedure taking into account the magnetic field reads

$$\mathbf{J}_k = \frac{s_k^T(\mathbf{I} + \mathbf{N}^T(\beta\beta^T + \beta_\times)\mathbf{N}^{-T})\mathbf{J}^0}{1 + \beta^2} \tag{3.10}$$

This implementation introduces extra entries in the Jacobian matrix, but it guarantees the existence of a solution if the magnetic field times the carrier mobility is much less than one. Also, the grid plays an important role in computing the solution, because the weights of the current projections with the magnetic field can generate large numbers which impact the properties of the Jacobian matrix. This discretization scheme was successfully implemented in MINIMOS-NT [19].

3.3 Previous Attempts

The work of Riccobene [34] was the best attempt to the numerical modeling of galvanomagnetic effects in semiconductors in any dimension where she has simulated magnetotransistors in two and three dimensions. Previous works deal with the discretization of galvanomagnetic effects, actually the Lorentz force on the current density in a surface [1, 3, 26]. All the simulation results are two-dimensional, and in the work [1] the discretization procedure is developed taking into account only one component of the magnetic field and taking advantage of the grid structure. The work of Baltes [3, 25, 32] has been used as a basis of other discretization procedures [21], but all of them are two-dimensional approaches.

All attempts so far are based more or less on the original work by Pfleiderer [30]. Numerous publications can be found since then [9, 23, 31, 41], but all the attempts are based in tearing the domain with discrete components, and only offer a two dimensional approximation of the domain. Neudecker *et al.* have made an attempt in three dimensions [27], but their work is only applicable to Hall plates. The work of Riccobene [34] is based on a general oriented device simulator, as the present thesis, but currently there is no literature dealing with the modeling and simulation of galvanomagnetic effects in three dimensions at low temperatures. Therefore, I tried to cover this lack of information with this thesis.

From the commercial TCAD tools only the device simulator DESSIS from Integrated Systems Engineering [1] is able to simulate magnetic effects in two and three dimensions. The values for the Hall scattering factors are set to the bulk values described in this chapter and successful simulations of magnetotransistors have been obtained [35].

---

[1] `http://www.ise.ch/products/dessis/index.html`

Chapter 4

Two-Drain MAGFET

4.1 The Structure

A two-drain MAGFET is a magnetic sensor based on a MOSFET. Its structure is identical to a MOSFET but the drain is split in two or more parts [25, 33, 42]. In this chapter, a two-drain MAGFET built with a 10 μm standard CMOS process will be analyzed. The substrate doping is of 1×10^{15} cm^{-3} and the oxide thickness is

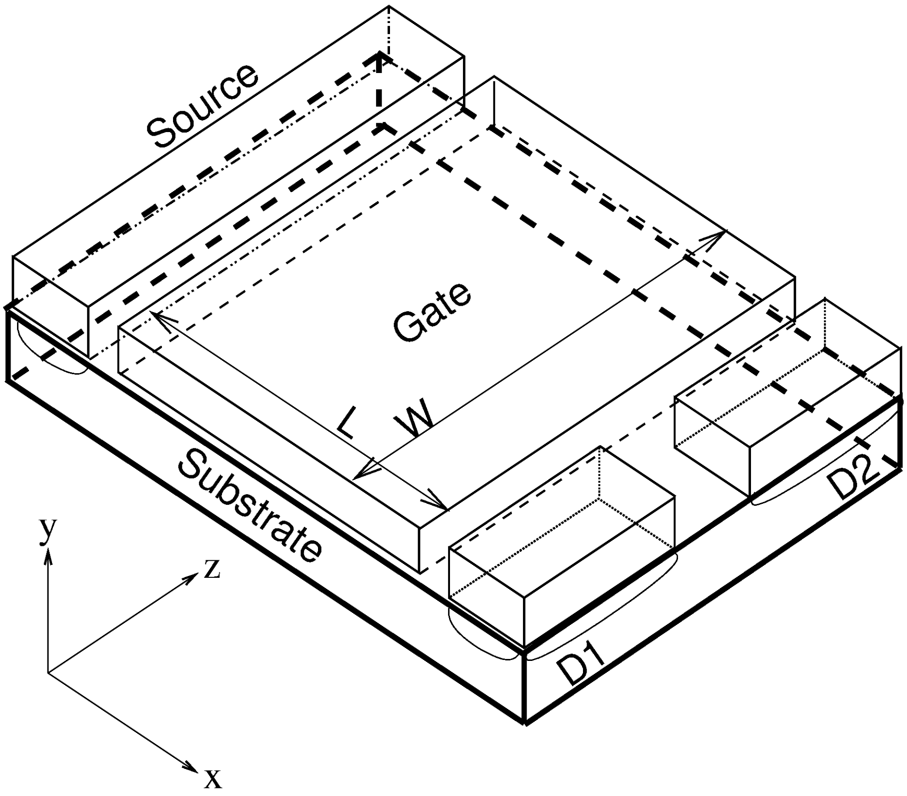

Figure 4.1: Two-drain MAGFET structure.

of 60 nm. The metallurgical junction is of 1 μm and the source/drain doping is of 5×10^{18} cm^{-3}. The structure was built at the National Institute for Astrophysics, Optics, and Electronics (INAOE) Tonantzintla, Puebla, Mexico and measurements were carried out by Dr. Edmundo A. Gutiérrez-Domínguez. Some results are shown in reference [33]. In the following analysis the investigated MAGFET has a W/L ratio of 0.8 ($W = 100\,\mu$m and $L = 125\,\mu$m) and a distance between the drains of $10\,\mu$m.

4.2 Analysis at 300 K

The main figure of merit of a two-drain MAGFET is its differential current related to the magnetic field it is sensing. The relative sensitivity is defined as

$$S_r = \frac{|I_{D1} - I_{D2}|}{(I^0_{D1} + I^0_{D2})|\mathbf{B}|} \tag{4.1}$$

where I_{D1} and I_{D2} are the currents at Drain 1 and Drain 2 when the magnetic field is applied, I^0_{D1} and I^0_{D2} when the magnetic field is not applied, and $\mathbf{B}$ is the magnetic field.

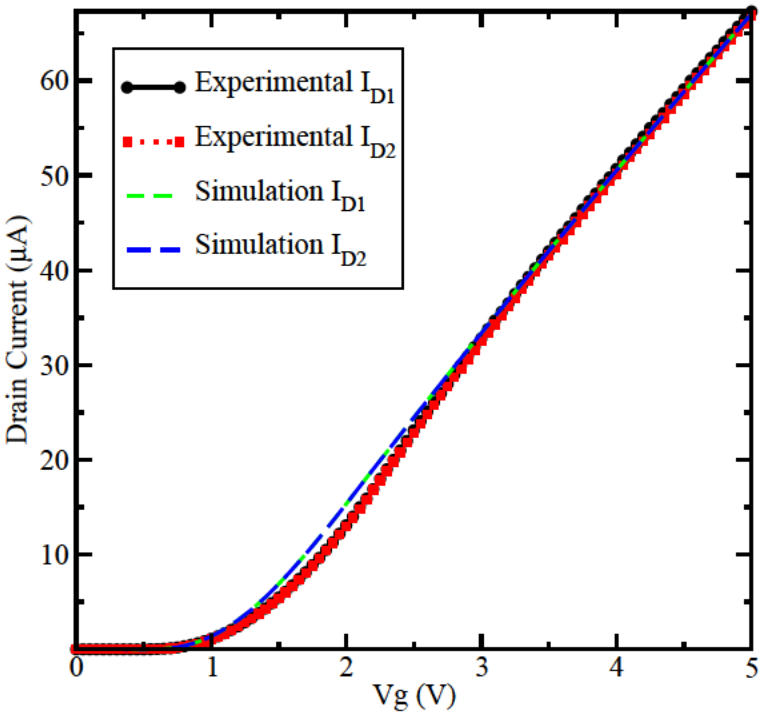

Figure 4.2: Drain currents as a function of the gate voltage at 300 K.

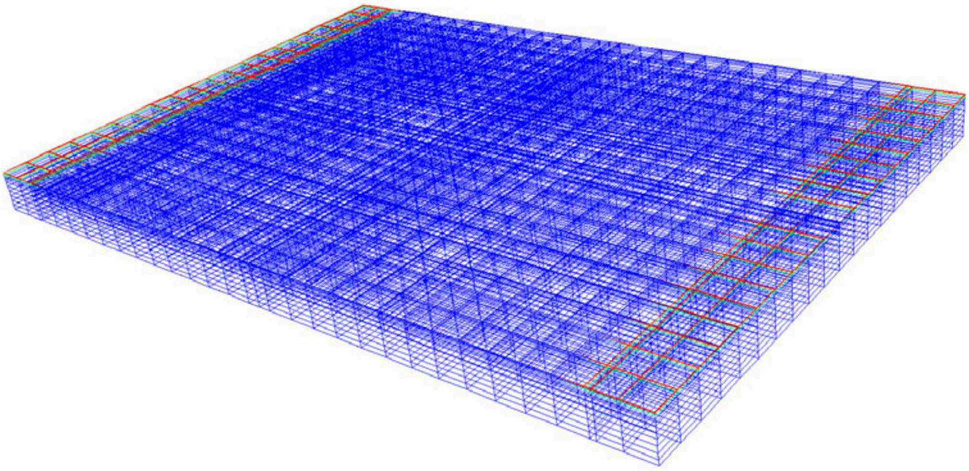

Figure 4.3: Three-dimensional view of the simulation grid.

4.2.1 Electrical Characteristics

Figure 4.2 shows the electrical characteristics of the two-drain MAGFET. Simulation results are compared with experimental data at room temperature. The bias are zero volts at source and substrate, and the drains are set to 1.0 V. A very good agreement between experimental and simulated data is obtained. The simulation grid used for this and the following results is shown in Figure 4.3. A cut is made at 90 μm from the source side along the width of the device. The current density is equally shared by both drains as it can be seen in Figure 4.4, where the x axis goes from the silicon oxide-silicon interface towards the substrate and the y axis is the width of the two-drain MAGFET.

4.2.2 Magnetic Field

If a magnetic field is applied perpendicular to the inversion layer, a differential current will be sensed according to (4.1). Figure 4.5 shows this differential current as a function of the magnetic field. In the present analysis the two-drain MAGFET is oriented in the following way (see Figure 4.3): the length of the device is along the x axis, the depth of the channel is along the y axis, and the width of the device is along the z axis. So, the magnetic field strength is set along the y axis.

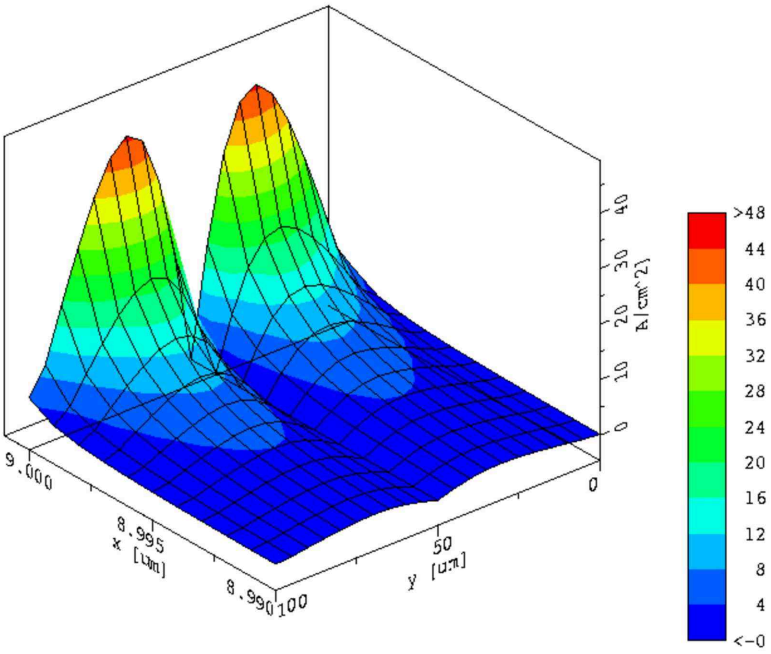

Figure 4.4: Current density at 300 K and zero magnetic field.

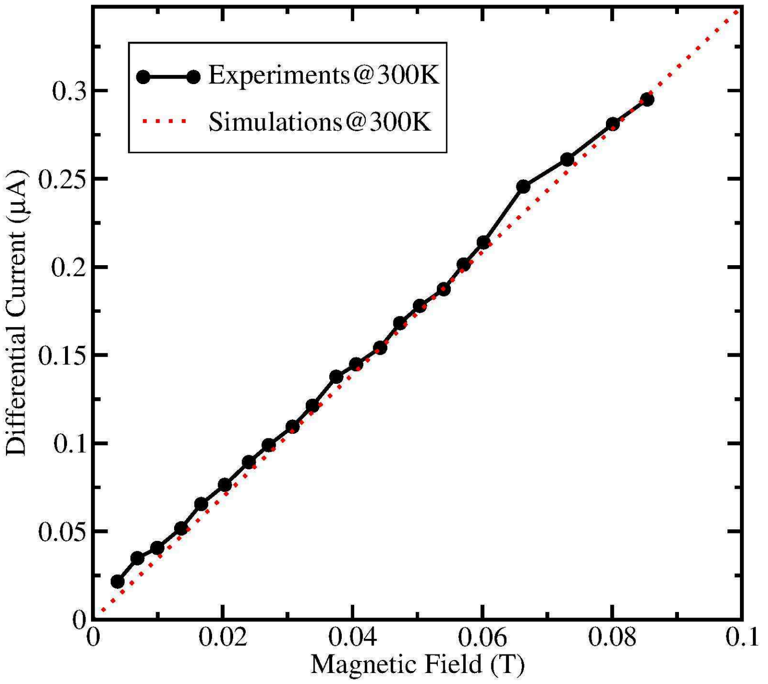

Figure 4.5: Differential current versus magnetic field at 300 K.

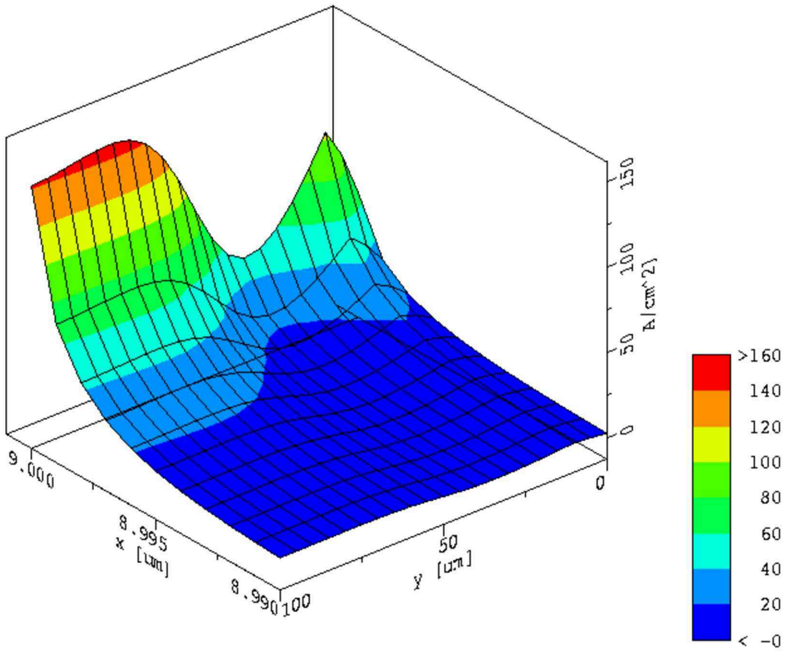

Figure 4.6: Current density at 300 K and a magnetic field of 50 mT.

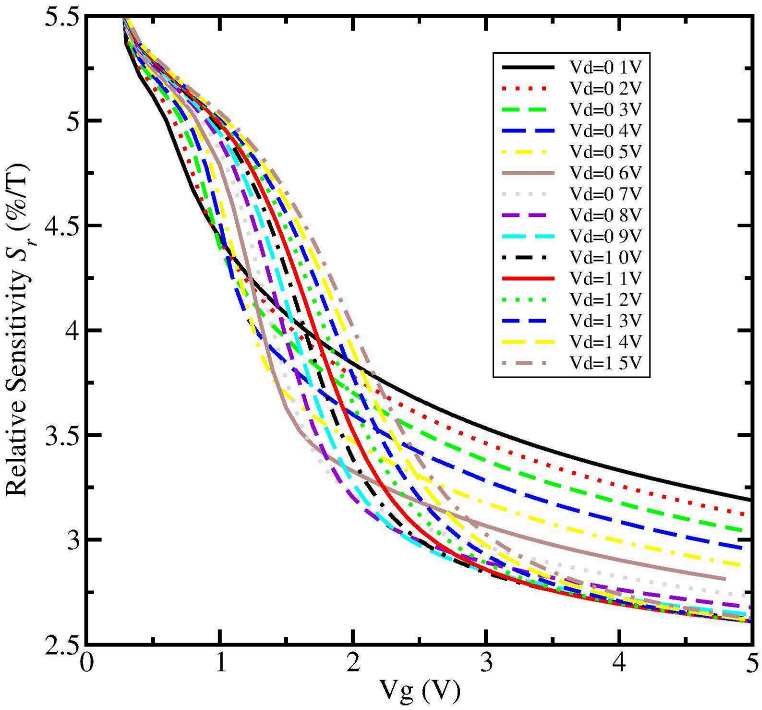

Figure 4.7: Simulated S_r as a function of the gate voltage at 300 K and 50 mT.

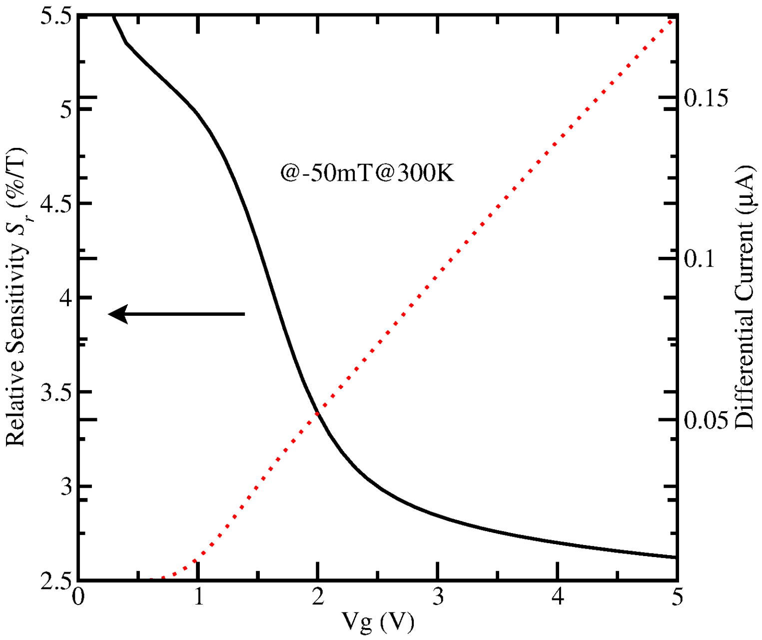

Figure 4.8: Simulated S_r and Δ for a gate swept. V_{D1} and V_{D2} are set to 1.0 V.

The match between experiments and simulation results is very good. The bias conditions of the two-drain MAGFET are a gate voltage of 4.95 V, a drain voltage of 1.0 V in both drains, and zero volts in the source and substrate. However, the Hall scattering factor for electrons is set to 0.6, a very low value in comparison to those that are found in the literature, specially in [6] and [18], where values between 1.1 and 1.4 are found.

A cut along the device is made again at 90 μm from the source side, as it was made with zero magnetic field. Figure 4.6 shows how the current piles up at one side of the two-drain MAGFET (x axis goes towards the substrate direction and y axis is the width of the two-drain MAGFET). It is clear that if the magnetic field is reversed, the current will pile up in the other drain.

At 300 K the relative sensitivity is 2.64 % T^{-1} according to (4.1). This is a very low value for a solid-state magnetic sensor, where Hall plates and other solid-state sensors are able to render up to 7 % T^{-1} at the same temperature [40]. However, most of the Hall sensors are compared with the current-related sensitivity, that is, the supply current that the Hall device needs to generate a higher Hall voltage. This current-related sensitivity is given in V/A-T units, so a direct comparison between Hall plates and the two-drain MAGFET is not possible, because the MAGFET sensor does not give a Hall voltage as output of the magnetic field sensing as the Hall plates do. The output of the magnetic field sensing in a two-drain MAGFET is the differential current between the drains. The higher this value, the higher the relative sensitivity. This differential current is related to the carrier deflection as it will be explained in the following section.

4.2.3 Bias Dependence

In this subsection the relative sensitivity as a function of the gate bias and the polarization of the drains is investigated. Figure 4.7 shows the relative sensitivity as a function of the gate voltage for different bias at the drains.

As the drain bias is increased the relative sensitivity decreases, because the thickness of the inversion layer is modulated, and also the longitudinal electric field increases, which reduces the carrier deflection. For example, at a gate voltage of 5.0 V the relative sensitivity decreases from 3.24 % T^{-1} down to 2.62 % T^{-1} showing that this modulation exists, but it is not as strong as with the gate voltage, where the relative sensitivity decreases from 5.50 % T^{-1} down to 2.62 % T^{-1}.

As the gate voltage is increased, the differential current increases too. Figure 4.8 shows how this differential current increases for a voltage of 1.0 V at the drains. However, that does not mean that the relative sensitivity increases. As can be seen from the same figure, the relative sensitivity decreases, because the differential current only increases a few microamperes whereas the total source current is larger at least two orders of magnitude.

The 's' shape of the relative sensitivity as a function of the gate voltage can be explained in terms of how carriers in the inversion layer move. For low drain to source voltages, most of the carriers move by diffusion. Once the drain to source voltage is high enough, the carriers are swept by the lateral electric field, that is, the carriers move by drift.

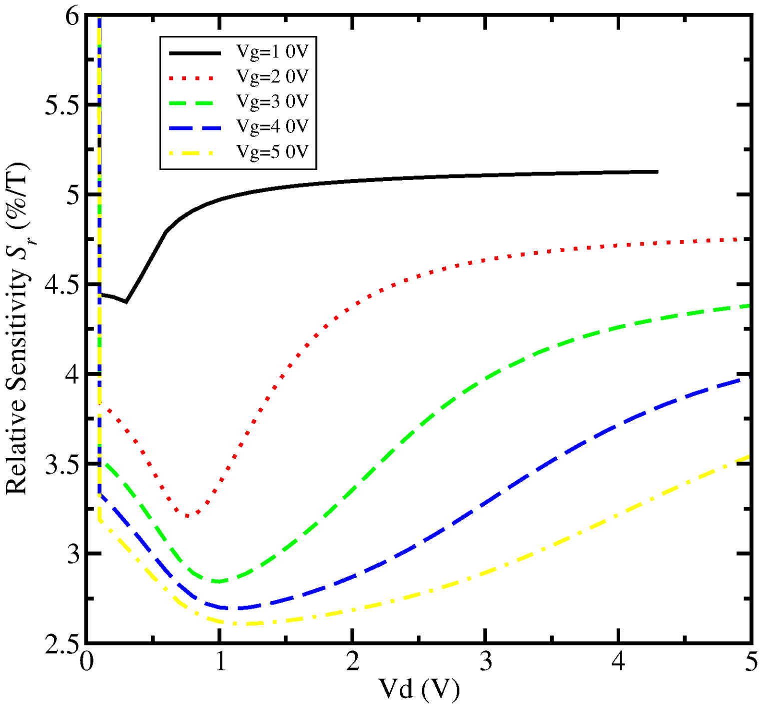

Figure 4.9: Simulated S_r as a function of the drain voltage at 300 K and 50 mT.

This behavior is more visible, if the relative sensitivity is plotted as a function of the drain voltage. Figure 4.9 shows this plot for different gate voltages. The minima of the relative sensitivity versus the drain voltage indicate the transition between diffusion and drift carrier transport, showing the complexity of the electro-magnetic interaction. In the low temperature analysis some surprising results are found for the same bias conditions, cf. Section 4.3.

Figure 4.9 also shows that the relative sensitivity is high at low gate voltages, because the drain currents are comparable with the differential current. Large differential currents can be reached at higher gate or drain voltages, but at expenses of larger drain currents. However, the relative sensibility decreases according to (4.1).

4.2.4 Channel Region

As the charge transport in the channel is governed by the same laws exactly as in a non split-drain MOSFET, it is desirable to observe how quantities change when a magnetic field is applied. Plots of the electron mobility, electron concentration, potential and electric field are shown. Because the variations are very small in the whole MAGFET structure, these quantities are presented from cuts along the MAGFET width and at 1 nm from the silicon oxide-silicon interface, that is, along the length of the MAGFET (see Fig. 4.1), from the end of the source towards the drains, cuts at 20 μm, 50 μm, 80 μm, and 110 μm from the source side are made. Then, the quantities are shown at 1 nm from the silicon oxide-silicon interface where deviations can be observed.

Figures 4.10 through 4.15 show the potential inside the channel at 20 μm from the source and at 1 nm from the silicon oxide-silicon interface at 300 K for different gate voltages and magnetic fields. Because the cut is close to the source which is biased to zero volts, the potential is almost constant when no magnetic field is applied. As soon as a magnetic field is applied, the potential is bent upwards if the magnetic field points inside the MAGFET sensor (y component of the magnetic field is 50 mT) or downwards on the contrary case (y component of the magnetic field is +50 mT). For a gate voltage of zero volts this bent is not noticeable, because the magnitude of the moving charge is very low, so the magnetic field has no visible effect on the potential.

From the previous plots, it is expected that the potential should be bent around a common point when a magnetic field is applied. Because the cut has been made at 20 μm from the source side of the MAGFET, the gate has more control over the channel than the other contacts. This explains the asymmetry in these figures. Figures 4.16 through 4.21 show the potential inside the channel at 50 μm from the source and at 1 nm from the silicon oxide-silicon interface at 300 K for different gate voltages and magnetic fields. The potential with zero magnetic field shows a small curvature coming from the drains, because the cut is approaching the drains. As can be seen, the potentials are symmetric with respect to the direction of the magnetic field.

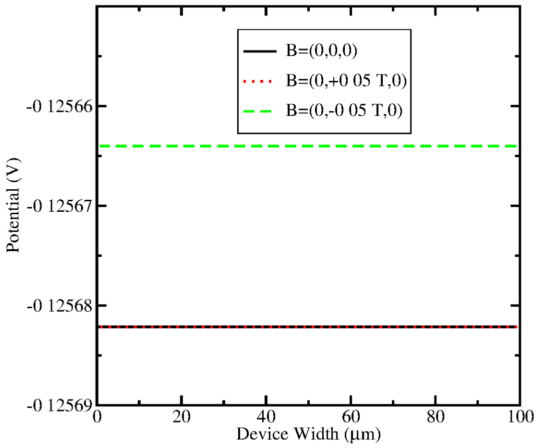

Figure 4.10: Potential in the channel @(20μm,300K,Vg=0.0V).

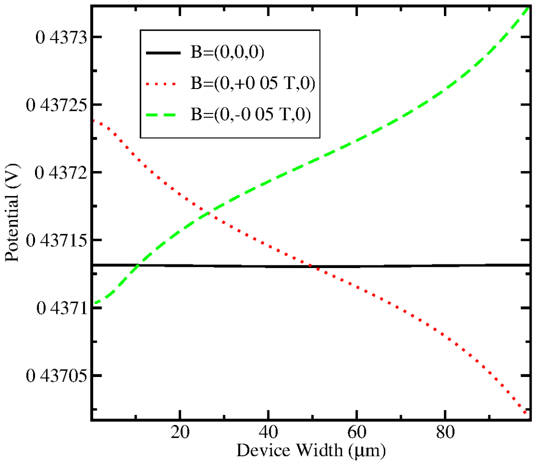

Figure 4.11: Potential in the channel @(20μm,300K,Vg=1.0V).

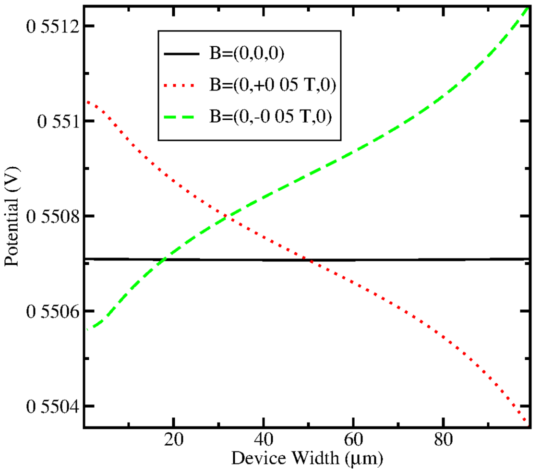

Figure 4.12: Potential in the channel @(20μm,300K,Vg=2.0V).

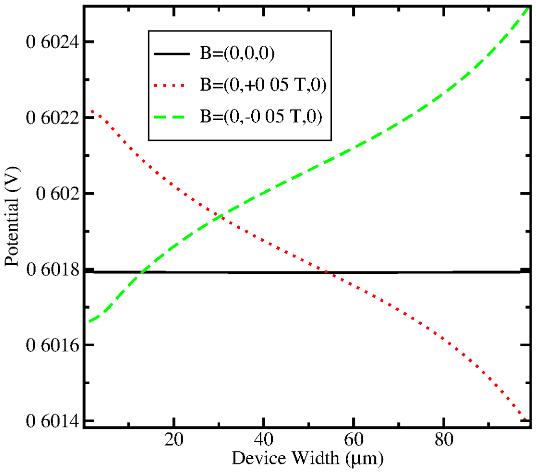

Figure 4.13: Potential in the channel @(20μm,300K,Vg=3.0V).

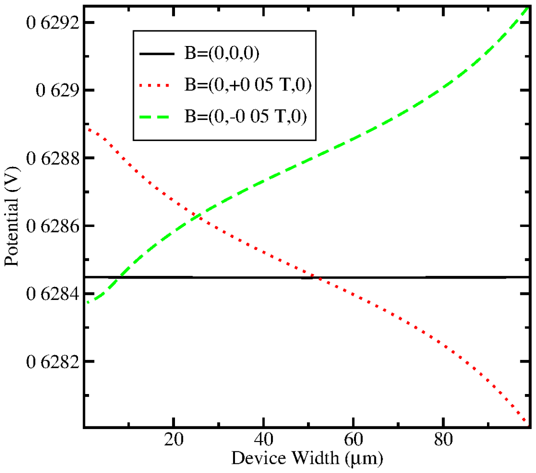

Figure 4.14: Potential in the channel @(20μm,300K,Vg=4.0V).

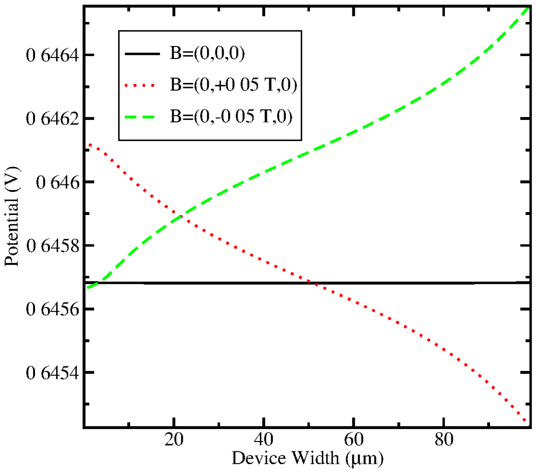

Figure 4.15: Potential in the channel @(20μm,300K,Vg=5.0V).

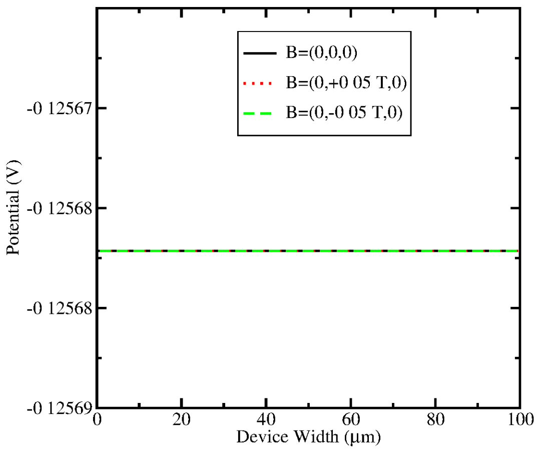

Figure 4.16: Potential in the channel @(50μm,300K,Vg=0.0V).

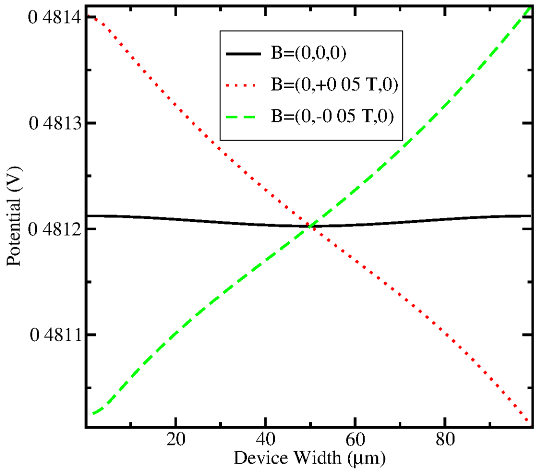

Figure 4.17: Potential in the channel @(50μm,300K,Vg=1.0V).

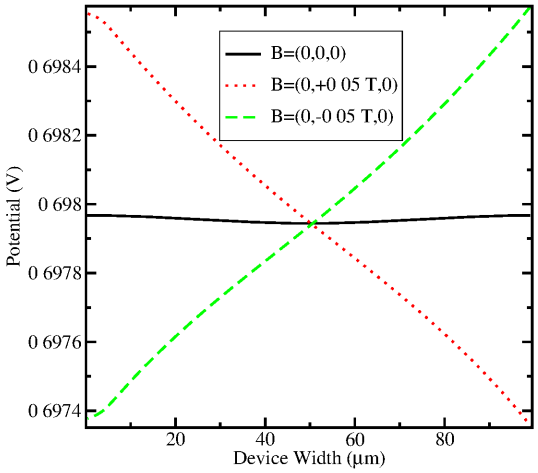

Figure 4.18: Potential in the channel @(50μm,300K,Vg=2.0V).

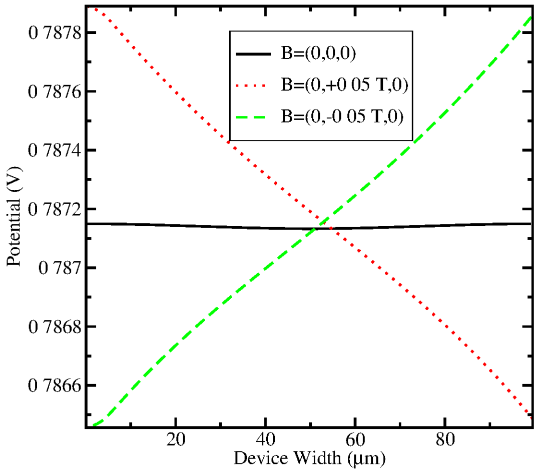

Figure 4.19: Potential in the channel @(50μm,300K,Vg=3.0V).

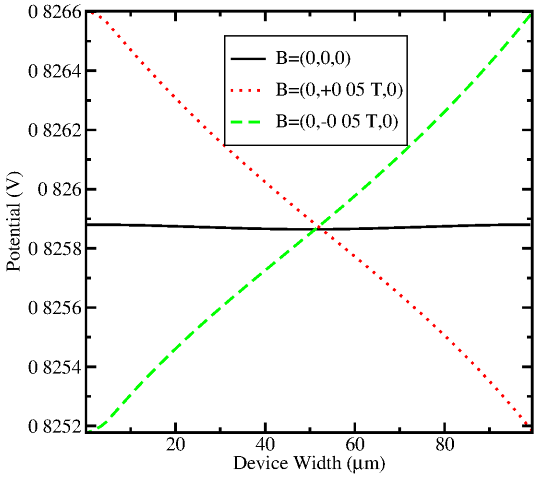

Figure 4.20: Potential in the channel @(50μm,300K,Vg=4.0V).

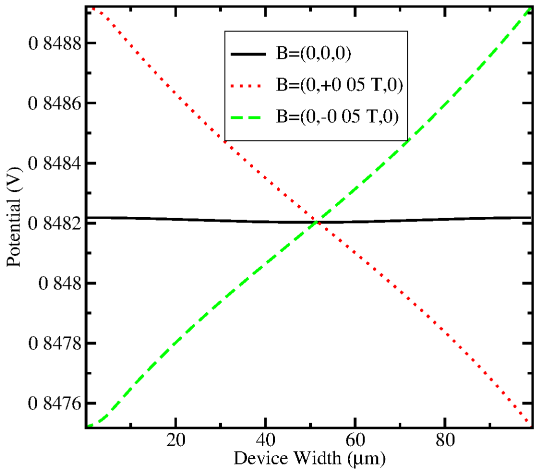

Figure 4.21: Potential in the channel @(50μm,300K,Vg=5.0V).

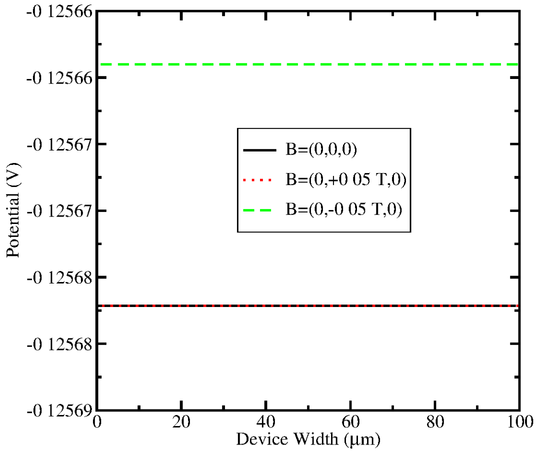

Figure 4.22: Potential in the channel @(80μm,300K,Vg=0.0V).

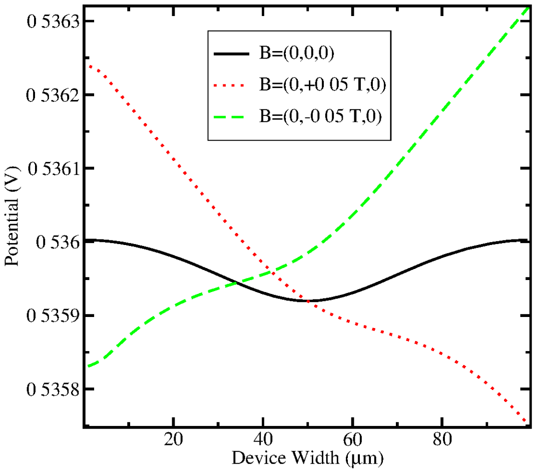

Figure 4.23: Potential in the channel @(80μm,300K,Vg=1.0V).

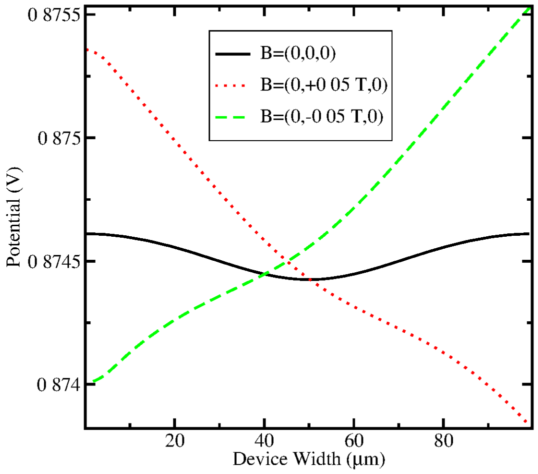

Figure 4.24: Potential in the channel @(80μm,300K,Vg=2.0V).

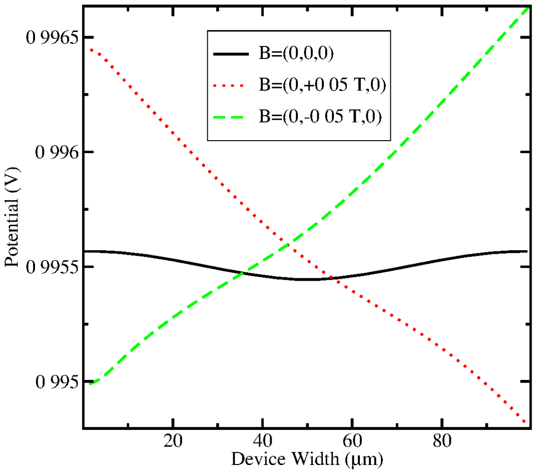

Figure 4.25: Potential in the channel @(80μm,300K,Vg=3.0V).

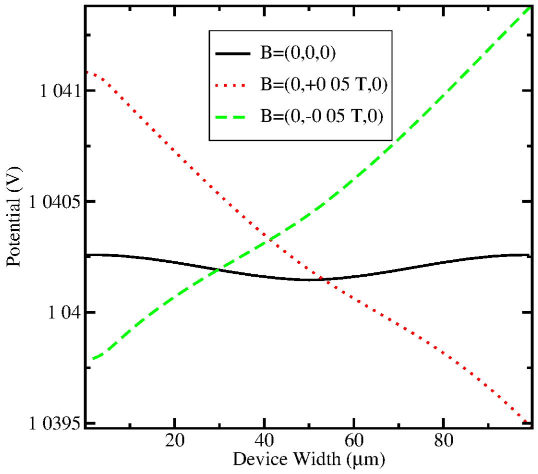

Figure 4.26: Potential in the channel @(80μm,300K,Vg=4.0V).

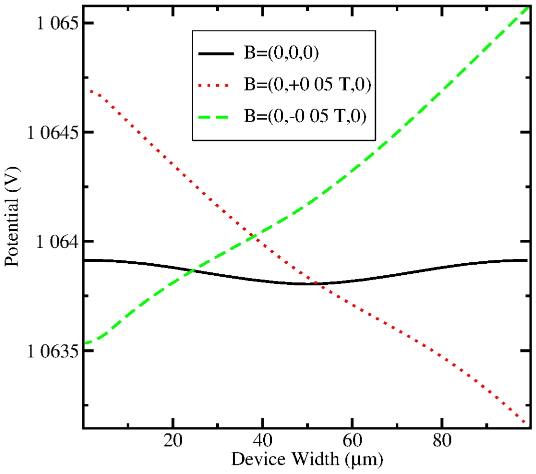

Figure 4.27: Potential in the channel @(80μm,300K,Vg=5.0V).

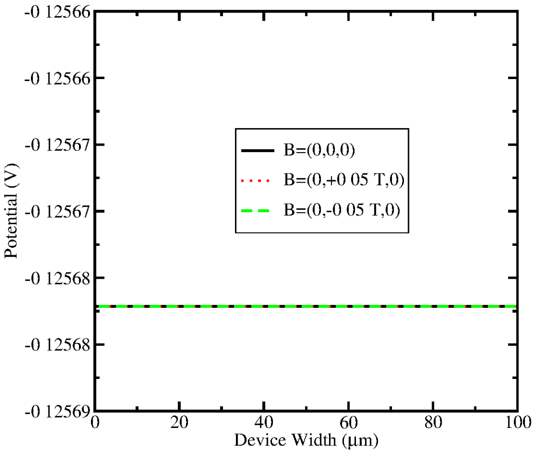

Figure 4.28: Potential in the channel @(110μm,300K,Vg=0.0V).

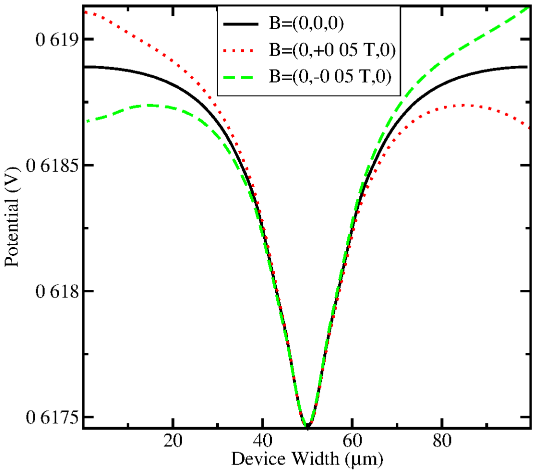

Figure 4.29: Potential in the channel @(110μm,300K,Vg=1.0V).

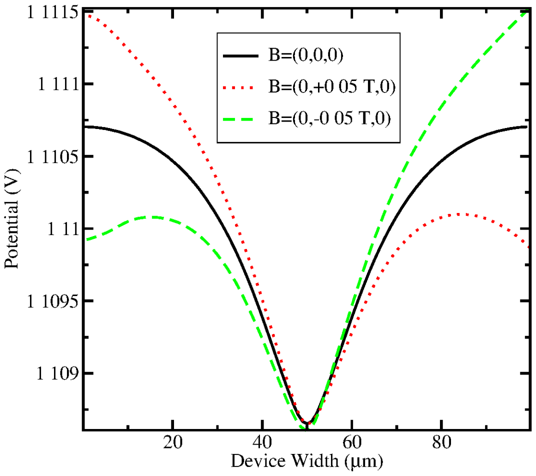

Figure 4.30: Potential in the channel @(110μm,300K,Vg=2.0V).

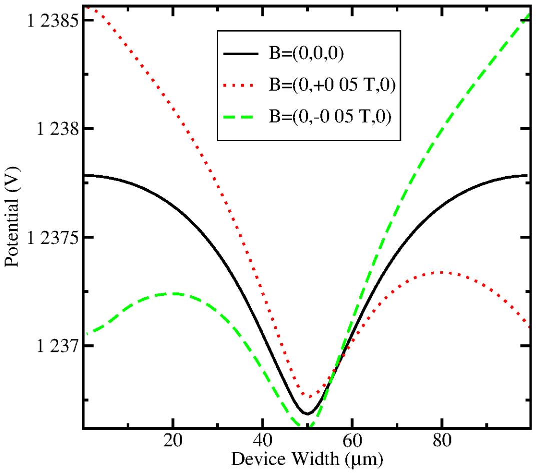

Figure 4.31: Potential in the channel @(110μm,300K,Vg=3.0V).

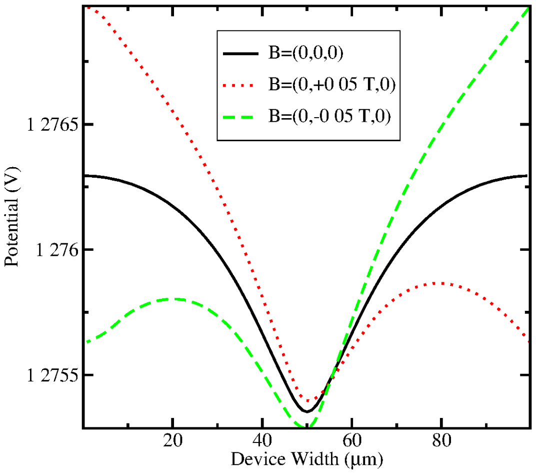

Figure 4.32: Potential in the channel @(110μm,300K,Vg=4.0V).

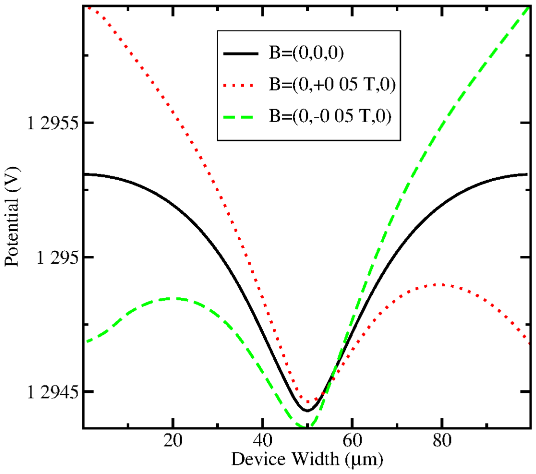

Figure 4.33: Potential in the channel @(110μm,300K,Vg=5.0V).

It is expected that a cut closer to the drains will show a strong influence of the drains on the potential. Figures 4.22 through 4.27 show the potential inside the channel at 80 μm from the source and at 1 nm from the silicon oxide-silicon interface at 300 K for different gate voltages and magnetic fields. A symmetry is roughly noticeable. Because the cut has been made in a zone between the middle of the MAGFET structure and the drains, in this zone both the gate and the drains *fight* for controlling this zone of the channel.

Figures 4.28 through 4.33 show the potential inside the channel at 110 μm from the source and at 1 nm from the silicon oxide-silicon interface at 300 K for different gate voltages and magnetic fields. The cut has been made only at 15 μm from the drains and their influence on the potential is quite remarkable. A quasi perfect symmetry can be seen in these figures.

The following quantity to be shown is the electron concentration inside the channel. As it is known from the Hall effect, the carriers pile up in one of the planes parallel to the applied magnetic field depending on their direction and the direction of the magnetic field. In the two-drain MAGFET, because the magnetic field is applied perpendicular to the channel, the electrons pile up in one side of the channel within the MAGFET structure. Figures 4.34 through 4.39 show the electron concentration inside the channel at 20 μm from the source and at 1 nm from the silicon oxide-silicon interface at 300K for different gate voltages and magnetic fields. For the gate voltages from 0 V, 1 V, and 2 V, a symmetry in the electron concentration due to the magnetic fields can be seen. For gate voltages larger than 3 V, the electron concentration with zero magnetic field is lower than the corresponding electron concentration with a magnetic field. This effect can be explained in terms of the driving force that exerts the gate. Because the electrons are attracted to the silicon oxide-silicon interface and at the same time swept by the Hall electric field, their concentration is higher in one side than in the other. Then, a symmetry point cannot be seen.

Figures 4.40 through 4.45 show the electron concentration inside the channel at 50 μm from the source and at 1 nm from the silicon oxide-silicon interface at 300 K for different gate voltages and magnetic fields. As stated for the potential, the cuts are approaching the drains, so a stronger influence from the drains on the electron concentration can be seen. A maximum is observed in the middle of the channel (with respect to the width of the MAGFET) for zero magnetic field, and it is caused by the combination of the lateral electric field which concentrates on the drains and the stronger transversal electric field. The scale at which the electron concentrations are plotted should be noticed. Because the applied magnetic field is quite low (50 mT), the changes with respect to the zero magnetic field case are very small. Stronger variations in the electric field and carrier concentration can be seen for stronger magnetic inductions or for devices with higher carrier mobilities [5, 24].

Figures 4.46 through 4.51 show the electron concentration inside the channel at 80 μm from the source and at 1 nm from the silicon oxide-silicon interface at 300 K for different gate voltages and magnetic fields. Comparing these figures with Figures 4.34 through

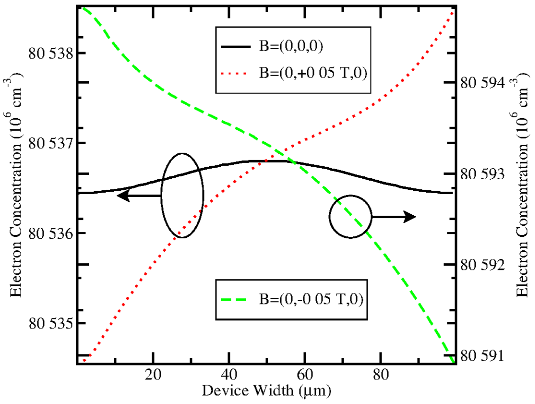

Figure 4.34: Electron concentration in the channel @(20μm,300K,Vg=0.0V).

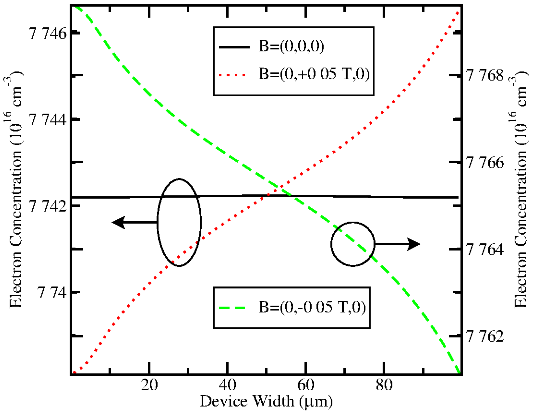

Figure 4.35: Electron concentration in the channel @(20μm,300K,Vg=1.0V).

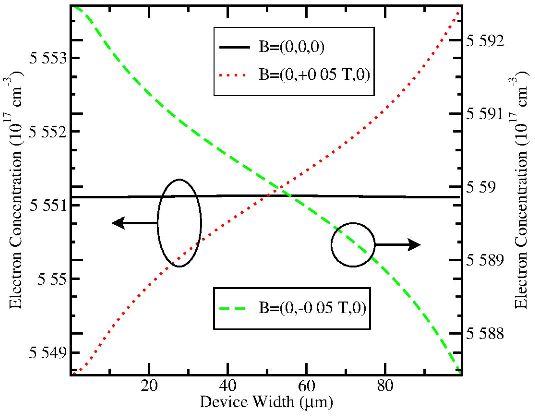

Figure 4.36: Electron concentration in the channel @(20μm,300K,Vg=2.0V).

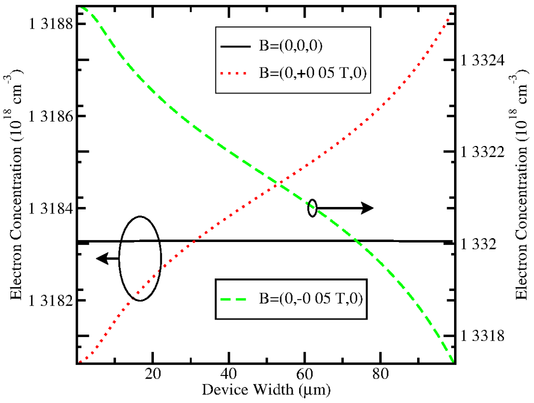

Figure 4.37: Electron concentration in the channel @(20μm,300K,Vg=3.0V).

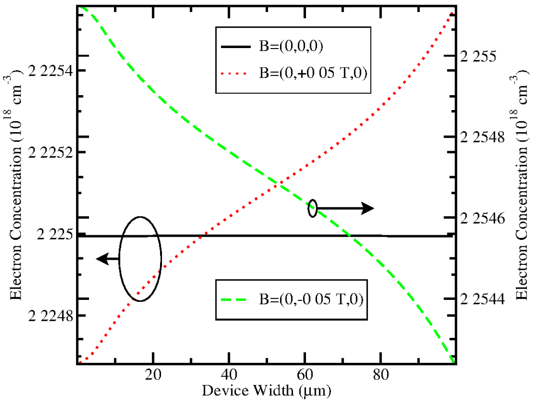

Figure 4.38: Electron concentration in the channel @(20μm,300K,Vg=4.0V).

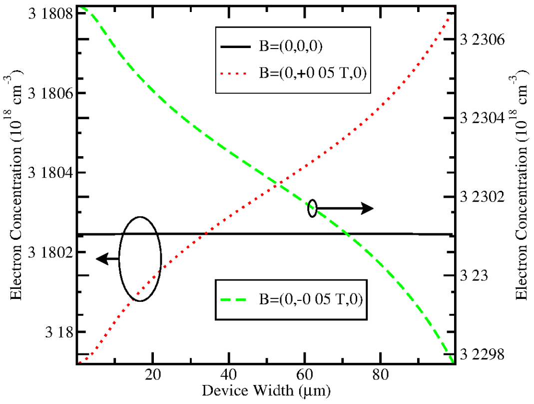

Figure 4.39: Electron concentration in the channel @(20μm,300K,Vg=5.0V).

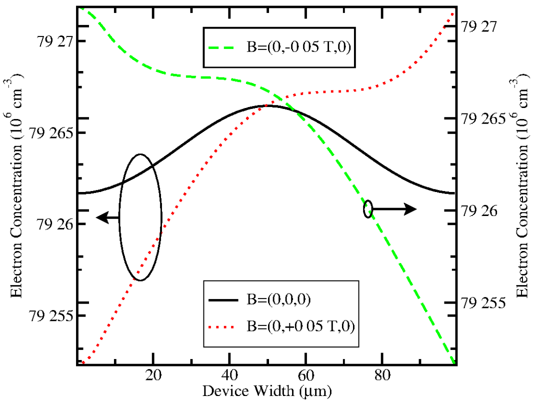

Figure 4.40: Electron concentration in the channel @(50μm,300K,Vg=0.0V).

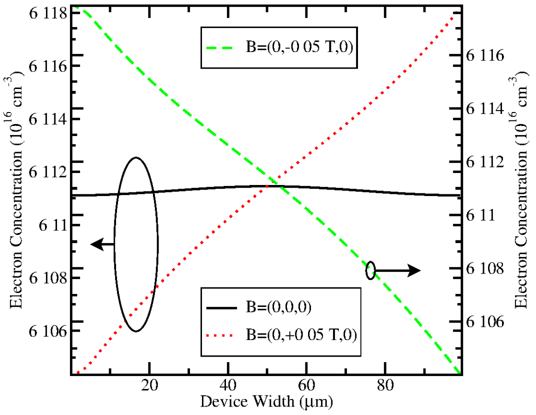

Figure 4.41: Electron concentration in the channel @(50μm,300K,Vg=1.0V).

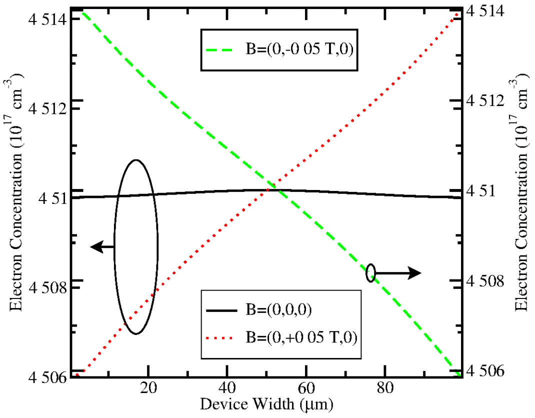

Figure 4.42: Electron concentration in the channel @(50μm,300K,Vg=2.0V).

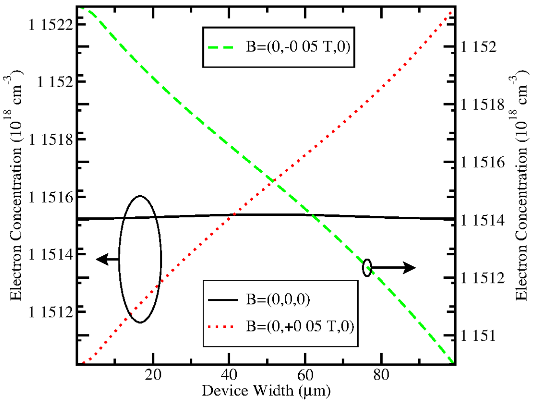

Figure 4.43: Electron concentration in the channel @(50μm,300K,Vg=3.0V).

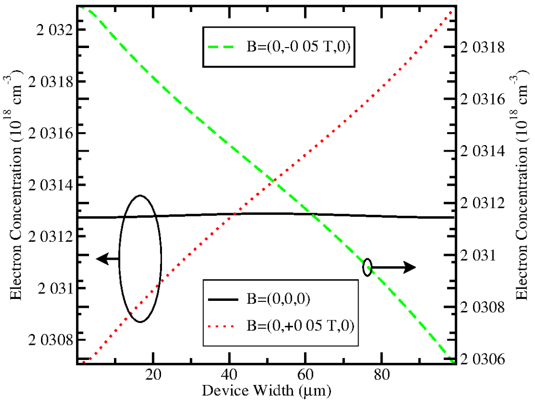

Figure 4.44: Electron concentration in the channel @(50μm,300K,Vg=4.0V).

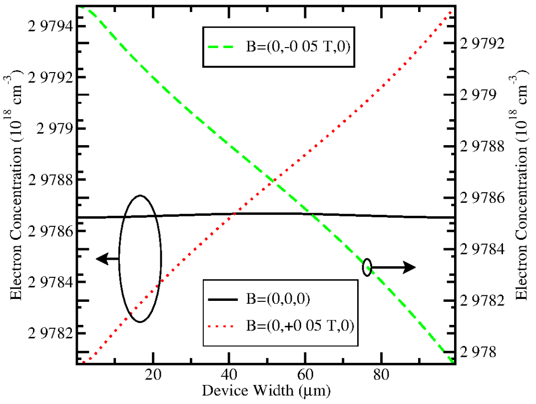

Figure 4.45: Electron concentration in the channel @(50μm,300K,Vg=5.0V).

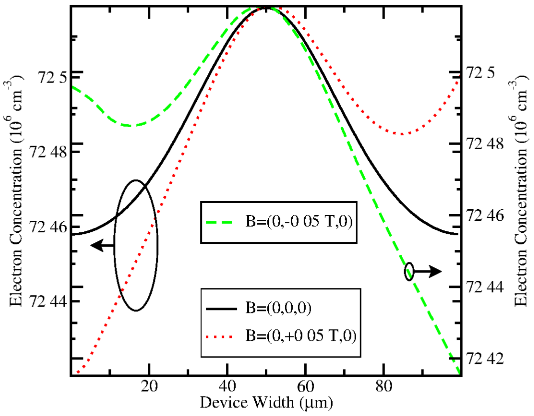

Figure 4.46: Electron concentration in the channel @(80μm,300K,Vg=0.0V).

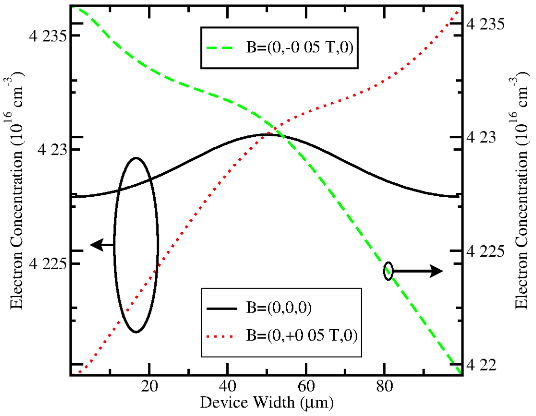

Figure 4.47: Electron concentration in the channel @(80μm,300K,Vg=1.0V).

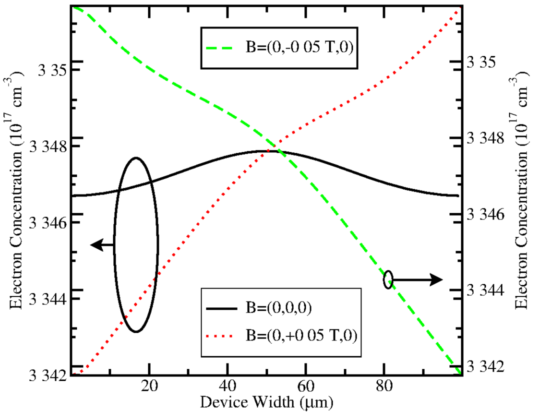

Figure 4.48: Electron concentration in the channel @(80μm,300K,Vg=2.0V).

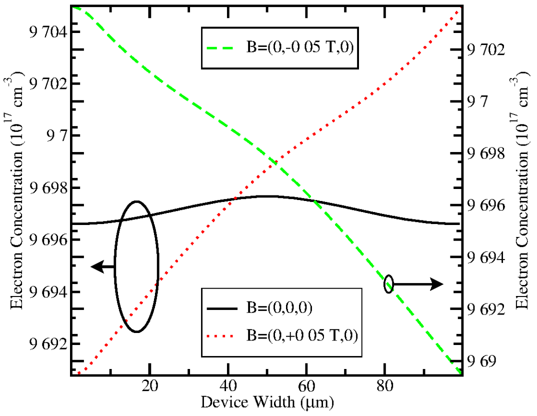

Figure 4.49: Electron concentration in the channel @(80μm,300K,Vg=3.0V).

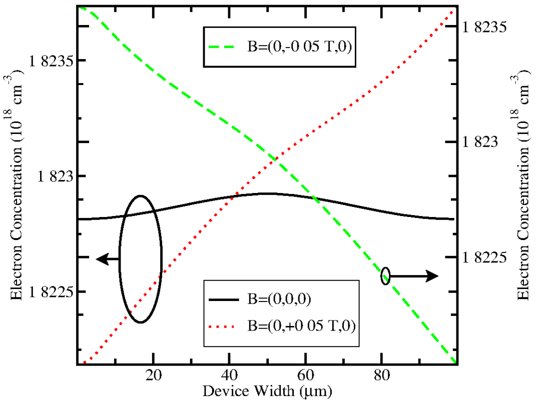

Figure 4.50: Electron concentration in the channel @(80μm,300K,Vg=4.0V).

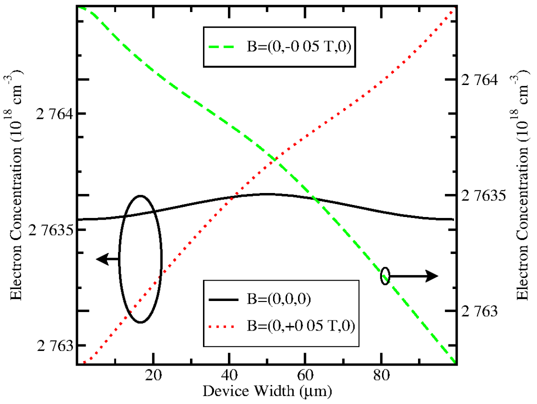

Figure 4.51: Electron concentration in the channel @(80μm,300K,Vg=5.0V).

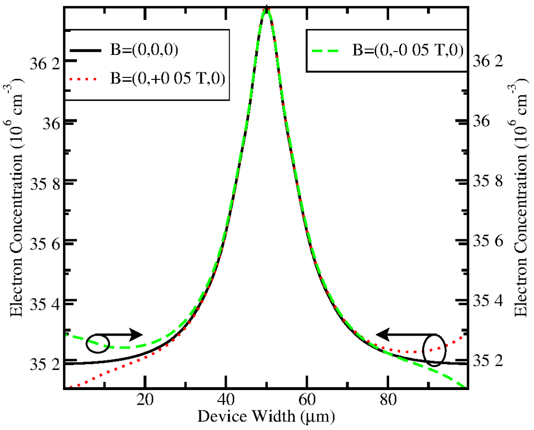

Figure 4.52: Electron concentration in the channel @(110μm,300K,Vg=0.0V).

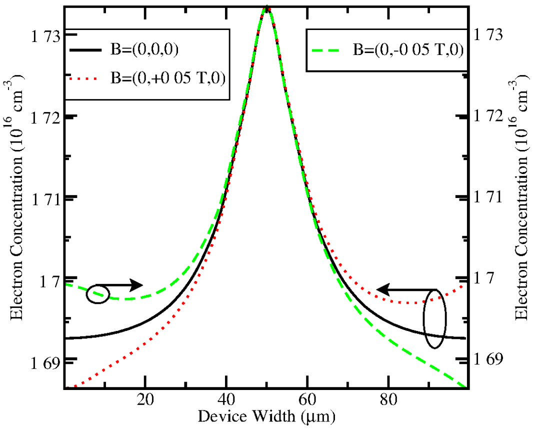

Figure 4.53: Electron concentration in the channel @(110μm,300K,Vg=1.0V).

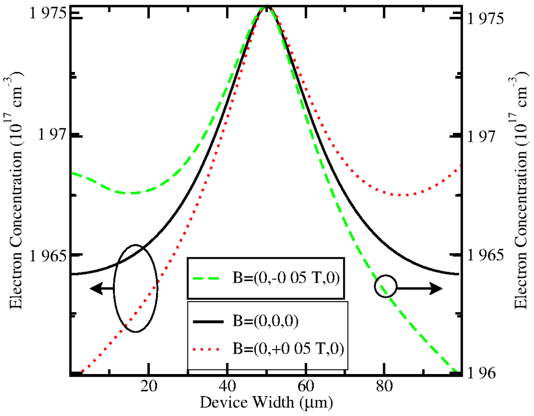

Figure 4.54: Electron concentration in the channel @(110μm,300K,Vg=2.0V).

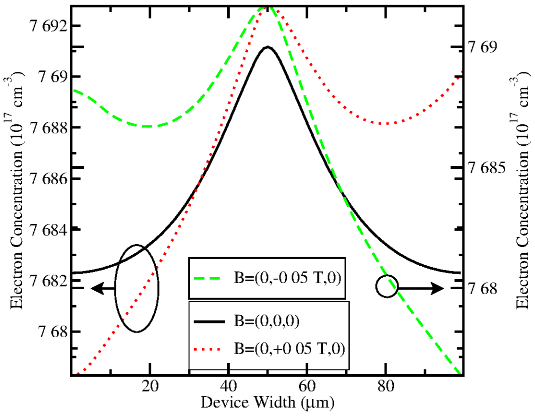

Figure 4.55: Electron concentration in the channel @(110μm,300K,Vg=3.0V).

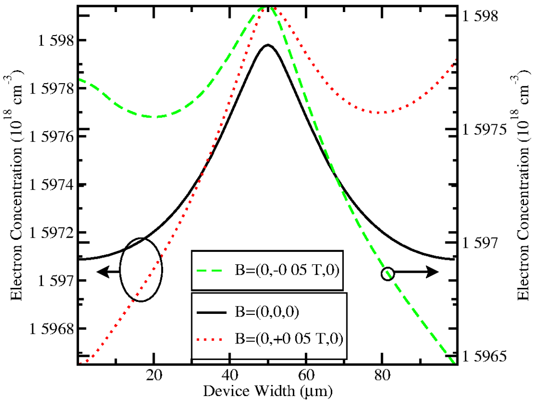

Figure 4.56: Electron concentration in the channel @(110μm,300K,Vg=4.0V).

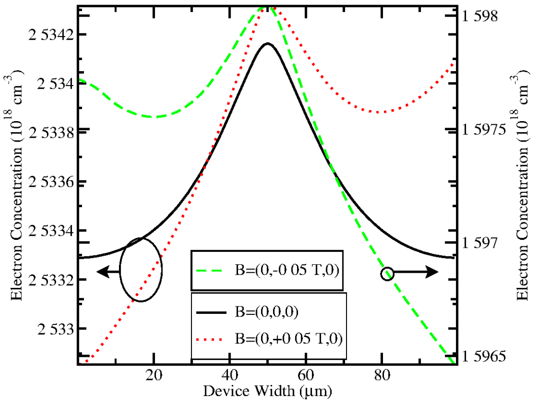

Figure 4.57: Electron concentration in the channel @(110μm,300K,Vg=5.0V).

4.39, the electron concentration for zero magnetic field shows a maximum. Actually there is indeed a maximum but it is hardly noticeable due to the scale used for the plots and because the cut is localized far away from the drains. In Figures 4.52 through 4.57 the electron concentration inside the channel at 110 μm from the source and at 1 nm from the silicon oxide-silicon interface at 300 K for different gate voltages and magnetic fields is shown. The strong influence from the drains and the gate can be seen on the electron concentration. In addition, a perfect symmetry can be observed.

The electric field is also a quantity of interest. Actually, its shape is correlated to the carrier concentration and the potential. However, the electric field is a vectorial quantity and because this subsection is presenting two-dimensional cuts from full three-dimensional simulations of a two-drain MAGFET, one component is missing. The cuts are made perpendicular to the y-z plane (see Figure 4.1) so the lateral component of the electric field due to the drains to source bias is missing (x component). The following plots only show the absolute value of the y and z components at 1 nm of the silicon oxide-silicon interface.

Figures 4.58 through 4.63 show the electric field inside the channel at 20 μm from the source and at 1 nm from the silicon oxide-silicon interface at 300 K for different gate voltages and magnetic fields. As explained for the electron concentration plots at the same cut distance, a symmetry in the electric field line can be observed for low gate voltages but this symmetry is lost as soon as the gate voltage is larger than 3 V. Because the cut is close to the source which is set to zero volts, the dominant component of the electric field is due to the gate. Although the x component of the electric field is missing in these figures, its influence can be noticed for the following figures as the cut approaches the drains.

Figures 4.64 through 4.69 show the electric field inside the channel at 50 μm from the source and at 1 nm from the silicon oxide-silicon interface at 300 K for different gate voltages and magnetic fields whereas Figures 4.70 through 4.75 show the electric field inside the channel at 80 μm from the source and at 1 nm from the silicon oxide-silicon interface at 300 K for different gate voltages and magnetic fields. Because a magnetic field deflects the electron current lines inside the channel, a Hall electric field across the current path must counteract the deflection.

As soon as the electrons leave the source, the magnetic field acts on them but not instantaneously. After the electrons have run through some of their paths, they are turned, so it is expected that the Hall electric field is not uniform. The electric field line in Figures 4.58 through 4.75 show this Hall electric field (when a magnetic field is applied). If the device were a MOS Hall plate, this line should be a straight line. That is the reason why the Hall contacts in a MOS Hall plate should be placed close but not next to the drain.

Figures 4.76 through 4.81 show the electric field inside the channel at 110 μm from the source and at 1 nm from the silicon oxide-silicon interface at 300 K for different gate voltages and magnetic fields. The influence of the drains is evident in this zone of the channel.

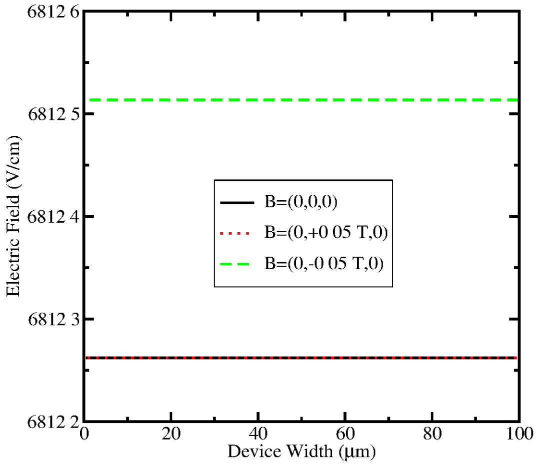

Figure 4.58: Electric field in the channel @(20μm,300K,Vg=0.0V).

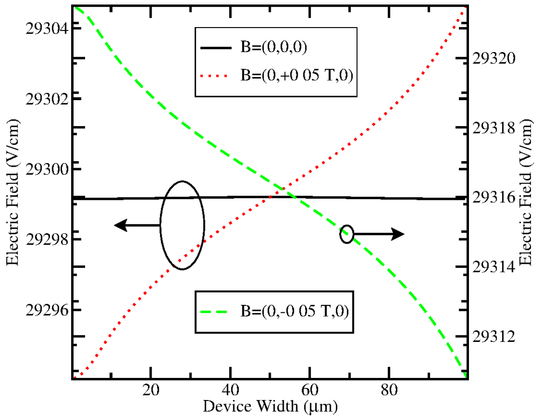

Figure 4.59: Electric field in the channel @(20μm,300K,Vg=1.0V).

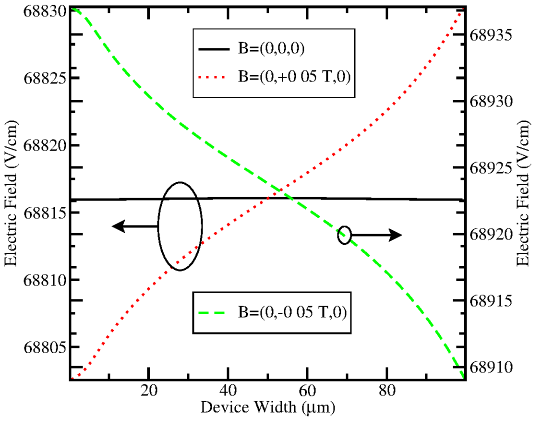

Figure 4.60: Electric field in the channel @(20μm,300K,Vg=2.0V).

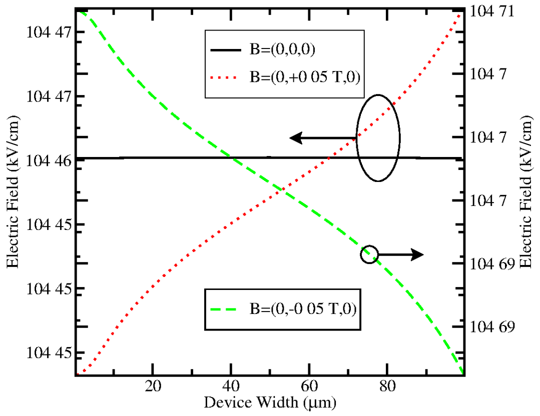

Figure 4.61: Electric field in the channel @(20μm,300K,Vg=3.0V).

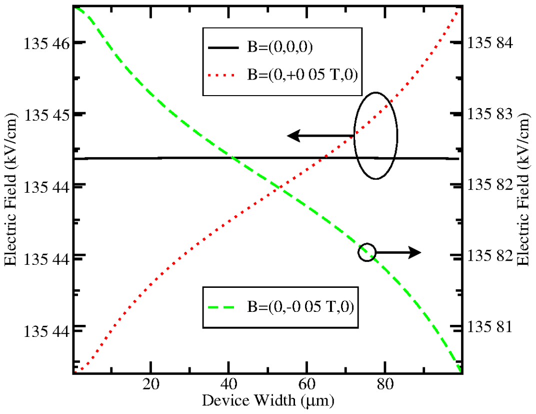

Figure 4.62: Electric field in the channel @(20μm,300K,Vg=4.0V).

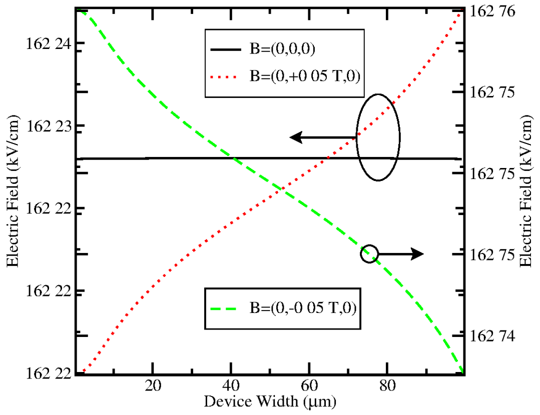

Figure 4.63: Electric field in the channel @(20μm,300K,Vg=5.0V).

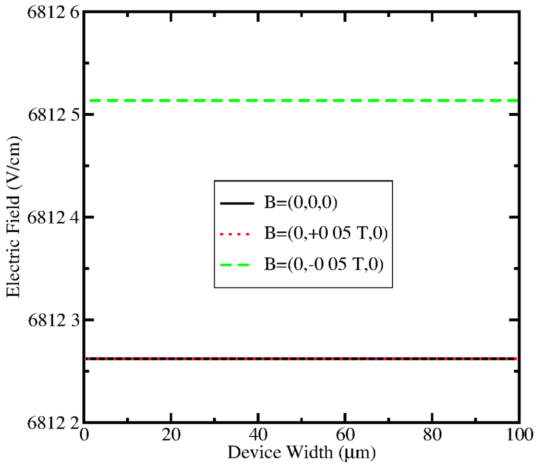

Figure 4.64: Electric field in the channel @(50μm,300K,Vg=0.0V).

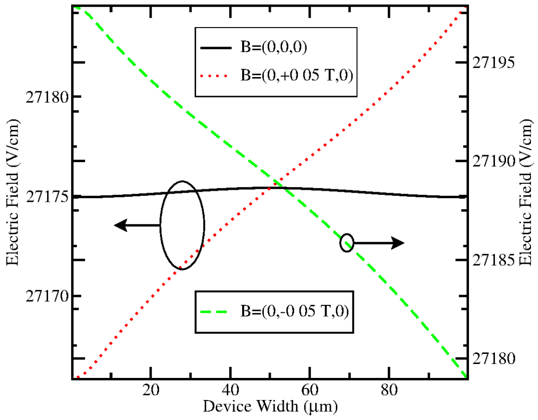

Figure 4.65: Electric field in the channel @(50μm,300K,Vg=1.0V).

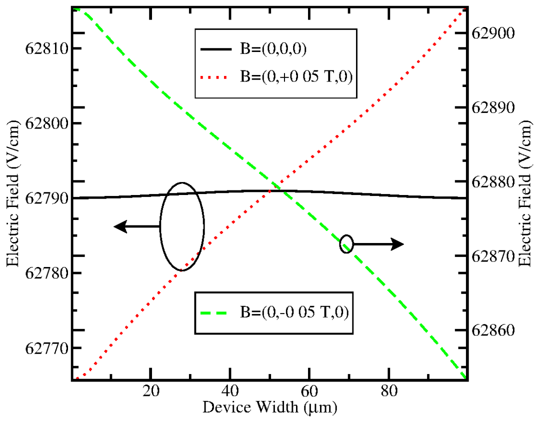

Figure 4.66: Electric field in the channel @(50μm,300K,Vg=2.0V).

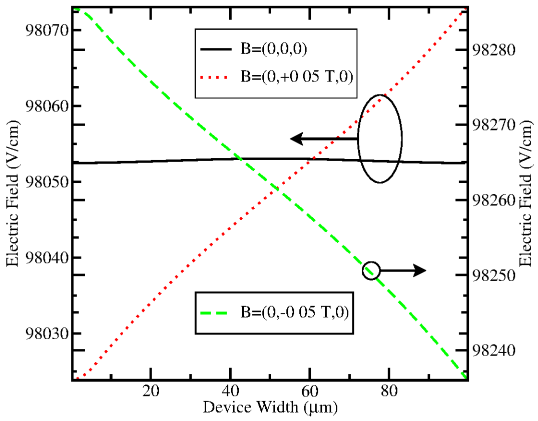

Figure 4.67: Electric field in the channel @(50μm,300K,Vg=3.0V).

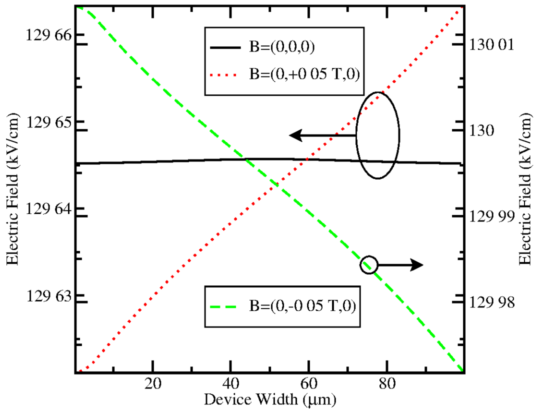

Figure 4.68: Electric field in the channel @(50μm,300K,Vg=4.0V).

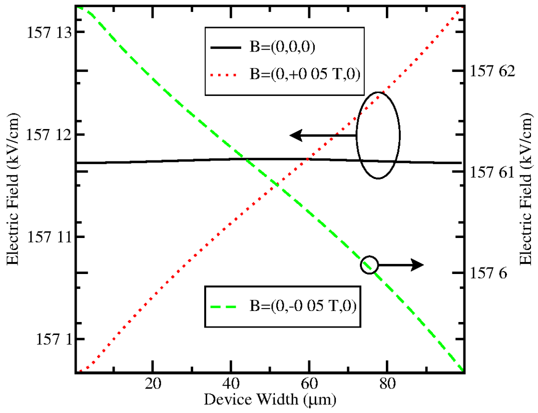

Figure 4.69: Electric field in the channel @(50μm,300K,Vg=5.0V).

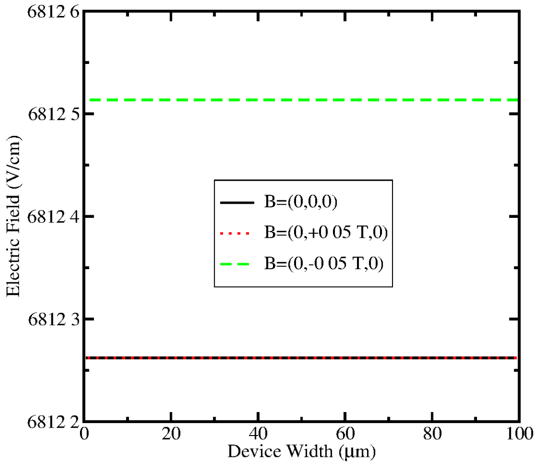

Figure 4.70: Electric field in the channel @(80μm,300K,Vg=0.0V).

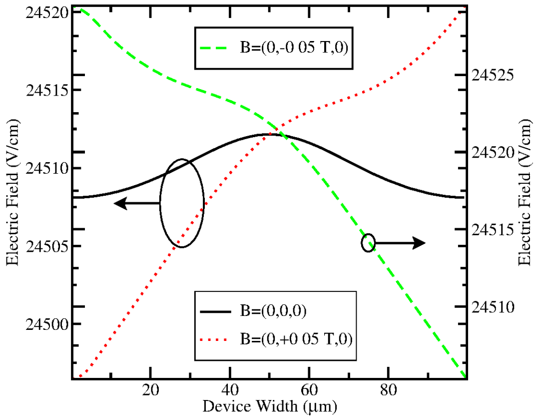

Figure 4.71: Electric field in the channel @(80μm,300K,Vg=1.0V).

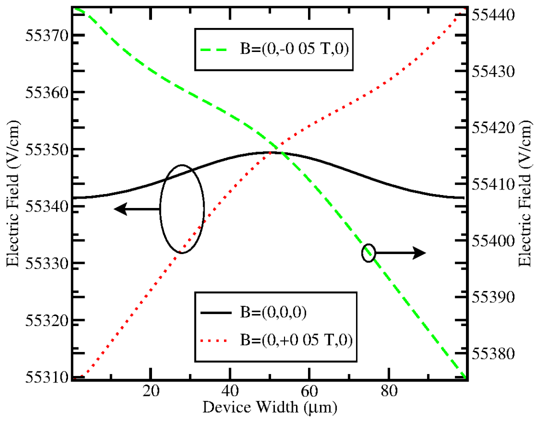

Figure 4.72: Electric field in the channel @(80μm,300K,Vg=2.0V).

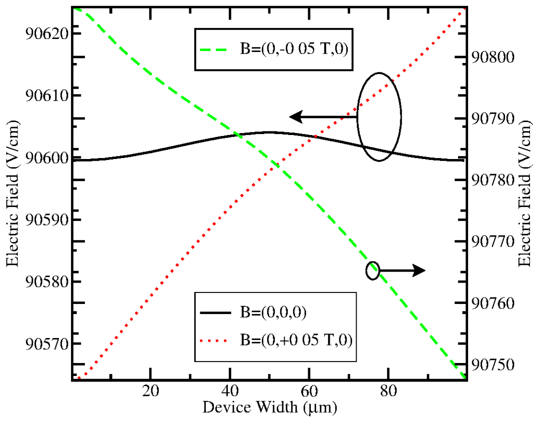

Figure 4.73: Electric field in the channel @(80μm,300K,Vg=3.0V).

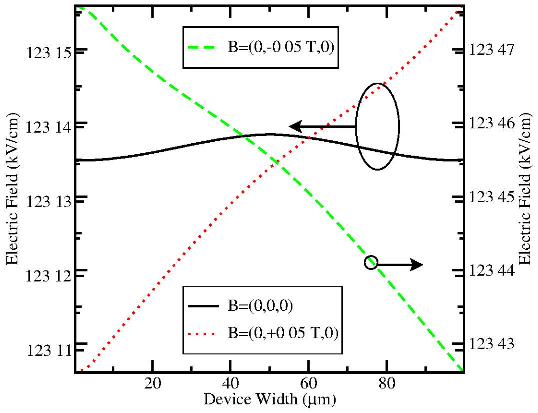

Figure 4.74: Electric field in the channel @(80μm,300K,Vg=4.0V).

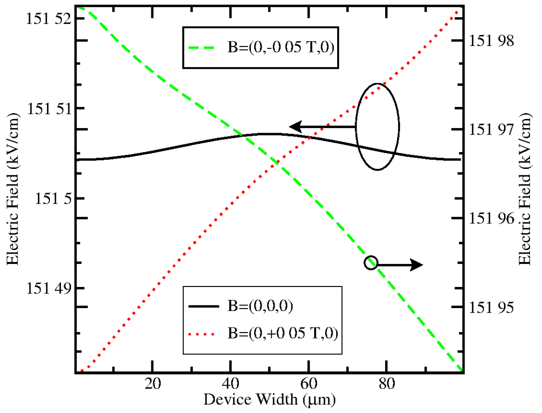

Figure 4.75: Electric field in the channel @(80μm,300K,Vg=5.0V).

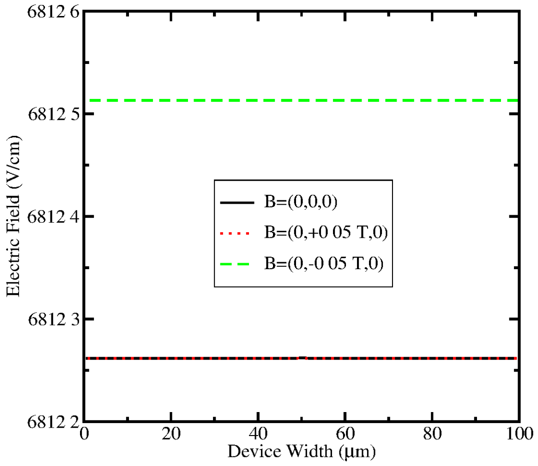

Figure 4.76: Electric field in the channel @(110μm,300K,Vg=0.0V).

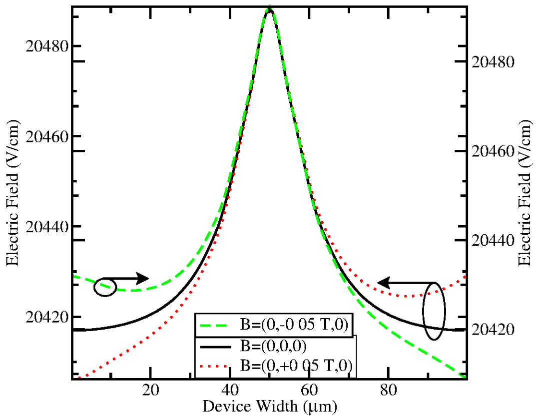

Figure 4.77: Electric field in the channel @(110μm,300K,Vg=1.0V).

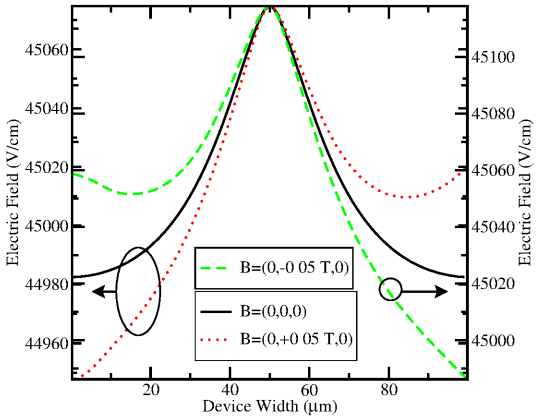

Figure 4.78: Electric field in the channel @(110μm,300K,Vg=2.0V).

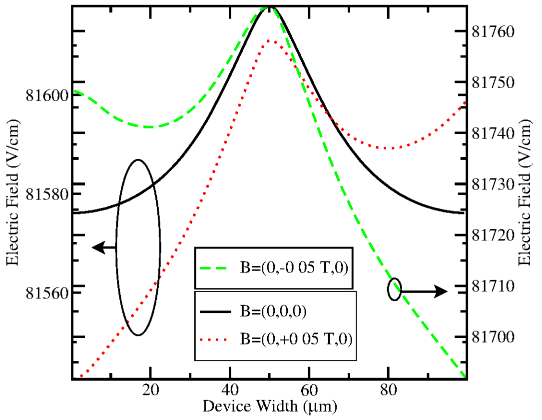

Figure 4.79: Electric field in the channel @(110μm,300K,Vg=3.0V).

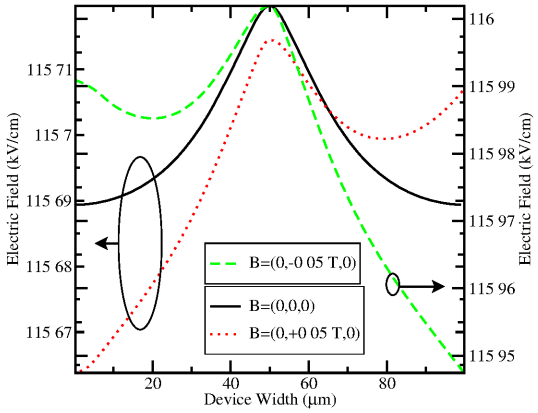

Figure 4.80: Electric field in the channel @(110μm,300K,Vg=4.0V).

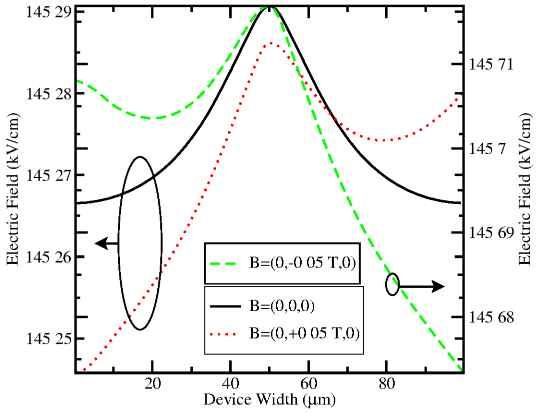

Figure 4.81: Electric field in the channel @(110μm,300K,Vg=5.0V).

4.3 Analysis at 77 K

The carrier deflection inside the inversion layer can be defined as follows:

$$L\mu_n|\mathbf{B}| \tag{4.2}$$

where L is the length of the device, μ_n is the electron mobility in the inversion layer, and $|\mathbf{B}|$ is the strength of the magnetic field. It is obvious that the larger the magnetic field, the larger the deflection of the current lines inside the channel. If a larger deflection is desirable at low magnetic field strengths, increasing the electron mobility of the inversion layer is one available solution. By cooling the two-drain MAGFET to 77 K (liquid Nitrogen temperature), the electron mobility increases. As a result, larger deflections are obtained with smaller magnetic field strengths [16] and the differential current will be higher.

4.3.1 Electrical Characteristics

Figure 4.82 shows the electrical characteristics of the two-drain MAGFET at 77 K. The source and substrate are biased at zero volts, while the drains are biased at 1.0 V. Only one drain current is shown because the experimental data shows that both currents are exactly the same, as in the simulation results. Compared to room temperature simulations, at 77 K the fitting between experimental data and simulation is not so good, but it suffices to qualitatively explain the results.

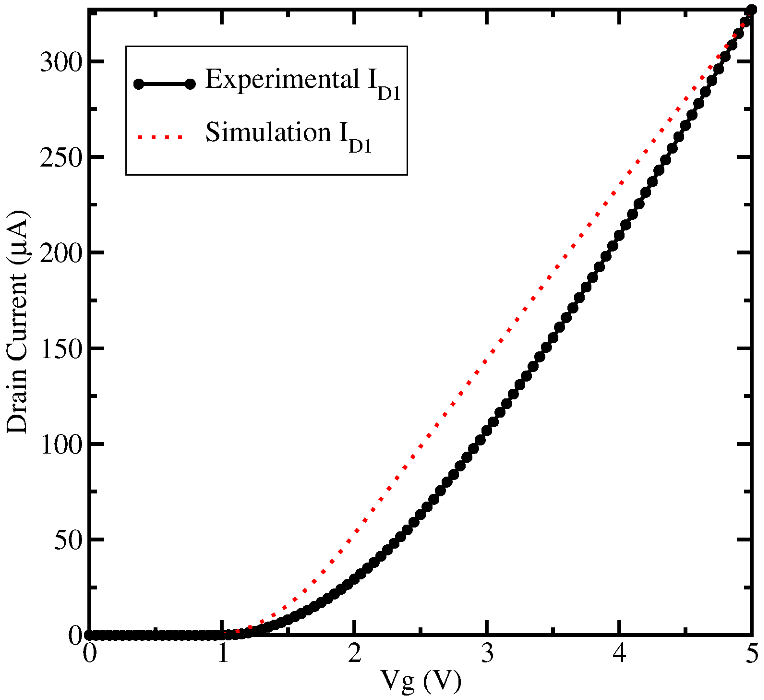

Figure 4.82: Drain currents as a function of the gate voltage at 77 K.

4.3.2 Magnetic Field

Figure 4.83 shows the differential current as a function of the magnetic field at 77 K and 300 K. The simulation results perfectly match the experimental data at 77 K. In this case the Hall scattering factor for electrons has been set to 0.8. From the data in Figure 3.1 [18], the Hall scattering factor increases as the temperature decreases. Although the absolute values of the Hall scattering factors for electrons used in the simulations do not agree with the values found in [18], the increase of the Hall scattering factor for electrons from 0.6 at 300 K to 0.8 at 77 K in this thesis seems to be reasonable in view of the match of the simulation results with the experimental data. The bias of the two-drain MAGFET are a gate voltage of 4.95 V, a drain voltage of 1.0 V in both drains, and zero volts in the source and substrate.

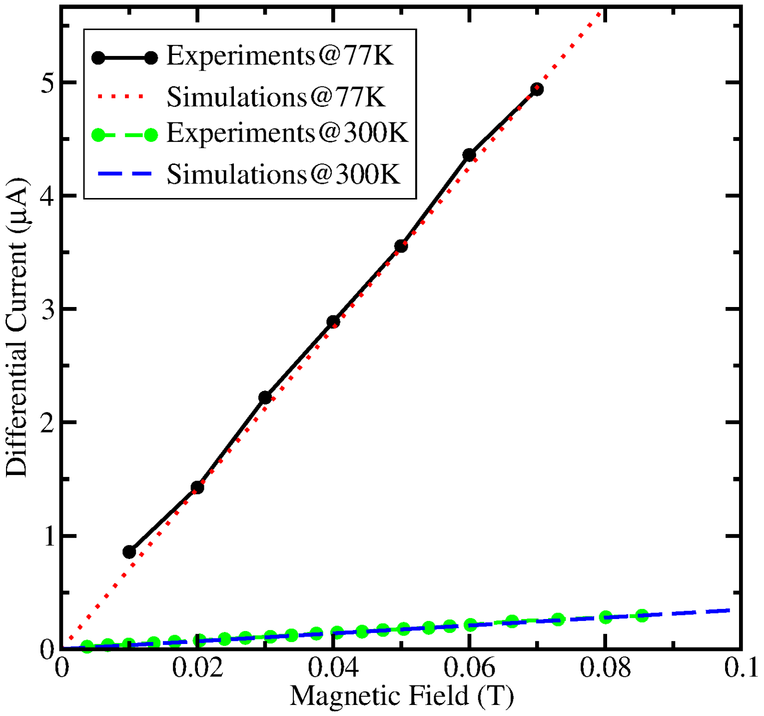

Figure 4.83: Differential current versus magnetic field at 77 K and 300 K.

At 77 K the relative sensitivity is 11.09 % T^{-1} according to (4.1). This value is notably higher compared to the room temperature value and even to other solid-state sensors. The improvement in the relative sensitivity is due to the increase in the electron mobility in the inversion layer. As it has been stated in (4.2), the higher the carrier mobility, the higher the carrier deflection. As a result, the differential current increases, as can be seen from Figure 4.83 where the 300 K case has been plot for a quick comparison.

4.3.3 Bias Dependence

As it has been shown in Section 4.2, the electro-magnetic interaction shows a complex behavior that can be explained in terms of the drift-diffusion process. At low temperature, some processes are enhanced (or reduced) [2, 17] modifying the general behavior of the device.

Figure 4.84 presents the relative sensitivity as a function of the gate voltage for different polarizations at the drains. Surprisingly it shows a complete different behavior as for room temperature (See Figure 4.7). As the drain to source voltage is increased, the relative sensitivity increases too. The carriers in the inversion layer are swept by the lateral electric field [17]. The larger the lateral electric field, the higher the mobility of the electrons in the inversion layer. As explained in Section 4.2, the relative sensitivity is higher at low gate voltages (see Figure 4.7), because the drain currents are comparable with the differential current.

Figure 4.85 shows how the differential current increases with respect to the gate voltage for a voltage of 1.0 V at the drains. The differential current at 77 K is almost 20 times higher as for the 300 K (see Figure 4.8), but at the same temperature operation a higher differential current does not mean a higher relative sensitivity, as can be seen from both figures.

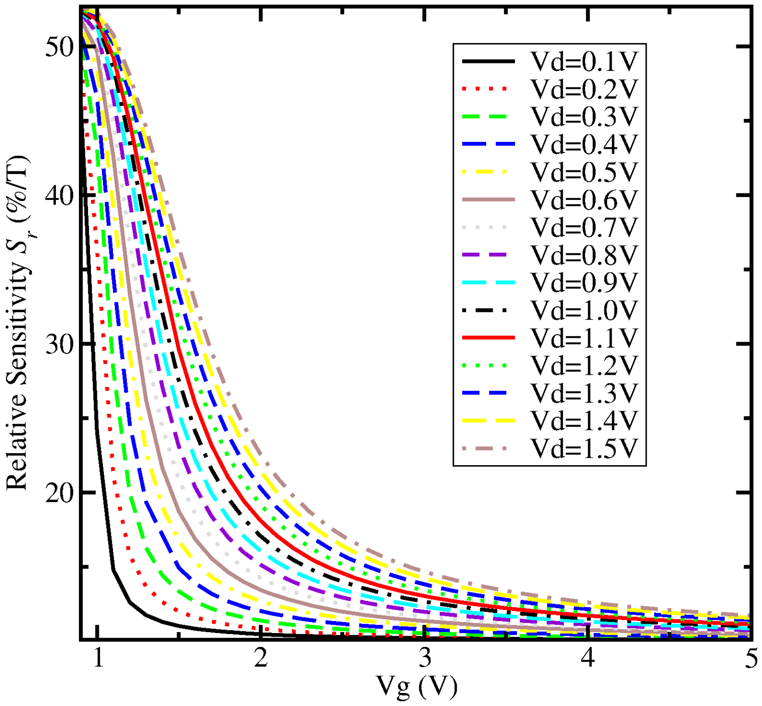

Figure 4.84: Simulated S_r as a function of the gate voltage at 77 K and 50 mT.

The 's' shape of the plots in the room temperature analysis (see Figure 4.7) has been explained by the transition between the diffusion and the drift process. Figure 4.86 shows the relative sensitivity as a function of the drain voltage for different gate voltages.

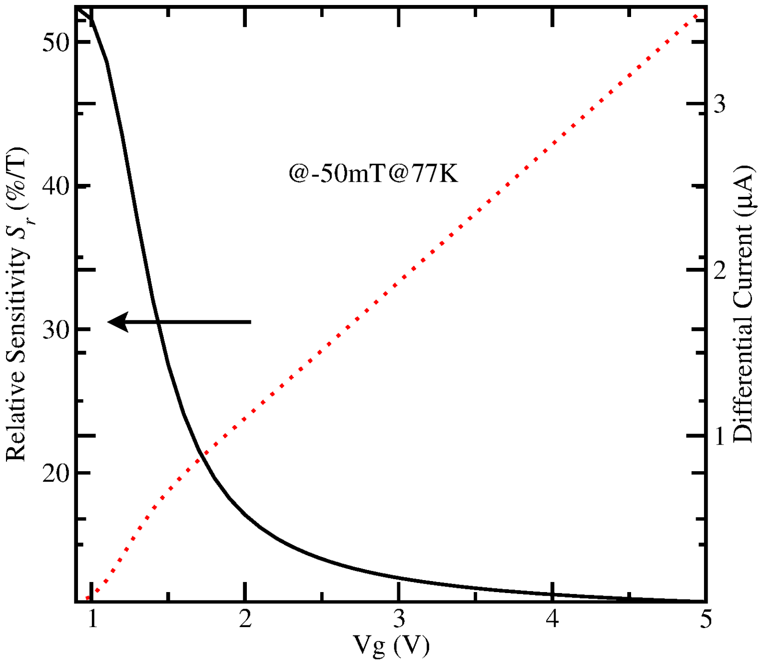

Figure 4.85: Simulated S_r and Δ for a gate swept. V_{D1} and V_{D2} are set to 1.0 V.

At low temperature, the various minima are not present, explaining that the carriers are swept by the lateral electric field. If this is true, no diffusion process exists at 77 K or it only exist at very low drain to source voltages which are not visible on the plots.

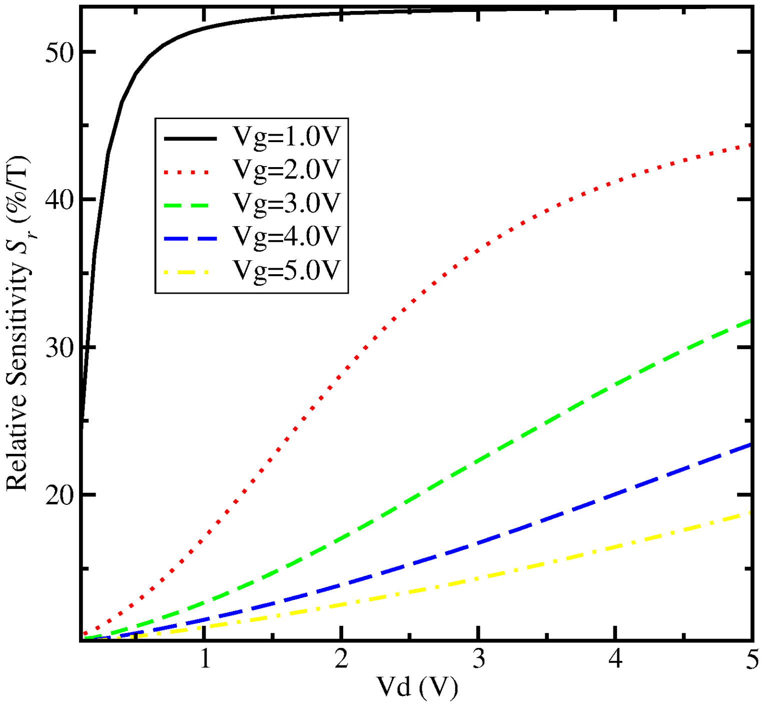

Figure 4.86: Simulated S_r as a function of the drain voltage at 77 K and 50 mT.

4.3.4 Channel Region

From the numerical point of view, the simulation of semiconductor devices at 77 K should not be different from the 300 K case, if critical quantities are properly scaled. Slight differences should come from the physical models used for the characteristic parameters. Except for high gate voltages, plots showing the potential, electron concentration, electric field, and electron mobility have a similar shape as their counterpart at 300 K. Having this in mind, only figures with evident differences are presented.

Figure 4.87 and Figure 4.88 show the potential inside the channel at 110 μm from the source and at 1 nm from the silicon oxide-silicon interface at 77 K for a gate voltage of 1 V and of 5 V, respectively, and different magnetic fields. Although the cuts are made close to the drains, Figure 4.3.4 is different from its 300 K counterpart, where the potential is stronger influenced by the gate than by the drains.

Figure 4.89 and Figure 4.90 show the electron concentration inside the channel at 110 μm from the source and at 1 nm from the silicon oxide-silicon interface at 77 K for a gate voltage of 1 V and of 5 V, respectively, and different magnetic fields. Except for the case of a gate voltage of 1 V, the electron concentration behaves differently as compared to the 300 K case (see Figures 4.52 and 4.57). This behavior can be attributed to the cryogenic operation of silicon devices. In this case the charge ionization, the process which electrically turns on the charges for electric conduction, is dominated by the electric field, because the carriers (in this case, electrons) obtain energy from both the lateral and the transversal electric field. The extreme points in the electron concentration in Figure 4.90 are the result of the influence of the lateral electric field.

Figure 4.91 and Figure 4.92 show the electric field inside the channel at 110 μm from the source and at 1 nm from the silicon oxide-silicon interface at 77 K for a gate voltage of 1 V and of 5 V, respectively, and different magnetic fields. Except for the case of a gate voltage of 1 V, the electric field behaves differently from the 300 K case.

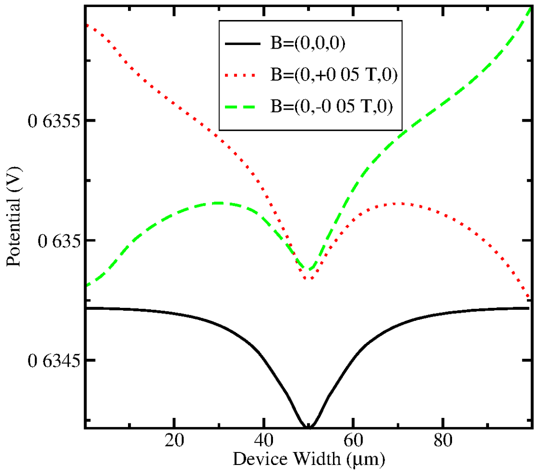

Figure 4.87: Potential in the channel @(110μm,77K,Vg=1.0V).

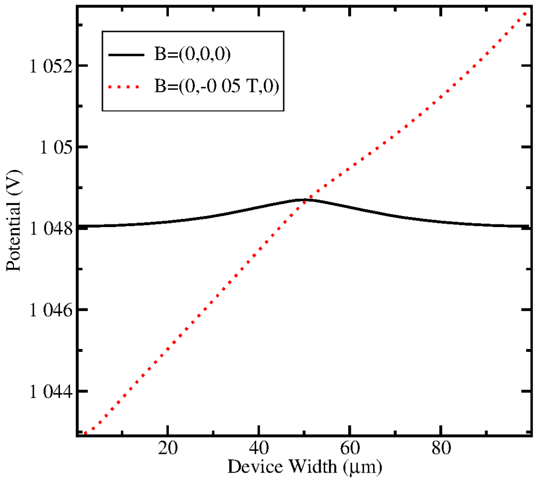

Figure 4.88: Potential in the channel @(110μm,77K,Vg=5.0V).

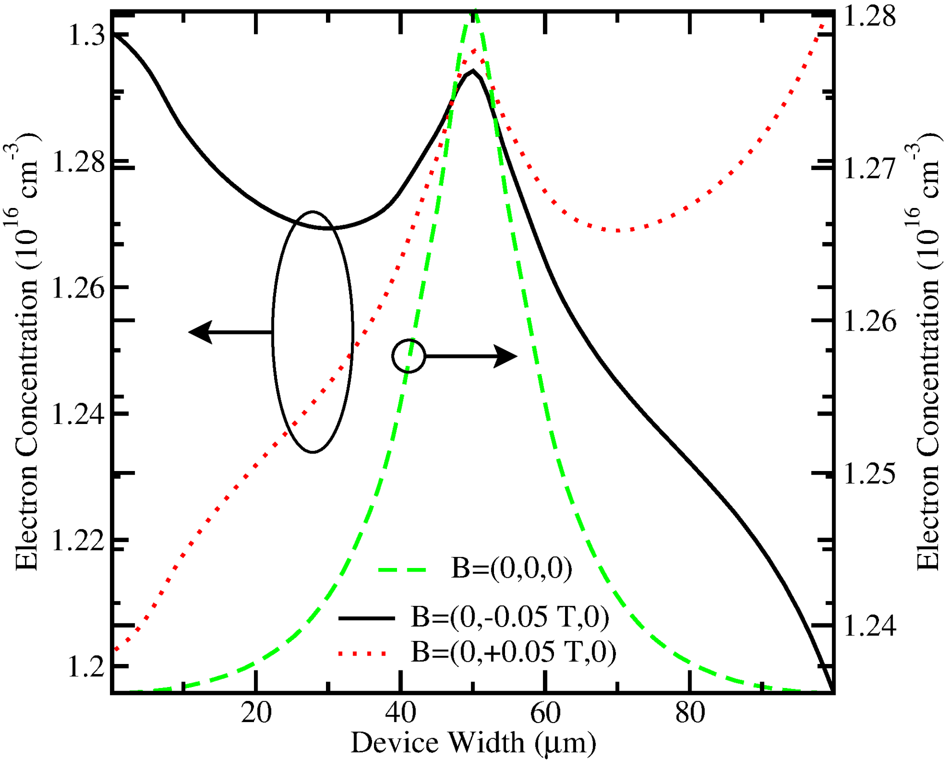

Figure 4.89: Electron concentration in the channel @(110μm,77K,Vg=1.0V).

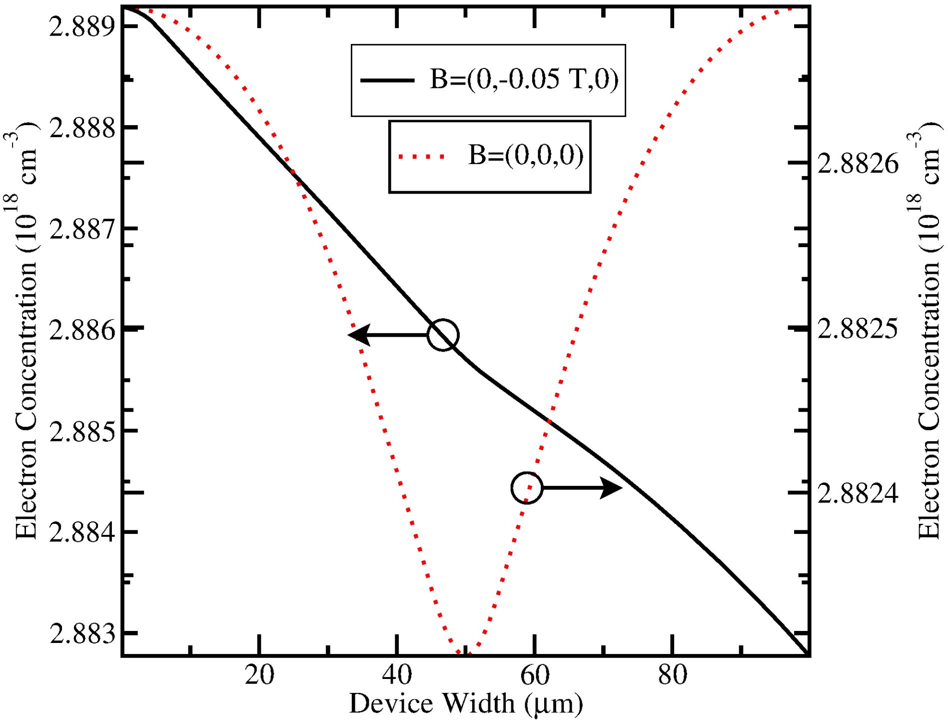

Figure 4.90: Electron concentration in the channel @(110μm,77K,Vg=5.0V).

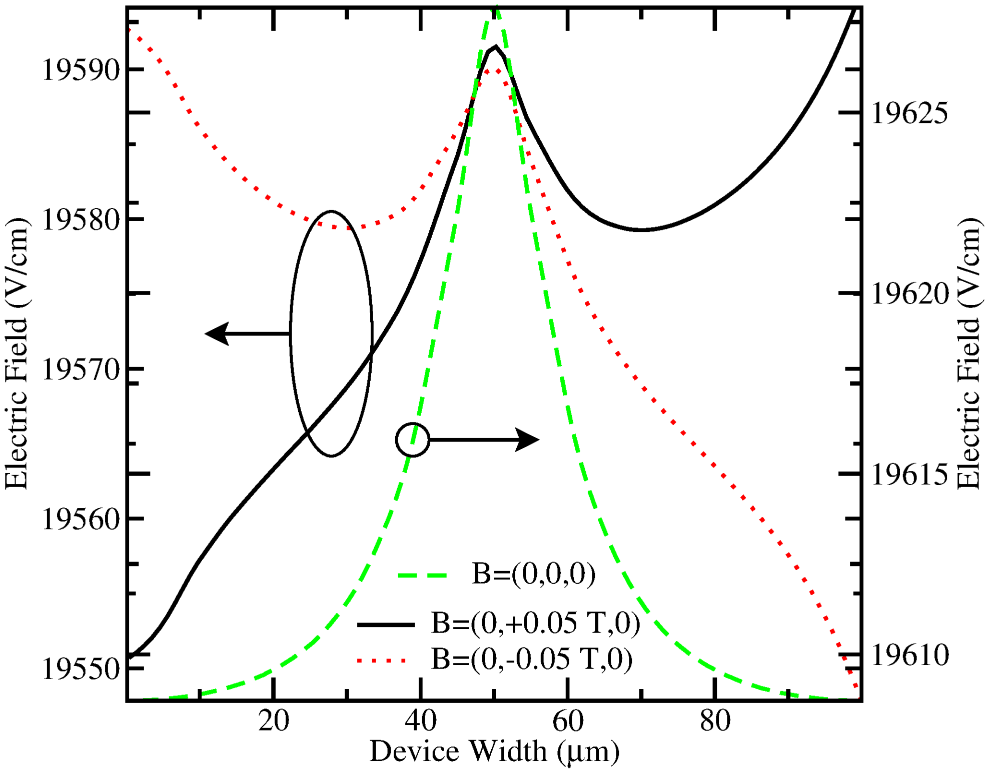

Figure 4.91: Electric field in the channel @(110μm,77K,Vg=1.0V).

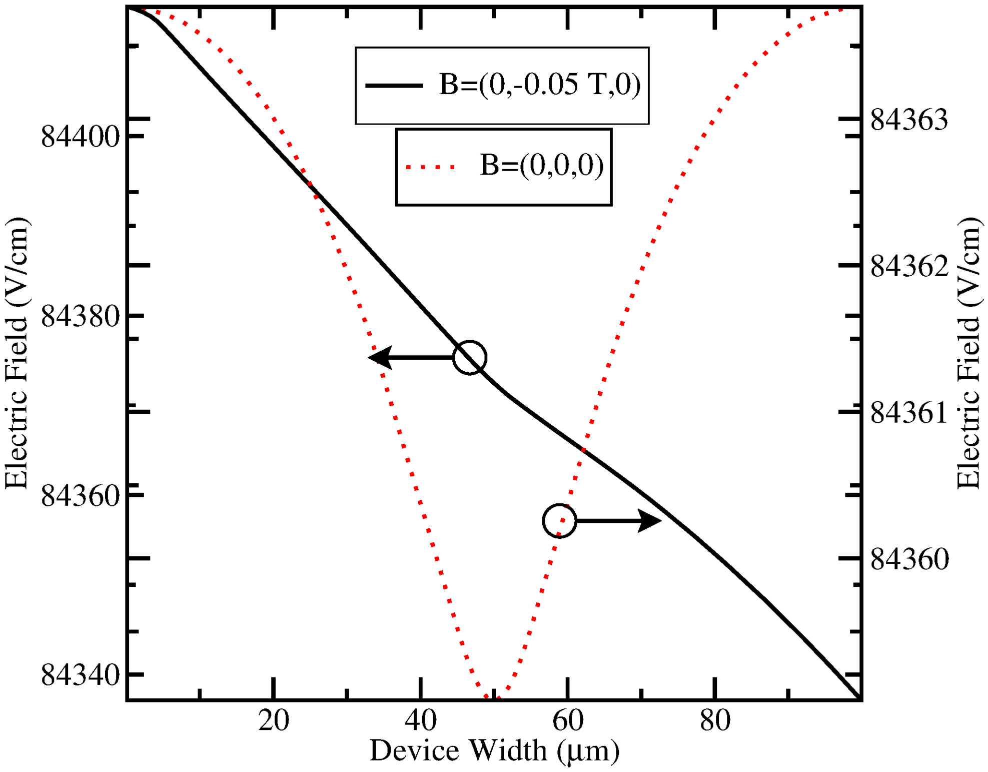

Figure 4.92: Electric field in the channel @(110μm,77K,Vg=5.0V).

4.4 Geometric Parameters

From Figure 4.1 three geometric parameters for the two-drain MAGFET can be identified: the length of the device, the width of the device, and the distance between the drains. From (4.2) it is clear that longer devices will give higher differential currents, because there is more "path" for the carriers to be deflected before they reach the drains. Wider devices will give higher differential currents, because there are more current lines to be deflected. Finally, the smaller the separation between the drains, the higher the differential current will be, because any minor deflection will be detected by the drains [42].

In order to verify these statements, some simulations are carried out with the following bias: a gate voltage of 4.95 V, 1.0 V at the drains, and 0.0 V at the source and substrate. The applied magnetic field is 50 mT and the simulations are carried out at both 300 K and 77 K. The Hall scattering factor for electrons has been set to a constant value of 0.8 for all the simulation results in this section. The geometry of the two-drain MAGFET is as follows: in the simulation results presented in Figure 4.93 the width and length of the two-drain MAGFET are set to 100 μm and 125 μm respectively. In the simulations results presented in Figure 4.94 the width of the two-drain MAGFET is set to 100 μm and the distance between the drains is set to 10 μm. In the simulation results presented in Figure 4.95 the length of the two-drain MAGFET is set to 125 μm and the distance between the drains is 10 μm.

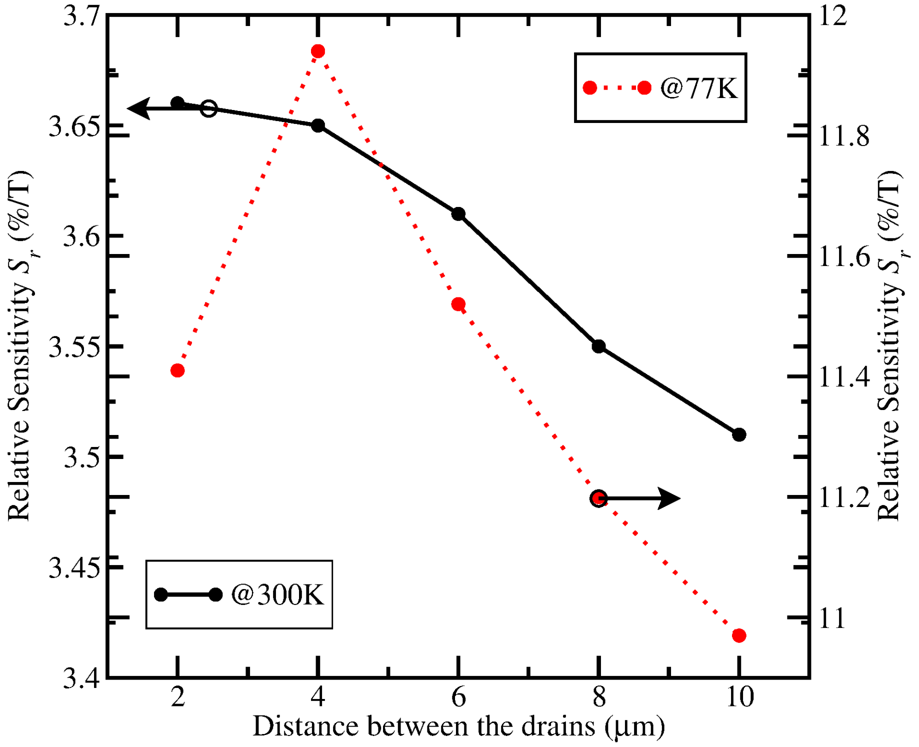

Figure 4.93: Simulated S_r for different distances between the drains.

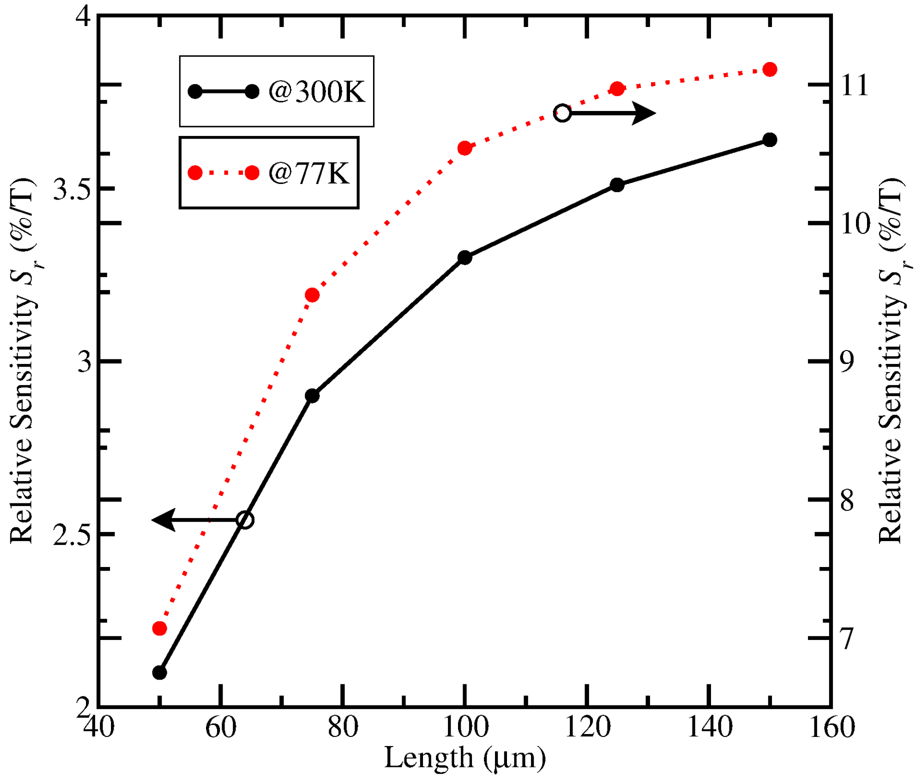

Figure 4.94: Simulated relative sensitivity for different lengths.

Figure 4.93 shows simulation results for different distances between the drains. As it can be seen, the separation distance does not play a dominant role in the general behavior of the two-drain MAGFET. At 300 K, the relative sensitivity increases from 3.51 % T^{-1} at a separation distance between drains of 10 μm, to 3.66 % T^{-1} at a separation distance between drains of 2 μm. Even at 77 K little improvement is obtained, where the relative sensitivity increases from 10.97 % T^{-1} at a separation distance between drains of 10 μm, to a maximum of 11.94 % T^{-1} at a separation distance between drains of 4 μm, and afterwards the relative sensitivity decreases.

Figure 4.94 shows how the relative sensitivity is improved as the length of the device is increased, as it is predicted by (4.2). At 300 K, the relative sensitivity increases from 2.10 % T^{-1} to 3.64 % T^{-1}. However, at 77 K the improvement of the relative sensitivity is very high, going from 7.07 % T^{-1} to 11.11 % T^{-1}. Finally, Figure 4.95 shows the relative sensitivity for different widths. As is also reported in [42], the relative sensitivity shows a maximum as the width is increased. At 300 K, the relative sensitivity increases from 2.75 % T^{-1} to a maximum of 3.56 % T^{-1} at a width of 120 μm. However, at 77K, the relative sensitivity increases from 6.45 % T^{-1} to a maximum of 13.67 % T^{-1} at a width of 190 μm. The fact that both maxima are not at the same width can be explained in terms of the cryogenic operation of the MAGFET: at room temperature operation, the scattering mechanisms are so strong that degrade the sensitivity of the device. At low temperature operation, those scattering mechanisms are reduced.

4.5 Conclusions

Full three-dimensional device simulations of a two-drain MAGFET taking into account a magnetic field have been carried out. A perfect match between simulation results and experimental data is obtained at room temperature and liquid Nitrogen temperature. Although the value of the Hall scattering factor for the electrons seems to be a little lower at 300 K in comparison to those values found in the literature, the simulation results show that the electric performance of the two-drain MAGFET with the magnetic field have a meaningful behavior as one would expect from basic physics.

The improvement of the relative sensitivity of the two-drain MAGFET at 77 K with both experimental data and simulation results has been shown. Despite the simulation results at 77 K with no magnetic field are not as good as those at 300 K, the increase in the differential current at 77 K has been reproduced. The simulation results of the electric performance of the two-drain MAGFET with magnetic field at 77 K have been explained using basic physics concepts, specially MOSFET physics.

The geometric dependence of the relative sensitivity has been shown at both 300 K and 77 K. Whereas only little improvement of the relative sensitivity at 300 K is obtained, a significant improvement of the relative sensitivity of the two-drain MAGFET at 77K is obtained.

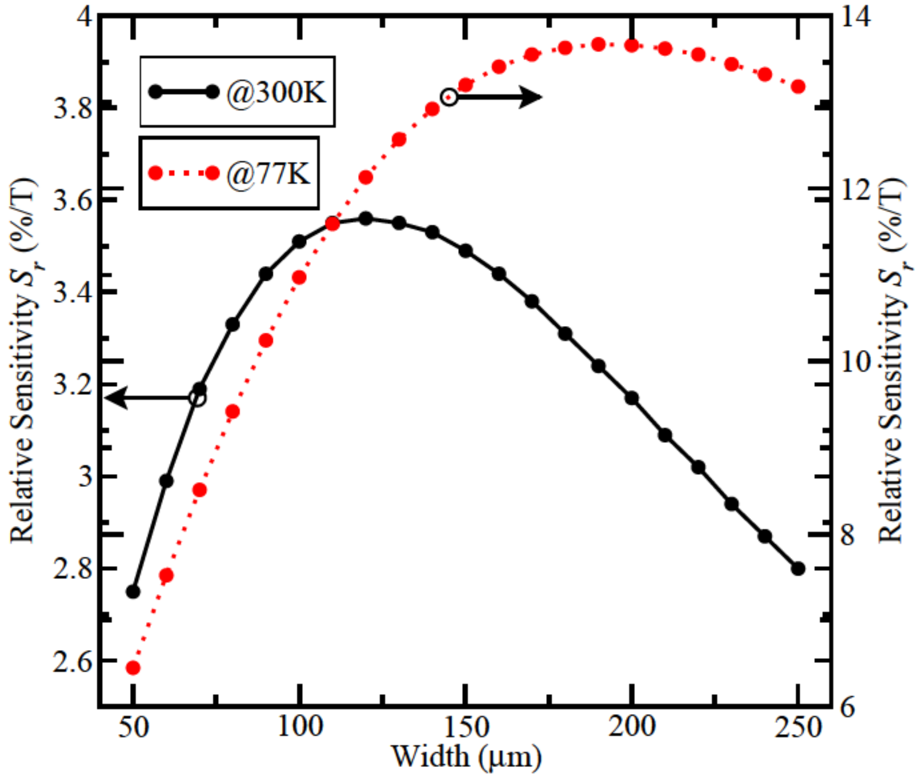

Figure 4.95: Simulated relative sensitivity for different widths.

Chapter 5

Three-Drain MAGFET

5.1 The Structure

A three-drain MAGFET is as old as the first MOS Hall plate device [14]. It was first proposed in [10, 20] where it is suggested to bound together the Hall voltage terminals and the drain to form a three-drain MAGFET. As stated by Gallagher [14], in a MOS Hall plate device the Hall voltage terminals should be placed as close as possible to the

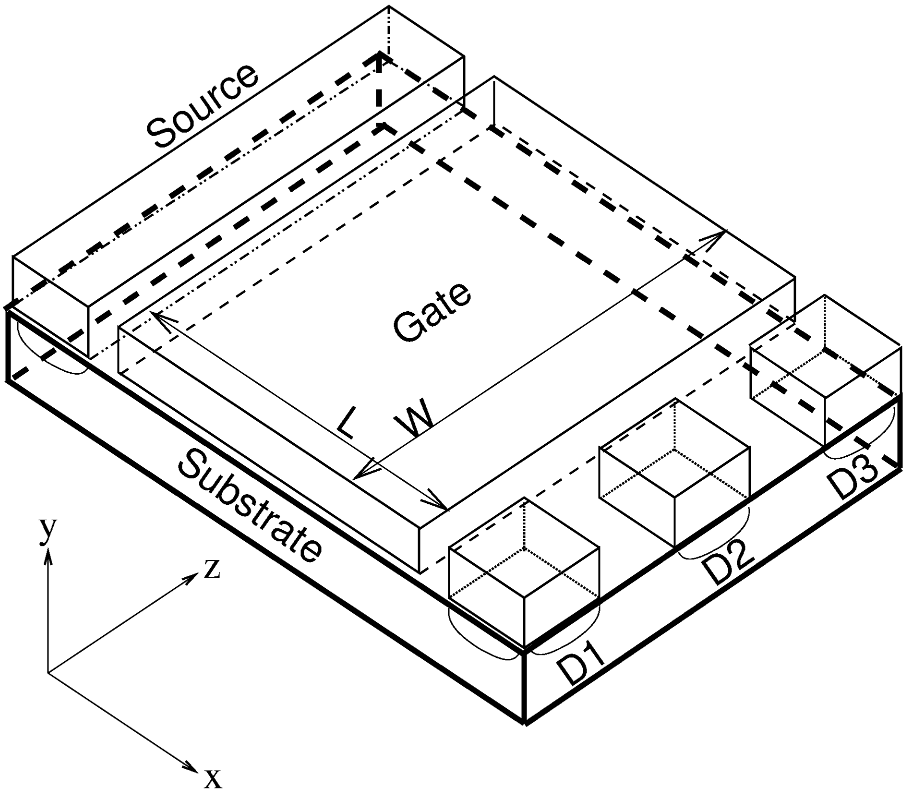

Figure 5.1: Three-drain MAGFET structure.

drain terminal in order to sense the Hall voltage and not to interfere with the electric behavior of the MOSFET. That is the reason why in [10, 20] the proposal of a three-drain MAGFET using Hall plates has been given. By taking the central drain current as a reference, a differential current is sensed on the lateral drains. However, no simulation results or experimental data showing the three-drain MAGFET as a magnetic sensor with a differential current output have been published yet.

In principle, the three-drain MAGFET looks exactly as a two-drain MAGFET (see Figure 4.1). The only difference is that the drain is split in three parts. Because of the lack of experimental data, this chapter only shows simulation results of this structure using the characteristics of a 10 μm standard CMOS process. In the following analysis the investigated three-drain MAGFET has a W/L ratio of 0.64 ($W = 80\,\mu$m and $L = 125\,\mu$m) and a distance between the drains of 10 μm.

5.2 Analysis at 300 K

The relative sensitivity of the three-drain MAGFET differs from the two-drain MAGFET. In the later the differential current comes from the fact that only two drain currents exist. In the case of a three-drain MAGFET, at least three differential currents can be defined. The central drain is used as a reference current and the differential current will be taken between the lateral drains. If the three drains are labeled as D1, D2 and D3, being D2 the central drain, then the relative sensitivity of a three-drain MAGFET is defined as follows:

$$S_r = \frac{|I_{D1} - I_{D3}|}{(I^0_{D1} + I^0_{D2} + I^0_{D3})|\mathbf{B}|} \tag{5.1}$$

where I_{D1} and I_{D3} are the currents at Drain 1 and Drain 3 when the magnetic field is applied, I^0_{D1}, I^0_{D2}, and I^0_{D3} are the drain currents when the magnetic field is not applied, and $\mathbf{B}$ is the magnetic field.

5.2.1 Electrical Characteristics

Figure 5.2 shows the electrical characteristics of the three-drain MAGFET with zero magnetic field. Although the drains are equally divided (20 μm width each drain) and set to the same level voltage (1.0 V; source and substrate are set to 0.0 V), the total current is not equally shared by them. The central drain current is higher than the lateral drain currents of the three-drain MAGFET structure. The currents at Drain 1 and Drain 3 are equal, so it is expected that they should experience an imbalance when a magnetic field is applied.

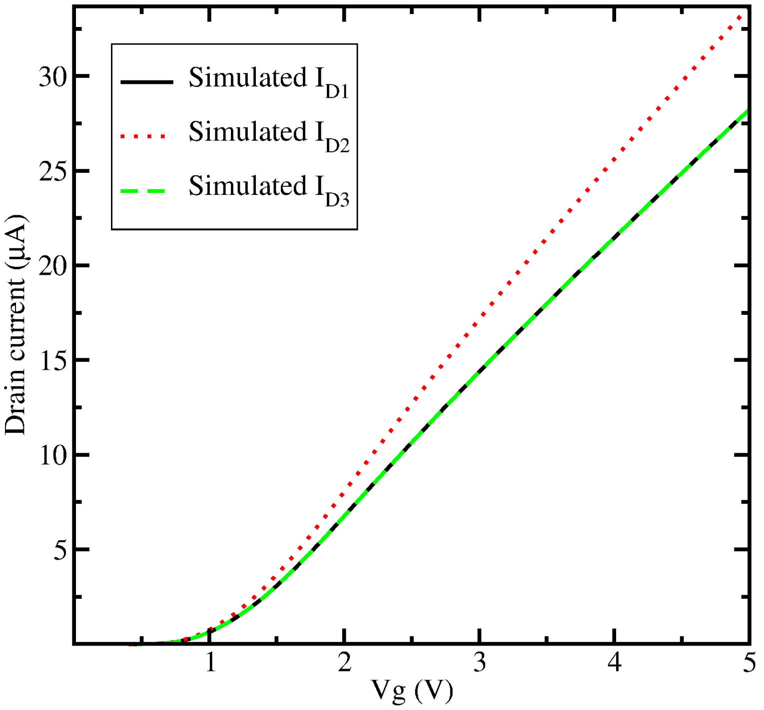

Figure 5.2: Simulated drain currents as a function of the gate voltage at 300 K.

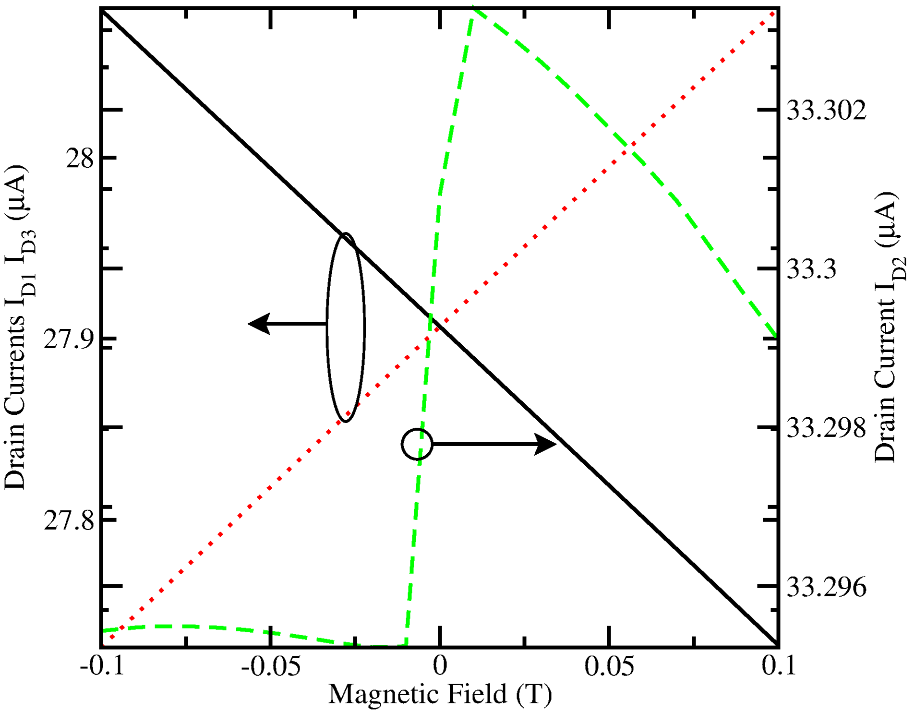

Figure 5.3: Simulated drain currents versus magnetic field at 300 K.

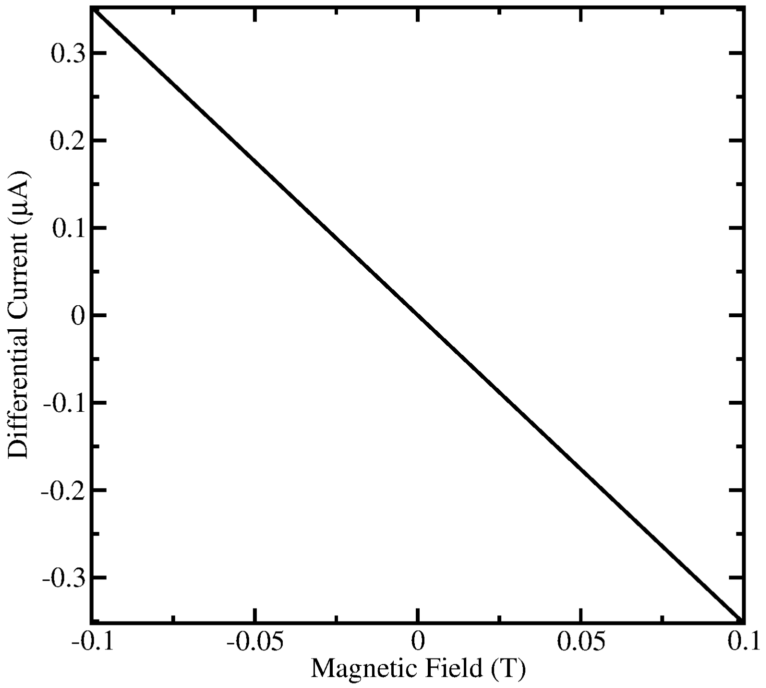

Figure 5.4: Simulated differential current versus magnetic field at 300 K.

5.2.2 Magnetic Field

Figure 5.3 shows how the drain currents are modified when a magnetic field is applied. The three-drain MAGFET is oriented in the same way as the two-drain MAGFET (see 4.2.2). The drain biases are set to 1.0 V, the gate is set to 4.95 V, and the source and substrate are set to 0.0 V. Whereas the current at Drain 1 increases as the magnetic field increases in the negative direction, the current at Drain 3 decreases proportionally. Once the magnetic field is reversed in sign, the opposite effect is observed.

Theoretically, as a result of the Lorentz force, the Drain 1 collects some of the deflected current lines from Drain 2, while Drain 3 losses current lines that are in turns collected by Drain 2. As a general result, the current in Drain 2 remains practically constant. A close up to the central drain current shows some changes that are attributed to a magnetoresistance effect.

Figure 5.4 shows the differential current as a function of the magnetic field. In this case the differential current is taken between Drain 1 and Drain 3.

5.2.3 Bias Dependence

The relative sensitivity of the three-drain MAGFET is shown in Figure 5.5 as a function of the gate voltage for different drain voltages. The simulation results show that the three-drain MAGFET has a higher relative sensitivity compared with the two-drain structure shown in the previous chapter (see Figure 4.7). A minimum relative sensitivity

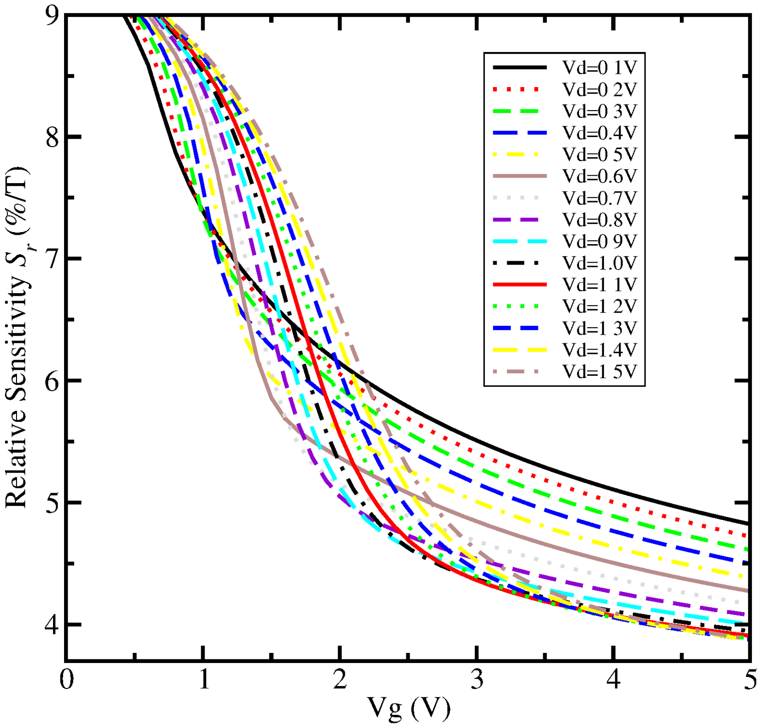

Figure 5.5: Simulated S_r as a function of the gate voltage at 300 K and 50 mT.

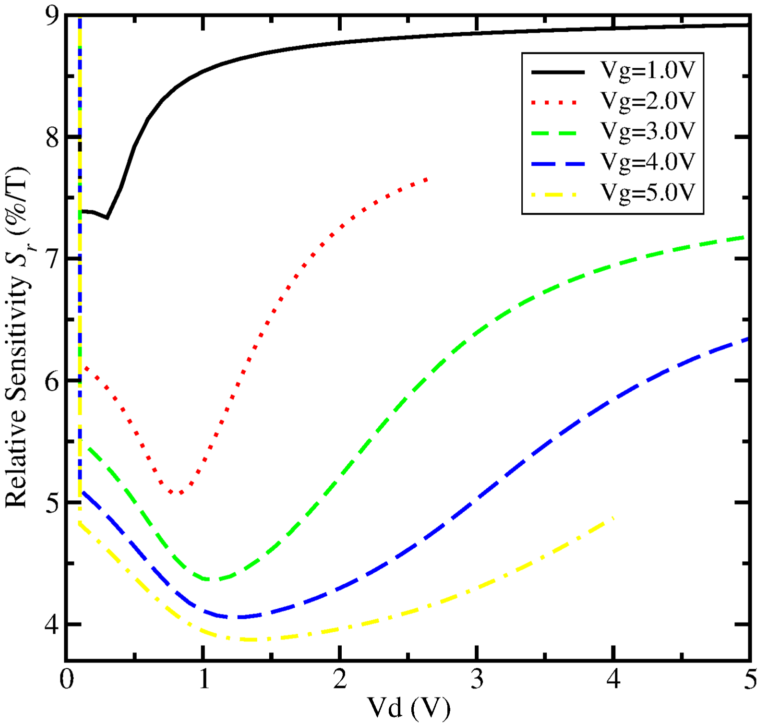

Figure 5.6: Simulated S_r as a function of the drain voltage at 300 K and 50 mT.

of $3.87\ \%\ \mathrm{T}^{-1}$ is obtained whereas the minimum in the two-drain MAGFET is $2.62\ \%\ \mathrm{T}^{-1}$.

As described in the previous chapter, the 's' shape of the plots in Figure 5.5 can be explained in terms of how the carriers move inside the channel, diffusion or drift, as can be seen in Figure 5.6. Once again, the various minima show the transition between diffusion and drift, that means, the transition between the linear regime and the saturation regime of the MOSFET structure.

As it was explained in the previous chapter, the gate and the drain voltages modulate the channel thickness that has a great impact on the sensor response. However, in the present analysis the relative sensitivity is a function of the polarization, because the total drains current plays an important role: the higher the drain currents, the higher the differential current although it implies a lower relative sensitivity.

5.3 Analysis at 77 K

As it has been shown in Chapter 4 for the low temperature analysis of the two-drain MAGFET, the relative sensitivity is improved as the device is cooled down to liquid Nitrogen temperature. This improvement comes from the fact that the electron mobility in the inversion channel increases at such temperatures. So, it is expected that the three-drain MAGFET would show such an improvement too.

5.3.1 Electrical Characteristics

Figure 5.7 shows the electrical characteristics of the three-drain MAGFET with zero magnetic field. As in the room temperature analysis, the central current at Drain 2 is higher that in the lateral Drains 1 and 3. The bias is as follows: the drains are set to 1.0 V and the source and substrate are set to 0.0 V.

5.3.2 Magnetic Field

Figure 5.8 shows how the drain currents are modified when a magnetic field is applied at 77 K. As in the 300 K analysis, the bias is as follows: the drains are set to 1.0 V, the gate is set to 4.95 V, and the source and substrate are set to 0.0 V. As it can be seen, there is no qualitative difference between Figures 5.3 and 5.8. As expected, at 77 K the differential current is higher than at 300 K case by almost a factor of 10 (see Figure 5.9).

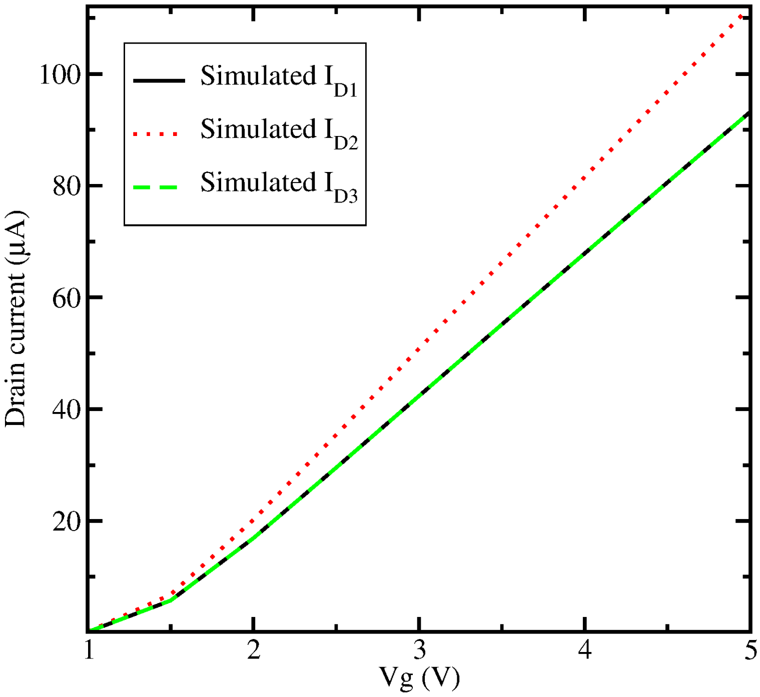

Figure 5.7: Simulated drain currents as a function of the gate voltage at 77 K.

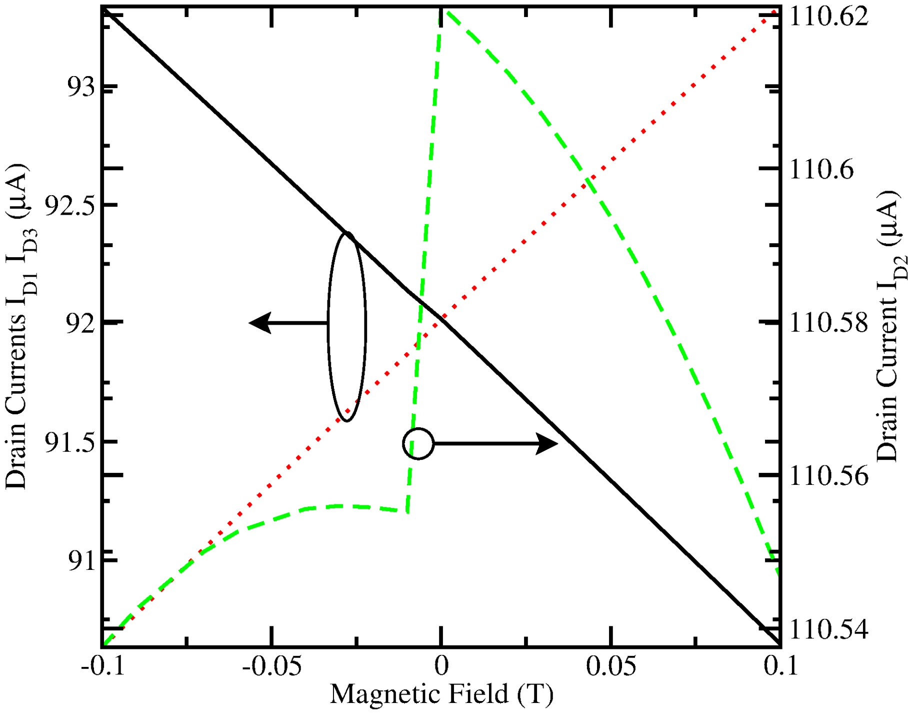

Figure 5.8: Simulated drain currents versus magnetic field at 77 K.

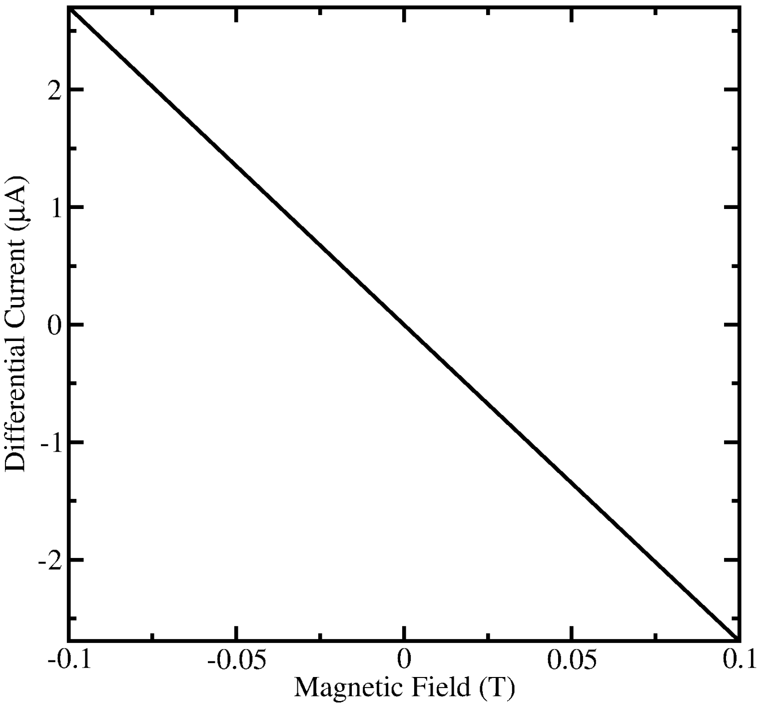

Figure 5.9: Simulated differential current versus magnetic field at 77 K.

5.3.3 Bias Dependence

The relative sensitivity of the three-drain MAGFET is shown in Figure 5.10 as a function of the gate voltage for different drain voltages at 77 K. As expected, the simulation results show that the three-drain MAGFET has a higher relative sensitivity at 77 K than at 300 K. However, the improvement in the relative sensitivity is not as high as in the two-drain MAGFET analysis, where a maximum of almost 55 % T^{-1} can be reached whereas a maximum of 40 % T^{-1} for the three-drain MAGFET is achieved. A plausible explanation is that the central current at Drain 2 is higher as the drain currents at Drain 1 and Drain 3, decreasing the relative sensitivity.

Figure 5.10 shows an important detail. Except from the plot where the drains are set to 0.1 V, in the other plots the relative sensitivity shows an increasing behavior while increasing the lateral electric field. A possible explanation is that the three-drain MAGFET at 77 K and at 0.1 V at the drains experiences both drift and diffusion of carriers in the inversion channel.

Figure 5.11 shows the relative sensitivity of the three-drain MAGFET as a function of the drain voltage for different gate voltages at 77 K. Compared with Figure 4.86, both Figures show the same shape. Once again, the improvement is not as high as in the two-drain MAGFET. The high central current at Drain 2 explains the *lower* improvement in the relative sensitivity.

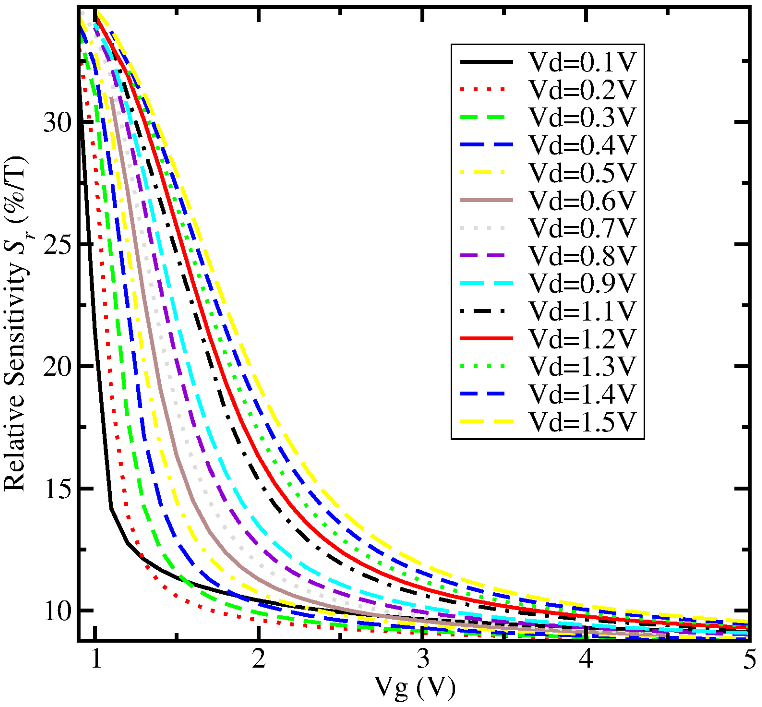

Figure 5.10: Simulated S_r as a function of the gate voltage at 77 K and 50 mT.

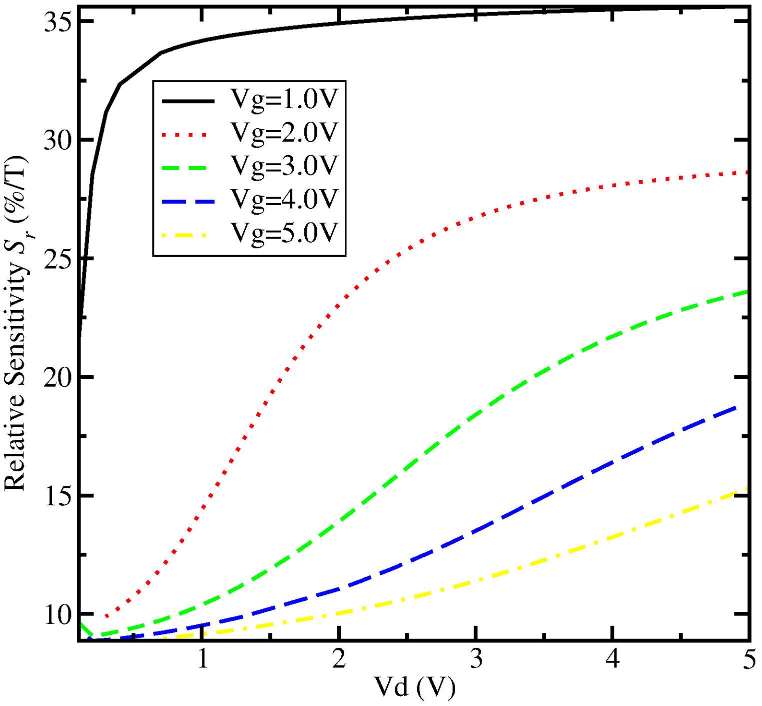

Figure 5.11: Simulated S_r as a function of the drain voltage at 77 K and 50 mT.

5.4 Geometric Parameters

As in the two-drain MAGFET analysis, the three-drain MAGFET has the same geometric parameters that play an important role in the relative sensitivity. However, extra parameters can be identified. For example, it is quite clear that the distance between the drains can be independently modified but this will lead to an undesirable offset, because the currents at the lateral drains will not be equal.

Figure 5.12 shows simulations results for the relative sensitivity at different drain distances and temperatures. The simulated three-drain MAGFET has a width of 80 μm and a length of 125 μm. The drains are set to 1.0 V, the gate to 4.95 V, and the source and substrate to 0.0 V. The magnetic field is set to 50 mT. A maximum relative sensitivity of 4.32 % T^{-1} and 11.10 % T^{-1} can be seen for a distance between drains of 4 μm at both 300 K and 77 K, where the drains almost share equally the total drain current. As the distance between the drains increases, the total drain current is equally shared by the drains.

Figure 5.13 shows the simulation results for the relative sensitivity at different lengths and temperatures. The simulated three-drain MAGFET has a width of 80 μm and a distance between drains of 10 μm. The drains are set to 1.0 V, the gate to 4.95 V, and the source and substrate to 0.0 V. The magnetic field is set to 50 mT. As predicted by (4.2), the relative sensitivity increases from 2.75 % T^{-1} to 4.08 % T^{-1} at 300 K, and from 6.75 % T^{-1} to 9.18 % T^{-1} at 77 K. However, in absolute terms, this improvement is not as high as in the two-drain MAGFET analysis, even at 77 K.

Figure 5.14 shows the simulation results for the relative sensitivity at different widths. The simulated three-drain MAGFET has a length of 125 μm and a distance between drains of 10 μm. The drains are set to 1.0 V, the gate to 4.95 V, and the source and substrate to 0.0 V. The magnetic field is set to 50 mT. As in the two-drain MAGFET analysis, a maximum in the relative sensitivity can be seen at both, 300 K and 77 K. At 300 K, the maximum is of 4.19 % T^{-1} for a device width of 125 μm, and at 77 K, the maximum is of 11.54 % T^{-1} for a device width of 155 μm.

Figure 5.15 shows the simulations results for the relative sensitivity at different sizes of the central drain. The simulated three-drain MAGFET has a length of 125 μm, a width of 80 μm, and a distance between drains of 10 μm. The drains are set to 1.0 V, the gate to 4.95 V, and the source and substrate to 0.0 V. The magnetic field is set to 50 mT. A tendency cannot be stated unless the magnitude of the drain currents for the zero magnetic field are analyzed. For a central drain size of 12 μm, a maximum in the relative sensitivity of 4.56 % T^{-1} at 300 K and 13.00 % T^{-1} at 77 K can be observed. The magnitude of the central drain current is almost the half of the lateral drain currents: $I_{D2} = 20.86\,\mu$A, $I_{D1,3} = 34.60\,\mu$A at 300 K, and $I_{D2} = 56.93\,\mu$A, $I_{D1,3} = 133.70\,\mu$A at 77 K (See also Figure 5.16). Because the magnitude of the reference current is low, the relative sensitivity is high, according to expression (5.1). However, the magnitude of the central drain current cannot be set as a general rule because the central drain current for the drain size of 8 μm is high as for the lateral drain currents and it gives a

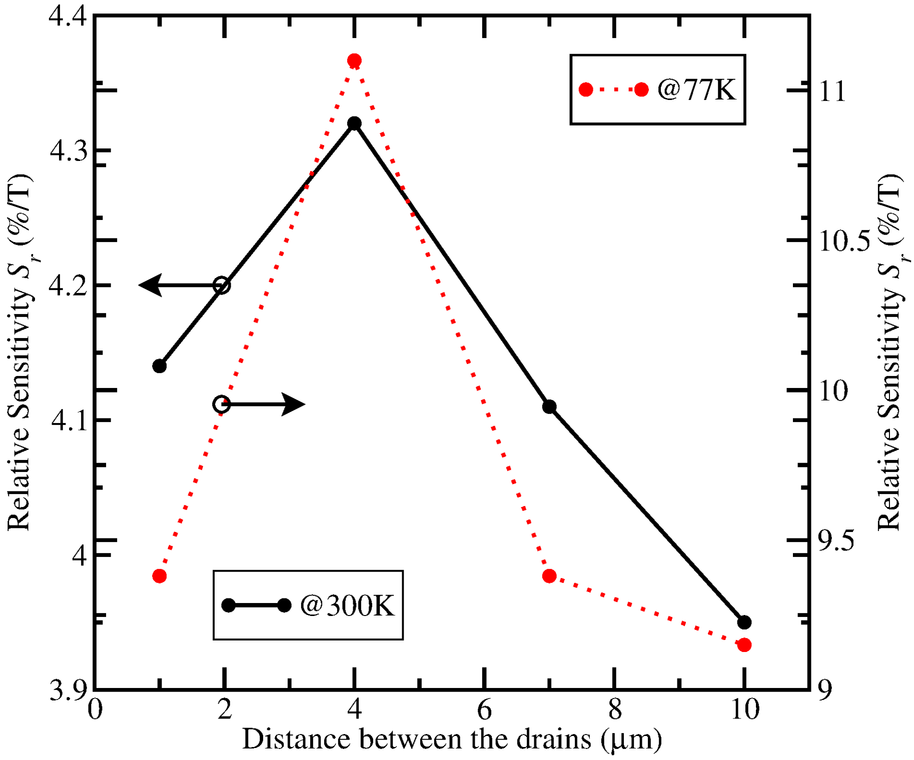

Figure 5.12: Simulated S_r for different distances between the drains.

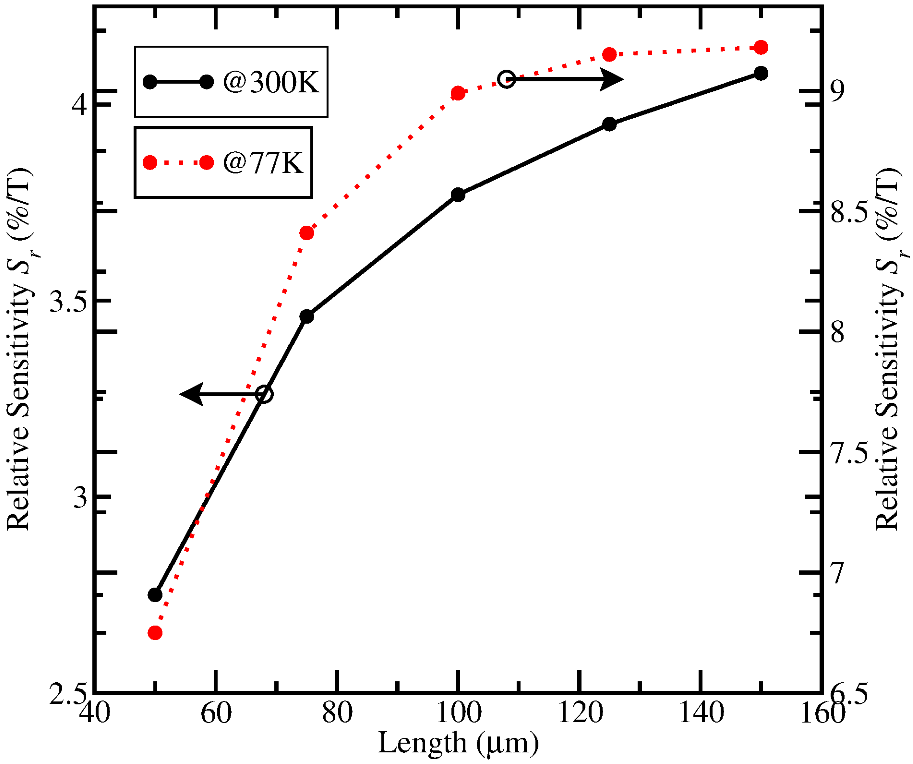

Figure 5.13: Simulated relative sensitivity for different lengths.

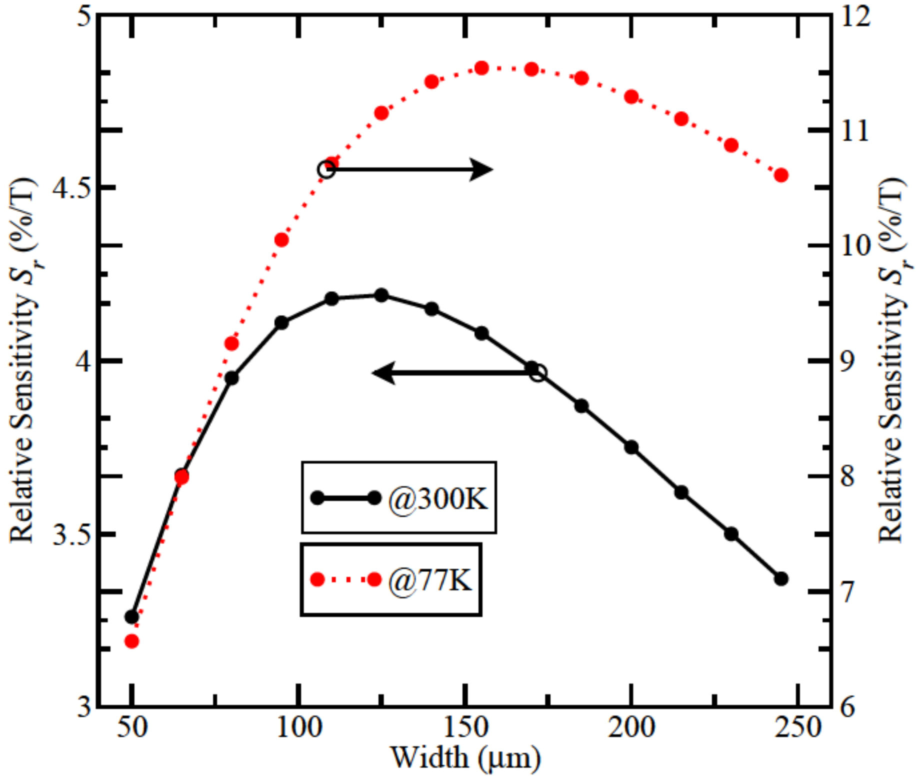

Figure 5.14: Simulated relative sensitivity for different widths.

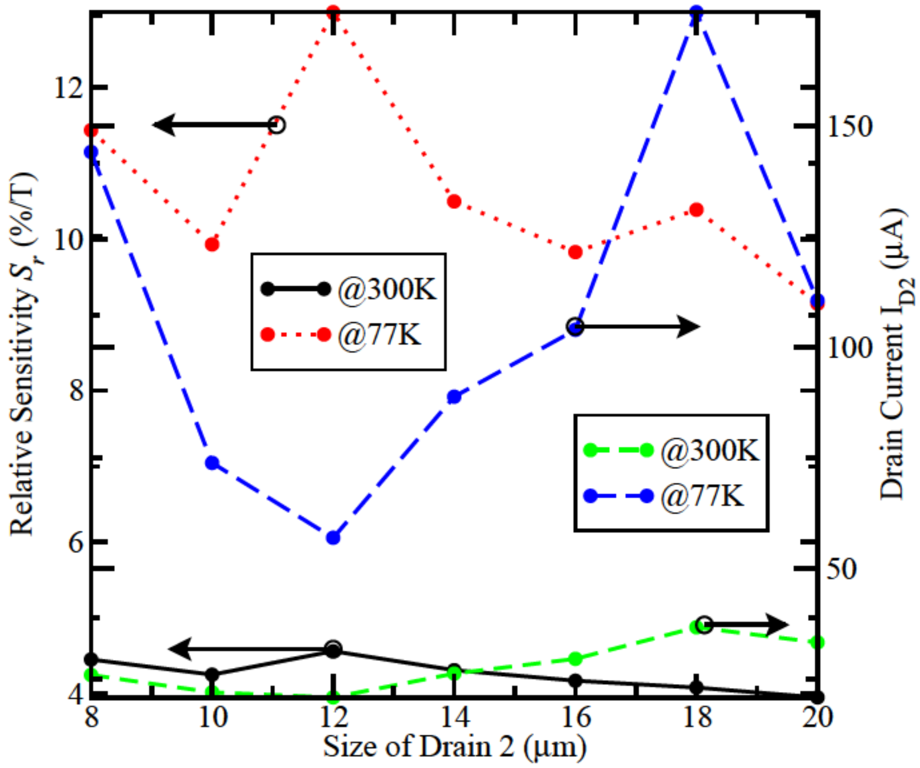

Figure 5.15: Simulated S_r and I_{D2} for different sizes of Drain 2.

pretty high relative sensitivity at both 300 K and 77 K. A complex relation between lowering the drain current at the Drain 2 or sharing equally the total drain current exists.

5.5 Conclusions

Full three-dimensional simulations of a three-drain MAGFET taking into account a magnetic field have been carried out. By using the default values of the various physical models, the relative sensitivity has been simulated at various bias conditions and geometric conditions. The differential current at the lateral drains of the three-drain MAGFET shows that the three-drain MAGFET would have a better performance at room temperature than the two-drain MAGFET. However, the performance of the three-drain MAGFET at liquid Nitrogen temperature is not as highly improved as in the two-drain MAGFET analysis.

A plausible explanation of this behavior can be given in terms of drain current magnitudes. Because the central drain current is higher than the lateral currents, at low temperature operation such currents also increase in magnitude. Although the differential current increases too, the central drain currents rises so rapidly that the relative sensitivity decreases. From the simulations results given in the previous section, the sharing of the total drain current by the drains shows a complex interaction with the magnetic field. Experimental data would be helpful to better determine and analyze this interaction.

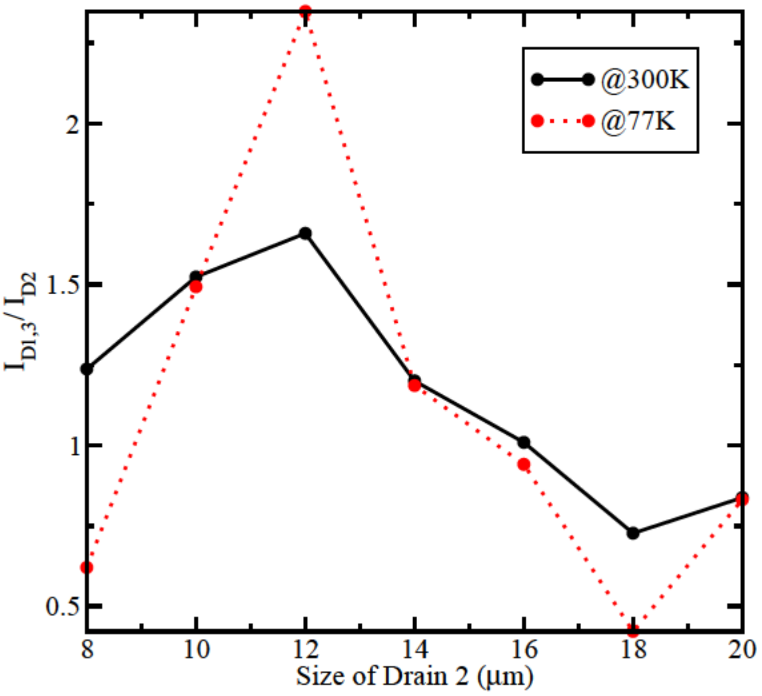

Figure 5.16: Simulated $I_{D1,3}/I_{D2}$ ratio for different sizes of Drain 2.

Chapter 6

Summary and Outlook

Modeling of galvanomagnetic effects in semiconductors has been performed using the general purpose device simulator MINIMOS-NT. By implementing a new discretization procedure that takes into account an arbitrary magnetic field, full three-dimensional simulations of a two- and three-drain MAGFETs were carried out. The simulation results obtained with this new discretization agree with experimental data of the two-drain MAGFETs at both 300 K and 77 K.

The new discretization procedure was implemented using a physical model that comprises both magnetic field and the current density. Although the original model includes thermoelectric and thermomagnetic effects, an isothermal approximation of the equation is sufficient for the modeling of magnetic sensors. Because the carrier transport equations are not directly modified by the presence of a magnetic field, in principle any transport equation can be used for the simulation of magnetic effects in semiconductors, in particular also a hydrodynamic transport model.

The main figure of merit from a magnetic sensor is the relative sensitivity. As it has been experimentally shown, the relative sensitivity of a two-drain MAGFET can be improved by cooling the device to 77 K. This improvement comes from the fact that the electron mobility in the inversion layer increases. As a result, the differential current increases and the relative sensitivity is improved. Smaller magnetic fields can be detected with the same magnetic sensor by cooling it to liquid Nitrogen temperature. Simulation results show this improvement. In addition the bias dependence of this relative sensitivity has been investigated at both room temperature and liquid Nitrogen temperature.

Also, the geometric dependence of the relative sensitivity has been analyzed at both 300 K and 77 K. As theory predicts, longer and wider devices will give better performance. However, if the device is going to be operated at both 300 K and 77 K, simulation results indicate that the maximum is not reached at the same device width.

An improvement of the relative sensitivity can be obtained if a three-drain MAGFET structure is used. Simulation results show such an improvement at room temperature although the performance at 77 K is not spectacularly improved as in the two-drain MAGFET case. However, a particular problem arises using a three-drain MAGFET structure, namely the match of the currents at the drains. Splitting the drain into two parts does not represent an important difficulty, but splitting the drain into three parts is difficult. Chances of getting a mismatch between the side drains are higher.

Although the Hall scattering factor for electrons, used for modeling the magnetic effects in semiconductors, is close to unity according to many sources in the scientific literature, the analysis of the two-drain MAGFET shows that this value is lower from the values found in the literature. This difference can be attributed to the different CMOS technologies. Modern CMOS technologies are used for the measurement of the Hall scattering factor whereas the CMOS process of the two-drain MAGFET is older. The value of the substrate doping is different in both technologies and this affects the scattering mechanisms in the channel.

Another important feature of the new discretization procedure is that it does not affect the matrix properties of the Jacobian (positive diagonal entries), an important feature from the numerical point of view. Those properties of the Jacobian guarantee the existence of a solution and the non-diagonal entries would not compromise the existence of a solution. Fortunately, the non-diagonal entries are a direct function of the grid and the magnetic field, which gives the user the possibility to control the general performance of the equation solver.

The overall performance of any solid-state device under non-zero magnetic field condition must be different from the zero magnetic field case, because the magnetic field deflects the path of the current and either it improves or degrades the performance of the device. By running simulations with arbitrary magnetic fields using the new feature developed in MINIMOS-NT, an analysis for the non-zero magnetic field case can be made. Different examples of solid-state devices that can be analyzed under such condition can be given. Optical sensors can improve their performance by deflecting the path of the generated carriers by incident radiation. Carrying the generated carriers to the depleted region enhances the hole-electron separation by the electric field, increasing the detectivity of the optical sensor. In the case of MOSFETs with nanometric dimensions, the inversion layer can be moved upwards or downwards depending on the direction of the magnetic field and the carrier density. New insight from the quantization of the inversion layer can be obtained if the simulations with magnetic field use the proper models.

Bibliography

[1] Lászlo Andór, Henry P. Baltes, Arokia Nathan, and Heinz Gunter Schmidt-Weinmar. Numerical modeling of magnetic-field sensitive semiconductor devices. *IEEE Transactions on Electron Devices*, 32(7):1224–1230, July 1985.

[2] Francis Balestra and Gérard Ghibaudo. *Device and Circuit Cryogenic Operation for Low Temperature Electronics*. Kluwer Academic Publishers, 2001.

[3] Henry P. Baltes, Lászlo Andór, Arokia Nathan, and H. G. Schmidt-Weinmar. Two-dimensional numerical analysis of a silicon magnetic field sensor. *IEEE Transactions on Electron Devices*, 31(7):996–999, July 1984.

[4] Henry P. Baltes and Radivoje S. Popović. Integrated semiconductor magnetic field sensors. *Proceedings of the IEEE*, 74(8):1107–1132, August 1986.

[5] A. C. Beer. The Hall effect and related phenomena. *Solid-State Electronics*, 9(5):339–351, May 1966.

[6] D. R. Briglio, Arokia Nathan, and Henry P. Baltes. Measurement of Hall mobility in n-channel silicon inversion layer. *Canadian Journal of Physics*, 65(8):842–845, August 1987.

[7] Herbert B. Callen. The application of Onsager's reciprocal relations to thermoelectric, thermomagnetic, and galvanomagnetic effects. *Physical Review*, 73(11):1349–1358, June 1948.

[8] Herbert B. Callen. A note on the adiabatic thermomagnetic effects. *Physical Review*, 85(1):16–19, January 1952.

[9] Robert Caverly and Edward Peck. A finite-element model and characterization of the *p-i-n* magnetodiode at microwave frequencies. *Solid-State Electronics*, 30(5):473–477, May 1987.

[10] A. Chovet, Ch. S. Roumenin, G. Dimopoulos, and N. Mathieu. Comparison of noise properties of different magnetic-field semiconductor integrated sensors. *Sensors and Actuators A*, A22(1-3):790–794, March 1990.

[11] Claus Fischer. *Bauelementsimulation in einer computergestützten Entwurfsumgebung*. Dissertation, Technische Universität Wien, 1994.

[12] J. Flokstra, H. J. M. Ter Brake, E. P. Houwman, D. Veldhuis, W. Jaszczuk, M. Caspari, H. Rogalla, A. Martínez, and C. Rillo. A 19-channel d.c. SQUID magnetometer system for brain research. *Sensors and Actuators A*, 27(1-3):781 785, May 1991.

[13] H. Gajewski and K. Gärtner. On the discretization of van Roosbroeck's equations with magnetic field. *ZAMM*, 76(5):247 264, May 1996.

[14] R. C. Gallagher and W. S. Corak. A metal-oxide-semiconductor (MOS) Hall element. *Solid-State Electronics*, 9(5):571 580, May 1966.

[15] Joseph M. Giachino. Smart sensors. *Sensors and Actuators*, 10(3-4):239 248, Nov/Dec 1986.

[16] Edmundo A. Gutiérrez-D., R. S. Murphy-A., A. Torres-J., M. Linares-A., P. J. Garía-R., R. Rojas-H., and V.H. Páez-V. A sub-mT cryogenic silicon magnetic sensor. In A. Touboul, Y. Danto, J.-P. Klein, and H. Grünbacher, editors, *Proceedings of the 28th European Solid-State Device Research Conference*, pages 188 191, September 1998.

[17] Edmundo A. Gutiérrez-Domínguez, M. Jamal Deen, and Cor L. Claeys. *Low Temperature Electronics*. Academic Press, 2001.

[18] C. Jungemann, D. Dudenbostel, and B. Meinerzhagen. Hall factors of Si NMOS inversion layers for MAGFET modeling. *IEEE Transactions on Electron Devices*, 46(8):1803 1804, August 1999.

[19] Robert Klima. *Three-dimensional Device Simulation with MINIMOS-NT*. Dissertation, Technische Universität Wien, 2002.

[20] S. Kordić. Integrated silicon magnetic-field sensors. *Sensors and Actuators*, 10(3-4):347 378, Nov/Dec 1986.

[21] Jack Lau, Ping K. Ko, and Philip C.H. Chan. Modelling of split-drain magnetic field-effect transistor (MAGFET). *Sensors and Actuators A*, 49(3):155 162, July 1995.

[22] Otfried Madelung. *Introduction to Solid-State Theory*. Springer-Verlag Wien, New York, 1996.

[23] S. M. Abu Nailah and K. N. Khalis. Analysis of a novel 3-d magnetic field sensor. *Solid-State Electronics*, 33(9):1119 1124, September 1990.

[24] Arokia Nathan, Walter Allegretto, Henry P. Baltes, and Tom Smy. Carrier transport in GaAs Hall-cross devices. *Canadian Journal of Physics*, 65(8):956 960, August 1987.

[25] Arokia Nathan, Lászlo Andór, Henry P. Baltes, and H. G. Schmidt-Weinmar. Modeling of a dual-drain NMOS magnetic-field sensor. *IEEE Journal of Solid State Circuits*, 20(3):819 821, June 1985.

[26] Arokia Nathan, Andrew M. J. Huiser, and Henry P. Baltes. Two-dimensional numerical modeling of magnetic-field sensors in CMOS technology. *IEEE Transactions on Electron Devices*, 32(7):1212 1219, July 1985.

[27] J. Neudecker, H. Hornung, K. P. Frohmader, and D. Seitzer. Three-dimensional numerical modeling of Hall plates in inhomogeneous magnetic fields. *Solid-State Electronics*, 34(5):429 436, May 1991.

[28] Lars Onsager. Reciprocal relations in irreversible processes I. *Physical Review*, 37(4):405 426, February 1931.

[29] Lars Onsager. Reciprocal relations in irreversible processes II. *Physical Review*, 38(12):2265 2279, December 1931.

[30] H. Pfleiderer. Magnetodiode model. *Solid-State Electronics*, 15(3):335 353, March 1972.

[31] Radivoje S. Popović. Numerical analysis of MOS magnetic field sensors. *Solid-State Electronics*, 28(7):711 716, July 1985.

[32] Radivoje S. Popović and Heinrich P. Baltes. A CMOS magnetic-field sensor. *IEEE Journal of Solid State Circuits*, 18(4):426 428, August 1983.

[33] Pedro Javier García Ramírez. *Análisis, modelado y diseno de una estructura Split-Drain MAGFET bajo condiciones de operación a 77 K y 300 K.* PhD thesis, Intituto Nacional de Astrofísica, Óptica y Electrónica, 2000.

[34] Concetta Riccobene. *Multidimensional Analysis of Galvanomagnetic Effects in Magnetotransistors.* PhD thesis, Eidgenössiche Technische Hochschule Zürich, 1995.

[35] Concetta Riccobene, Gerhard K. Wachutka, Josef Bürgler, and Henry P. Baltes. Operating principle of dual collector magnetotransistors studied by two-dimensional simulation. *IEEE Transactions on Electron Devices*, 41(7):1136 1148, July 1994.

[36] Ljubisa Ristic. *Sensor Technology and Devices.* Artech House, Inc., 1994.

[37] S. Rudin, Gerhard K. Wachutka, and Henry P. Baltes. Thermal effects in magnetic microsensors modeling. *Sensors and Actuators A*, 27(1-3):731 735, May 1991.

[38] Karlheinz Seeger. *Semiconductor Physics: An Introduction.* Springer-Verlag., 1989.

[39] Siegfried Selberherr. *Analysis and Simulation of Semiconductor Devices.* Springer-Verlag Wien, New York, 1994.

[40] S. M. Sze. *Semiconductor Sensors.* John Wiley & Sons, Inc., 1994.

[41] Wei Tongli and He Ye. Computer analysis and design optimization of magnetic-field sensitive MOS device. *Solid-State Electronics*, 31(2):237–240, February 1988.

[42] Johannes W. A. von Kluge and Werner A. Langheinrich. An analytical model of MAGFET sensitivity including secondary effects using a continuous description of the geometric correction factor G. *IEEE Transactions on Electron Devices*, 46(1):89–95, January 1999.

[43] Gerhard K. Wachutka. Rigorous thermodynamic treatment of heat generation and conduction in semiconductor device modeling. *IEEE Transactions on Computer-Aided Design*, 9(11):1141–1149, November 1990.

[44] Gerhard K. Wachutka. Unified framework for thermal electrical, magnetic, and optical semiconductor device modeling. *COMPEL*, 10(4):311–321, October 1991.

Own Publications

[**1**] R. Rodríguez-Torres, E. A. Gutiérrez-Domínguez, R. Klima, and S. Selberherr, "Three-Dimensional Analysis of a MAGFET at 300 K and 77 K," in *Proceedings of the 32nd European Solid-State Device Research Conference* (G. Baccarani, E. Gnani, and M. Rudan, eds.), pp. 151 154, September 2002.

[**2**] R. Rodríguez-Torres, E. A. Gutiérrez-Domínguez, R. Klima, and S. Selberherr, "Three-Dimensional Simulations of Two-Drain MAGFETs," *This work has been submitted to the IEEE for possible publication* January 2003.

[**3**] R. Rodríguez-Torres, R. Klima, and S. Selberherr, "Three-Dimensional Analysis of Three-Drain MAGFETs," *This work has been submitted to the SISPAD 2003 Conference for possible presentation* February 2003.

Curriculum Vitae

[redacted]

December 1994
Graduation at Puebla Institute of Technlogy, Puebla, México.
Industrial electronic engineer.

August 14th, 1997
Received degree of "Maestro en Ciencias"
From the National Institute of Astrophysics, Optics, and Electronics, Puebla, México.

September 1997
Accepted in the doctoral program at the
National Institute of Astrophysics, Optics, and Electronics, Puebla, México.

September 1999
Accepted in the doctoral program at the
Institute for Microelectronics, Technical University Vienna.

May 31st, 2002
Received Ph. D. degree
From the National Institute of Astrophysics, Optics, and Electronics, Puebla, México.